Development of Micro Gas Chromatographs and Micro Photoionization Detectors

by

Hongbo Zhu

A dissertation submitted in partial fulfillment
of the requirements for the degree of
Doctor of Philosophy
(Biomedical Engineering)
in the University of Michigan
2019

Doctoral Committee:

Professor Xudong Fan, Chair
Professor Yogesh B. Gianchandani
Professor Katsuo Kurabayashi
Professor Euisik Yoon

Hongbo Zhu

hongbo@umich.edu

ORCID iD: 0000-0002-7612-4363

Dedication

To my wife Dr. Yaoxin Li and the enduring support of my parents

Acknowledgements

It is my great honor start the page of acknowledgments. There are so many people helped me getting accomplishments in the process of pressuring Ph.D. degree.

I would like to thank my advisor, Professor Xudong Fan who bring me the field of micro instrumental research. The advice, inspirations, and encouragements from him lead me forward to the point where I am today. His research enthusiasm and precise working style helped me reform to be an independent researcher throughout my Ph.D. study.

I also want to present my gratitude to Professor Katsuo Kurabayashi. The development of most key components during the coloration in these yeas were based on support from his lab. I'd like to thank Sanketh Buggaveeti who initialized the design and computational simulation of microcolumn heater, which helped me with related projects demonstrated in chapter 5 and 6. I also would like to thank Dr. Robert Nidetz who was my mentor in microfabrication. I learned a lot precious fabrication experience and failure analysis strategies from him. His support in microcolumn and micro detector fabrication strongly endorse our system or component design and optimization in chapter 1, chapter 5, and chapter 6.

I would thank my committee members, Professor Yogesh B. Gianchandani and Professor Euisik Yoon for the valuable feedback to my research work. Professor Edward T. Zellers provided a valuable experience of critical article reviews in my research field, which introduced a lot of talent works from worldwide groups and inspired my research scope. The students from his lab, Dr. William Reginald Collin, Junqi Wang, Changhua Zhan also shared their experience on micro gas chromatography system development in a detail, which helped me on system integration. I really

appreciated the help from Professor Zhaohui Zhong and his student Wenzhe Zang. Many of optimizations on system integration and device fabrication was implemented based on their advice.

I would like to thank the engineers (Nadine Wang, Katherine Beach, Greg Allion, Shawn Wright, Vishva Ray, Kevin Owen, etc.) at the Lurie Nanofabrication Facility for helping me through all fabrication process including training, protocol developments, and trouble shootings. In addition, I am also grateful to Professor Hui Li and Professor Weitai Wu for support during my master's and bachelor's study. They introduce me into Ph.D. study and encouraged me for the further research in graduate school.

I really appreciated to my awesome lab mates. Dr. Jiwon Lee and Menglian Zhou helped me and with first prototype instrument development, test platforms construction and experiment design. Dr. Jinyan She provides a great support on the projects of ultra-compact system development and formaldehyde detection. I'd like to thank Dr. Ruchi Sharma and Dr. Zhizheng Zang for the wonderful working experience on microfabrication in the cleanroom. I also appreciated Dr. Girish Kulkarni for his help, support, and guidance on my Michigan I-Corps project as well as circuit design. The helpful discussions and advice from Dr. Qiushu Chen, Dr. Yu-cheng Chen, Dr. Xiaoqin Wu, Xiaotian Tan, and Xuzhou li benefit and help me a lot in many areas due to the background and research area diversity. A special thanks to Maxwell Li on his help on writing and very useful discussion on projects. I've had a great time to interact with all group alumni and current lab members that I overlapped with. It's a great honor to be a member of professor Fan's group.

It is my pleasures to thank my wife, Dr. Yaoxin Li for her endless support for my research, study, and life. I'm so glad to have her with me in these years of abroad study with so many difficulties, and so many happy time experienced together, especially the year we have our son Daniel Zhuli. Her love and support made me keep going forward to overcome all challenges on

my road. My parents and parents in-low provided me with a great support and love, which made me brave to pursue my dream.

Finally, I would like to thank National Science Foundation (IIP-1342917), Environmental Protection Agency (83564401), Michigan Center for Wireless Integrated MicroSensing & Systems, and Intelligence Advanced Research Projects Activity (contract #: FA8650-17-C-9106) for providing financial support.

Table of Contents

List of Tables

List of Figures

List of Appendices

Abstract

Micro gas chromatographs are miniaturized analytical instruments developed based on gas chromatography (GC) and Micro-Electro-Mechanical Systems technologies for fast, on-site, volatile compound analysis. The small footprint of these devices enables portability, low power consumption, and fast analysis time. Due to these features, micro gas chromatographs can be applied to environmental monitoring, homeland security, and online quality tracking. This dissertation describes the development of prototype instruments as well as studies of core components such as micro preconcentrators, microcolumns, Deans switches, and micro vapor detectors. Two nondestructive photoionization detectors have been developed and verified to have ultra-low detection limits (few pg) as well as rapid response rates. The micro flow-through photoionization detector (micro-PID) integrates microfluidic channels and ionization chambers on monolithic chips, providing 'on column detection' for analytes. The micro-PID can be used at fluidic interfaces between each dimension in multidimensional GC systems for obtaining additional information for gas routing control and signal reconstruction. Helium dielectric barrier discharge photoionization detectors use helium plasma as an ionization source to emit photons with energies up to 17.5 eV. Thus, these detectors can serve as universal vapor sensors and will expand the application scope of micro GC systems. These detectors were used in an application on formaldehyde detection, which was studied with a heart cutting two-dimensional (2D) micro GC. Target compounds can be transferred into the second-dimensional system for further precise separation and detection. Analysis of other air pollution-related, toxic compounds was performed

by the first-dimensional column and micro-PID simultaneously. The formaldehyde low detection limit of the novel 2D system was tested to be sub-ppb (V/V) level with 6 min of sampling. The design, fabrication, and evaluation of separation microcolumns are also discussed in this dissertation. A stationary phase thickness gradient coated microcolumn was developed to generate high-resolution chromatograms by introducing a peak focusing effect. Additionally, a hybrid adhesive connection method was developed for high-temperature applications and evaluated to be leak free and volatile compound free up to 350 °C even after thermal cycling. By integrating all miniaturized components, including micro preconcentrators, microcolumns, and micro-PIDs, an ultra-compact micro GC system (147 g in weight and 0.14 L in volume) was constructed. By scaling down the system, we achieved high separation performance and low power consumption, which clearly separated 14 compounds in 3 minutes.

Chapter 1 Introduction

1.1 Introductory Remarks

This chapter presents introductory and background information about gas chromatography (GC) principles. The first section provides a brief review of GC instrumentation, followed by theoretical analysis of separation processes and performance evaluation methods in the second section. In the third section, background and motivation of GC miniaturization are discussed. A summary of miniaturized system design and other topics in subsequent chapters is presented in the final section.

1.2 Gas chromatography

GC is a physical separation technology for mixture analysis in gas phase samples and is commonly used in forensic science, pharmaceuticals, petrochemicals, and environmental sciences. Chemicals are distributed between two phases (i.e. stationary phase and mobile phase), which allows for separation of compounds without decomposition. GC can be classified into gas-solid chromatography and gas-liquid chromatography depending on the stationary phase material[1]. Gas-solid chromatography uses solid porous materials as the stationary phase and is typically used for permanent gas or low boiling point compound separation[2]. Gas-liquid chromatography has widespread applications for many types of semi-volatile and volatile compounds due to the variety of stationary phase materials (e.g. non-polar, mid-polar, high-polar or chiral). Generally, vaporizable, non-corrosive, and thermally stable chemical mixtures can be separated and detected by GC systems equipped with appropriate detectors. For special chemicals that do not fulfill these

requirements, a chemical derivatization is required in the sampling process. Figure 1.1 depicts the components of a basic GC system which includes carrier gas, injector, separation column, and detector.

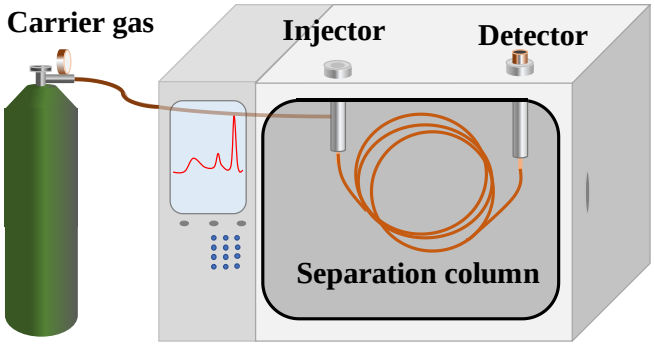

Figure 1.1 Schematic of basic GC system.

The carrier gas provides a driving pressure to the injector and carries vaporized mixtures into the separation column, where compound separation takes place. Due to differences in partitioning between the mobile phase (carrier gas) and stationary phase, compounds in mixture will elute out from the column at different rates. The detector measures the total quantity of eluted analyte by the corresponding change in signal strength. A chromatogram is then produced by a time-resolved detector signal from a control computer. Following this, spectrometry methods such as infrared spectrometry and mass spectrometry can be used to identify eluted compounds.

1.2.1 Injectors

Various types of injectors can be used for different applications. Commonly used methods are thermal desorption/cold trapping (TD/CT)[3], sample loops[4], and split/splitless (S/SL) injectors[5]. TD/CT is a method that integrates incoming samples using vapor adsorption materials in thermal desorption tubes (TDT). The analytes are concentrated to improve the system's signal to noise ratio and can be released by heating. The following mixture is trapped in a cold trapping tube (CTT), which can be rapidly heated to make a sharp injection into the GC. Sample loops are valve-

based injectors that are used to deliver the same volume of sample in each injection, which is useful for applications that require continuous monitoring. Compared with TD/CT, sample loops are simpler in structure and can be used to make lower dead volume interfaces. They are useful for permanent gas sampling, but typically do not provide any sample concentrations. S/SL injectors are the most popular injectors for GC due to their versatility and simplicity, but cannot handle samples directly. Samples are either injected from syringes or solid phase microextraction (SPME)[6] and can be vaporized rapidly by heating. The resulting vapor is partially delivered into separation columns by coupled carrier gas sources. There are three flow venting ports in S/SL injectors, which correspond to the column, septum purge, and split vent. In splitless mode, the vapor is entirely purged into the column, resulting in a broad peak due to injector dead volume. In split mode, the peak is much sharper since only a small fraction of the sample is injected into the column; thus, chromatogram resolution can be enhanced. However, since split mode only uses part of the sample, the signal is reduced at the detector. The split ratio is controlled by adjusting the flow resistance of the split vent and is typically set in the range of tens to a few hundred in split mode.

1.2.2 Separation column

Separation columns are categorized by fluidical channel structure, which are usually classified as wall coated open tubular (WCOT) capillaries[7] and packed columns. Packed columns are typically made from glass or stainless-steel tubes that are filled with silica partials onto which the stationary phase is coated[8]. The stationary phase in packed columns is thicker and less uniform compared to that in WCOT columns. The packed column is also impaired by band broadening due to Eddy diffusion and flow turbulence around packing partials, which results in lower efficiency[9]. WCOT columns are typically made from fused silica due to its flexibility and inertness, but require

deactivation of Silanol groups using silanization reactions[10]. These capillaries are coated with a sheath of polyimide, which protects silica from moisture, but limits the maximum operating temperature to 232 °C (400 °C short-term)[11]. Due to the homogeneity of polymer film coating, WCOT columns can have higher performance than packed columns, and since the pressure drop of open tubular columns is relatively small, WCOT columns can be 30 m or even 60 m long.

1.3 GC column parameters and performance metrics

An important measure of separation performance is chromatogram resolution, which can be calculated using Equation 1.3.1 [1]

$$R = 1/4\sqrt{N} \times (\alpha - 1) \times \frac{k'}{1 + k'} \qquad (1.3.1)$$

where R is resolution, N is effective theoretical plate number (which itself is a function of column length, inner diameter, carrier gas type, and linear velocity), k' is retention factor, and α is separation factor. The $(\alpha - 1)$ term represents peak separation and is a function of stationary phase composition and temperature. The $\frac{k'}{1+k'}$ term stands for retention and is affected by inner diameter, film thickness and composition, and temperature.

1.3.1 Column length

Column efficiency (N, theoretical plate number) is proportional to column length, but resolution is proportional to $\sqrt{N}$. Thus, long columns (e.g. 60 m) are typically only used for complex mixture analysis when peak separation is very small and high efficiency is required. Shorter columns (e.g. 30 m) have higher performance per unit length, shorter analysis time, and lower system pressure, making them more commonly used in typical benchtop GC systems.

Theoretical plate number can be calculated with equation[1]

$$N = 5.545\left(\frac{t_r}{t_w}\right)^2 \quad (1.3.1.1)$$

where t_r is the retention time counted from injection and t_w is the peak full width at half maximum. Analytes used for measurement of N are required to have a retention factor higher than 5 for precise performance evaluation.

1.3.2 Column inner diameter

Column inner diameter is inversely proportional to column efficiency and analyte retention. Reduction in tube diameter improves column efficiency and analyte retention by increasing analyte and stationary phase interactions. However, column head pressure is approximately an inverse square function of column radius, which means that smaller columns require higher instrument pressure. Sample capacity is also reduced as column diameter decreases (since the statuary phase volume decreases). Thus, there is a trade-off in optimizing column inner diameter: smaller inner diameter improves performance but requires higher pressure and results in reduced sample capacity.

1.3.3 Stationary film thickness

Column stationary phase film thickness (d_f) affects five critical GC parameters including retention, inertness, capacity, resolution, and bleed. Under isothermal conditions, retention factors of specific analytes are proportional to film thickness. Increasing the film thickness can increase retention for volatile analytes. Alternatively, higher column temperature can be used with the same retention factor. Increased film thickness also results in a higher stationary phase volume, which increases sample capacity. Furthermore, thicker film columns are more inert to analytes because the thick film shields analytes from active site residues on the silica capillary. Unfortunately, thicker films will bleed more stationary phase at high operating temperatures, which can

contaminate the detector and cause retainability degeneration. Thus, the upper-temperature limits of thick film columns will be lower than that for thin film columns[1].

1.3.4 Phase Ratio (β)

Phase ratio (β) is the ratio of column stationary phase to mobile phase and can be calculated with Equation 1.3.4.1

$$\beta = \frac{r}{2d_f} \tag{1.3.4.1}$$

where r is column radius and d_f is stationary phase film thickness. Phase ratio affects analyte retention in the stationary phase and is inversely proportional to retention factor, as shown in Equation 1.3.4.2

$$K_c = k\beta \tag{1.3.4.2}$$

where K_c is analyte distribution coefficient (ratio of concentration in stationary phase and mobile phase) and k is analyte retention factor (or capacity factor, partition ratio). k is a unitless measure of the column's retention of a compound and can be calculated from Equation 1.3.4.3

$$k = \frac{t_r - t_m}{t_m} \tag{1.3.4.3}$$

where t_r is the retention time measured from injection and t_m is the retention time for non-retained chemicals (e.g. time it takes carrier gas to travel through the system).

Equation 1.3.4.2 indicates that increasing the phase ratio will result in decreased analyte retention. By controlling the phase ratio, retention time can be kept constant when using columns of varying diameters. Compared to larger columns, smaller inner diameter columns can therefore use a thinner stationary phase for efficient separation with similar timescales.

1.3.5 Carrier gas flow rate and species

The van Deemter Equation relates various parameters to the height equivalent to a theoretical plate (HETP)[12] as shown in Equation (1.3.5.1)

$$HETP = A + \frac{B}{u} + Cu \tag{1.3.5.1}$$

where A is the Eddy diffusion parameter, B is the longitudinal diffusion coefficient, u is carrier gas linear velocity, and C is resistance to mass transfer coefficient.

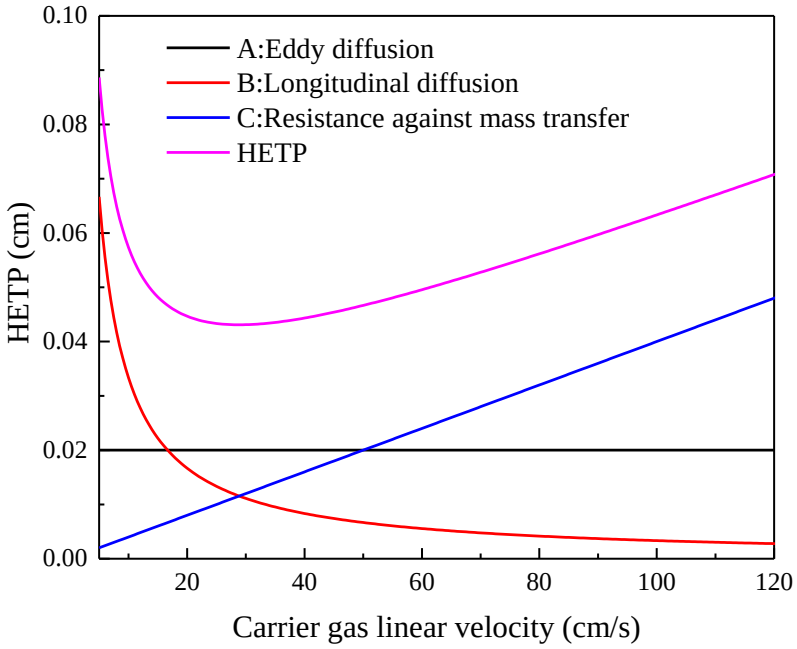

Figure 1.2 van Deemter plot (Golay plot) of HETP as function of carrier gas linear velocity.

Eddy diffusion is proportional to the asymmetry of the flow channel, which is caused by shape changes or flow turbulence. The longitudinal diffusion effect can be reduced by increasing carrier gas flow rate, since the diffusion time (same as analyte elution time) will be shortened. Resistance against mass transfer affects peak asymmetry (tailing effect) which results from higher analyte retention in stationary phase. An increase in resistance to mass transfer results in a lower amount of analyte in mobile phase, which then diffuses with a higher mobile phase velocity and

broadens the peak (as well as resulting in peak tailing). This effect can be reduced by reducing flow rate. As shown in Figure 1.2, plotting HETP as a function of carrier gas linear velocity (u) allows us to determine the optimal mobile phase velocity at which the highest column efficiency can be attained.

Helium, hydrogen, and nitrogen are the most commonly used carrier gases, and all have different effects on the shape of the HETP curve, as shown in Figure 1.3. Among these gases, the diffusivity of nitrogen is the lowest and results in a higher mass transfer effect, which means that the optimized flow rate using nitrogen will be lower than using the other two gases[13]. However, column efficiency is more sensitive to change in flow rate for nitrogen; thus, a small change in flow rate will result in a greater difference in results if nitrogen is used. Because of this, helium is often preferred over nitrogen as a carrier gas. From Figure 1.3, we see that the pressure must be controlled precisely for separation repeatability.

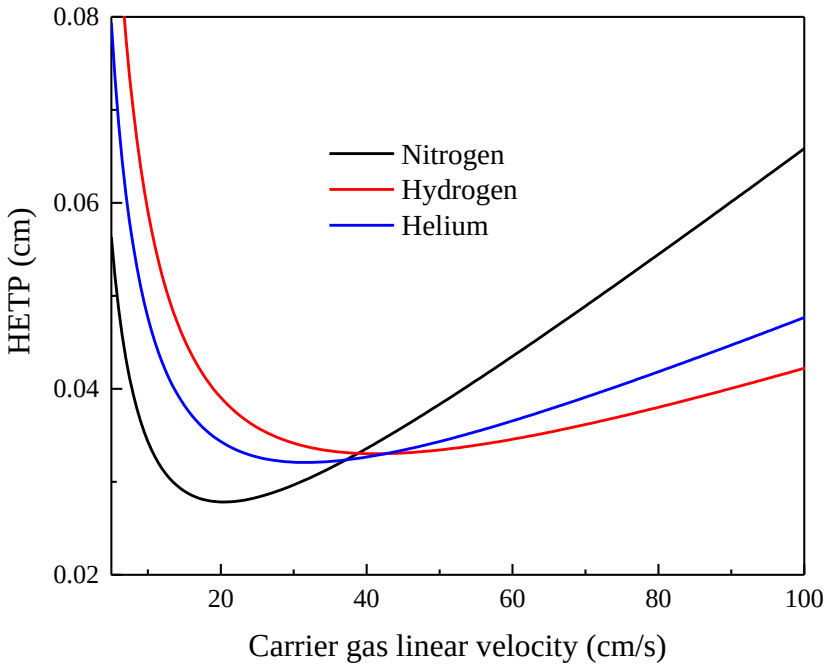

Figure 1.3 van Deemter plot with different carrier gases.

1.4 Miro GC (µGC) system

Conventional GC has high separation performance and low detection limit due to high efficiency, long capillary columns, and sensitive detectors. However, bulky size and heavy weight prevent ease of use for on-site and real-time analysis. Thus, small, light, miniaturized GCs[14] with low power consumption and fast analysis time were developed as highly portable or even wearable solutions for field applications. To develop these µGCs, Micro-Electro-Mechanical Systems (MEMS) technologies have been used to fabricate micro-columns[9, 15-17], micro-pumps[18-21], micro preconcentrators[22-24], and micro detectors along with on-column integrated temperature sensors and heaters. Miniaturization also reduces power consumption required for heating and results in lower dead volume in various components, such as in the column and at interfaces. By integrating all micro-components, a µGC system can perform sampling, injection, separation, and detection automatically, which also reduces the work required for sample transfer and pretreatment. A discussion of each micro-component follows.

1.4.1 Preconcentrator/thermal injector

Micro preconcentrators/thermal injectors (PC/TI) are typical components used for sampling and injection in µGCs and are similar to the aforementioned TD/CT used in benchtop GC systems. PC/TI integrates chemical trapping and injection together in the same device. In sampling mode, the PC/TI is connected to a pump, whereupon chemicals will be sucked into the PC/TI and trapped by adsorption materials such as activated charcoal and porous polymers. Sampling can be controlled by pump power and PC/TI flow resistance: flow rate must be optimized for sufficient interaction between adsorption materials and samples to prevent sample break through at high sampling flow rates.

In injection mode, PC/TI is connected to a carrier gas flow source and heated very rapidly. Trapped chemicals are released from the adsorption material quickly, resulting in a sharp injection to the separation column. PC/TI can be used to concentrate chemicals from large volumes of sample gas while injecting with small volumes in order to increase the low detection limit without any detector improvement. Improvements on PC/TI have been targeted at new adsorption materials, trapping chamber designs, and heaters. Activated charcoals are the most commonly used adsorption materials in PC/TI due to low volatile organic compound (VOC) background, high sample capacity, and wide volatile chemical applicability. A typical PC/TI design is shown in Figure 1.4.

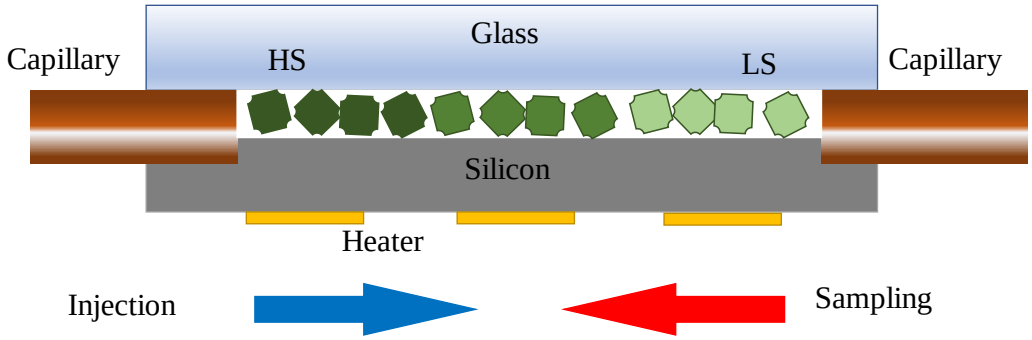

Figure 1.4 Schematic of PC/TI in cross section view.

In this design, a shallow chamber area (sorption-bed) was etched on a silicon wafer for adsorption material loading. The heater deposited on the bottom side of the silicon rapidly introduces thermal energy into the sorption bed via resistive heating. Due to the low thermal conductivity of charcoals, a signal layer of adsorption charcoals was filled in sorption-bed for better heater transfer as well as sharp injection. Chemical adsorbability is proportional to charcoal specific surface area; in sampling mode, charcoals having low specific surface area (LS) trap compounds with low volatility while compounds with high volatility move continuously and are trapped by charcoals having high specific surface area (HS). In injection mode, the PC/TI is heated

with reversed flow direction to allow LS charcoal to protect HS charcoal from chemical poisoning (permanent contamination) by exposure to low volatile compounds. Thus, PC/TI can be used for mixture sampling in a broad volatility range.

1.4.2 Micro columns

Traditional columns require long columns (up to 30 to 60 m) to ensure high enough total column efficiency. This requires large column thermostat ovens and high-pressure gas control systems, which are the main reasons for high power consumption and bulky size. With MEMS technology, miniaturized columns integrate heaters and micro fluidic channels on chip[9, 17, 25-27]. Micro columns are convenient for direct heating and temperature control, which can greatly reduce power consumption and volume. Micro column design involves channel layout[28], cross section[29] shape, in-column (fluid channel) structure[9, 27, 30], column material[9, 17, 31], coating material, and coating method[14, 32-33].

Current micro column layouts include micro circular spirals[34-35], squire spirals[16-17], and polygonal spirals (serpentine[36-37] and wave serpentine[15]). The goal is to fabricate the longest column possible in the limited chip area. Sharp turns also must be avoided in layout design in order to minimize path length difference between inner and outer paths in the turn. The cross-section shape is ideally circular and can be made from isotropic wet etching. However, due to chemical etching selectivity to the crystal orientation of silicon surfaces, the column channel aspect ratio is usually small. More commonly used are rectangular cross section micro GC columns due to ease of fabrication. High aspect ratio vertical column trenches are made with deep reactive ion etching (DRIE), which increases sample capacity and reduces flow resistance. Micro GC columns include open-tube capillary columns, semi-packed capillary columns, and multi-channel capillary columns. Open-tube capillary columns are the most popular type of micro column and will be

discussed later in this dissertation. Multi-channel capillary columns are difficult to be uniformly coated and not commonly used due to performance disparities between capillaries. Semi-packed columns enhance interactions between analyte and stationary phase, which improves column efficiency.

In generally, the stationary phase can be coated with either dynamic or static coating. In dynamic coating, the coating solution is slowly passed through the column by controlling the purging gas pressure. In order to coat the stationary phase film uniformly throughout the column, a dummy column with the same dimensions is connected at the end of the column. The coating solution is then purged out with a purging gas supplied continuously for several hours to ensure that the solvent is completely evaporated. The film thickness of the stationary phase by the coating speed and the concentration of the stationary phase in the solvent. However, the coating thickness cannot be accurately calculated.

In static coating, the film thickness can be precisely adjusted by changing the concentration of the coating solution. The thickness can be calculated with equation below

$$d_f = \frac{V_{column} \times C_{coating}}{\rho \times S} \tag{1.4.2.1}$$

where d_f is film thickness, V_{column} is the column total inner volume, S is column total inner surface area, ρ is stationary phase material density, and $C_{coating}$ is coating solution mass concentration.

In order to create the coating, the stationary phase material is dissolved in a low boiling-point solvent and pushed into the microcolumn with high pressure. The end of column is sealed and connected to a high-pressure source to remove air bubbles. The high-pressure end is then connected to a vacuum pump to dry out the solvent, leaving a layer of stationary phase on the inner wall. The solvent drying process is usually done in a water bath for isothermal control. A

crosslinking and deactivation are required after coating to increase the thermal stability and reduce tailing for polar compounds, respectively.

1.4.3 Micro pump

Miniaturized diaphragm pumps are the most common pumping devices in μGC systems due to low power consumption and small footprint. However, the presence of moving parts makes them challenging to use for remote testing in harsh environments. Instead, a solid-state pump (Knudsen pump) is a promising alternative solution for μGC[18-20, 38-40]. In Knudsen pumps, gas molecules will drift from the cold end to the hot end through a narrow channel. The thermal transpiration intensity is proportional to the intensity of the temperature gradient. Due to the motionless design, these pumps can provide reliable and precise control of gas flow with little wear and tear in harsh conditions. By using better thermal insulation packaging materials and narrower (on the order of sub-micron or nanometer) gas flow channels, high flow rate and high pressure can be achieved.

1.4.4 Micro detector

Micro detectors are connected downstream of separation columns and provide quantitative information of analytes. Like other components, micro detectors are required to have small footprints and low power consumption. Since the sample capacity of separation columns is reduced with channel dimension reduction, the sensitivity of micro detectors must be high enough for trace chemical detection. Many types of micro detectors have been developed with MEMS technology. Signal generation can be achieved by various means, including thermal ductility, ionization, and interface material property changes by vapor adsorption. Micro thermal conductive detectors (μTCD) are flow-through, nondestructive detectors which generate signals by detecting thermal conductivity differences between analyte flows and reference gases[41-42]. Due to the small

difference in thermal conductivity of the gases, the low detection limit of μTCD is typically on the order of a few nanograms. Micro flame ionization detectors (μFID) generate signals by collecting ion charges from analytes that are ionized by hydrogen flame[43]. The low detection limit is similar to μTCD because the ionization efficiency is impaired by flame size reduction. Commonly used interface materials include polymers, ionic liquids, nanoparticles, nanowires, and graphene. A thin layer of interface material coated on the transducer surface induces signals by corresponding physical property changes. For cantilever bridges[44], surface acoustic waves[45-46], and quartz crystal microbalance transducers[47-48], the signal is generated by resonance frequency changes caused by interface material mass changes after vapor adsorption. Charge density changes of graphene[49] and nanowires[50] can generate current changes in transistor type transducers. Polymer resistance, dielectric constant, and refractive index changes after vapor adsorption have been applied in chemresistors[51-53], chemcapacitors[54-56], and optical sensors[57-59], respectively. Multiple nondestructive detectors can be integrated to make sensor arrays providing chemical identification through multivariate analysis.

1.4.1 Multidimensional μGC

In complicated mixture chromatographic separation processes, it is difficult to separate all the compounds at once. Multi-stage chromatography is therefore proposed, which transfers the components eluted in the first-stage to second-stage for further separation. Two-stage combined chromatography, or two-dimensional (2-D) GC (or GC x GC) technology has been developed for more than twenty years[60-62]. Currently, the interface modulator is the key technology for 2-D GC development; one example would be Deans switch heart cutting technology[63-64]. One issue is that Deans switch heart cutting can only send a part of the compound to the second column, which leads to a signal reduction and less accuracy in quantitative detection. Thermal modulation is

another typical interface technology, which uses cold traps to accumulate analytes, which are released by rapid heating[65-66]. Therefore, the analyte from the first dimensional column can be sent into the second dimensional column by pulse injection without any loss. The post reconstruction of the detection result from the end of second column can provide a chromatogram with high peak capacity.

Current GC x GC (both commercial and those in research labs) are limited mainly to the bench-top format and even more power-intensive than 1-D benchtop GCs. Recently, μGC x μGC is being explored by research groups worldwide. However, current μGC x μGCs are also power intensive and have limited peak capacities primarily due to peak broadening introduced by the thermal modulation process and the limited length allowed for the 2D column[67]. A multidimensional, multichannel μGC was developed to enhance the separation performance[68-69]. In this design, multichannel second dimensional columns work in parallel, which allows for longer separation times and longer columns for the second dimension.

1.5 Outlook

Improvement of μGC relies on further development of each component. In addition to the requirements of small size, light weight, and low power consumption, some detailed desired features of specific components are described below.

PC/TI has very low thermal mass, meaning that the energy cost to heat this device to 310 °C (typical analyte injection temperature) is very low. To generate a sharp injection, PC/TI needs to be heated rapidly with high instantaneous power consumption, which is a challenge to the control circuit and heating resistor. Heater failure is likely to occur when current density is too high (beyond the electromigration threshold). Resistance, thermal mass, heating voltage, and the control relay need to be comprehensively optimized. The microcolumns used in μGC usually have high

column efficiency but require high pressure. Optimization on column length needs to be considered for system design. The heater layout on the column chip should prevent a temperature gradient when the column is programmably heated. Micro detectors are required to have rapid responses to prevent peak broadening after separation and may require heating to prevent low volatility compound condensation.

The fluidic connection interfaces between components are required to be leak-free, VOC free, low in dead volume, and cold spot free. Additionally, thermal cross talk should be limited as well. For example, when the PC/TI is heated, the column needs to stay at low temperature for high volatility compound separation. Each component should be developed without hindering other components and the overall system performance. In the following chapters, development of micro detectors, micro columns, and other improvements of μGCs will be presented.

1.6 References

1. Grob, R. L.; Barry, E. F., *Modern practice of gas chromatography*. John Wiley & Sons: 2004.
2. De Zeeuw, J.; De Nijs, R.; Henrich, L., Adsorption chromatography on PLOT (porous-layer open-tubular) columns: A new look at the future of capillary GC. *Journal of chromatographic science* **1987,** *25* (2), 71-83.
3. Badings, H. T.; de Jong, C.; Dooper, R. P. M., Automatic system for rapid analysis of volatile compounds by purge-and-cold-trapping/capillary gas chromatography. *Journal of High Resolution Chromatography* **1985,** *8* (11), 755-763.
4. Vreuls, J.; De Jong, G.; Brinkman, U. T., On-line coupling of liquid chromatography, capillary gas chromatography and mass spectrometry for the determination and identification of polycyclic aromatic hydrocarbons in vegetable oils. *Chromatographia* **1991,** *31* (3-4), 113-118.
5. Grob, K., *Split and splitless injection for quantitative gas chromatography*. John Wiley & Sons: 2008.
6. Curran, A. M.; Rabin, S. I.; Prada, P. A.; Furton, K. G., Comparison of the volatile organic compounds present in human odor using SPME-GC/MS. *Journal of chemical ecology* **2005,** *31* (7), 1607-1619.
7. Poole, C. F.; Poole, S. K., Separation characteristics of wall-coated open-tubular columns for gas chromatography. *Journal of Chromatography A* **2008,** *1184* (1-2), 254-280.
8. Gere, D. R.; Board, R.; McManigill, D., Supercritical fluid chromatography with small particle diameter packed columns. *Analytical Chemistry* **1982,** *54* (4), 736-740.
9. Ali, S.; Ashraf-Khorassani, M.; Taylor, L. T.; Agah, M., MEMS-based semi-packed gas chromatography columns. *Sensors and Actuators B: Chemical* **2009,** *141* (1), 309-315.
10. Sandra, P.; Verzele, M., Surface treatment, deactivation and coating in (GC) 2 (glass capillary gas chromatography). *Chromatographia* **1977,** *10* (8), 419-425.
11. Clair, A. K. S.; Clair, T. L. S., Addition polyimide adhesives containing various end groups. *Polymer Engineering & Science* **1982,** *22* (1), 9-14.
12. Kieselbach, R., Gas Chromatography-Source of the Velocity-Independent A Term in the Van Deemter Equation. *Analytical Chemistry* **1961,** *33* (6), 806-806.
13. Klee, M. S.; Blumberg, L. M., Theoretical and practical aspects of fast gas chromatography and method translation. *Journal of chromatographic science* **2002,** *40* (5), 234-247.
14. Lambertus, G.; Elstro, A.; Sensenig, K.; Potkay, J.; Agah, M.; Scheuering, S.; Wise, K.; Dorman, F.; Sacks, R., Design, Fabrication, and Evaluation of Microfabricated Columns for Gas Chromatography. *Analytical Chemistry* **2004,** *76* (9), 2629-2637.
15. Bhushan, A.; Yemane, D.; Trudell, D.; Overton, E. B.; Goettert, J., Fabrication of micro-gas chromatograph columns for fast chromatography. *Microsystem Technologies* **2007,** *13* (3-4), 361-368.
16. Agah, M.; Potkay, J. A.; Lambertus, G.; Sacks, R.; Wise, K. D., High-performance temperature-programmed microfabricated gas chromatography columns. *Journal of Microelectromechanical Systems* **2005,** *14* (5), 1039-1050.
17. Agah, M.; Lambertus, G. R.; Sacks, R.; Wise, K., High-Speed MEMS-Based Gas Chromatography. *Journal of Microelectromechanical Systems* **2006,** *15* (5), 1371-1378.
18. Liu, J.; Gupta, N. K.; Wise, K. D.; Gianchandani, Y. B.; Fan, X., Demonstration of motionless Knudsen pump based micro-gas chromatography featuring micro-fabricated columns and on-column detectors. *Lab on a Chip* **2011,** *11* (20), 3487-3492.

19. Qin, Y.; Gianchandani, Y. B., iGC2: an architecture for micro gas chromatographs utilizing integrated bi-directional pumps and multi-stage preconcentrators. *Journal of Micromechanics and Microengineering* **2014,** *24* (6), 065011.
20. Qin, Y.; Gianchandani, Y. B., iGC1: An integrated fluidic system for gas chromatography including Knudsen pump, preconcentrator, column, and detector microfabricated by a three-mask process. *Journal of Microelectromechanical Systems* **2014,** *23* (4), 980-990.
21. McNamara, S.; Gianchandani, Y. B., On-chip vacuum generated by a micromachined Knudsen pump. *Journal of Microelectromechanical Systems* **2005,** *14* (4), 741-746.
22. Zampolli, S.; Elmi, I.; Mancarella, F.; Betti, P.; Dalcanale, E.; Cardinali, G.; Severi, M., Real-time monitoring of sub-ppb concentrations of aromatic volatiles with a MEMS-enabled miniaturized gas-chromatograph. *Sensors and Actuators B: Chemical* **2009,** *141* (1), 322-328.
23. Tipler, A.; Campbell, G.; Collins, M., Analyte pre-concentrator for gas chromatography. Google Patents: 2003.
24. Reddy, K.; Guo, Y.; Liu, J.; Lee, W.; Oo, M. K. K.; Fan, X., Rapid, sensitive, and multiplexed on-chip optical sensors for micro-gas chromatography. *Lab on a Chip* **2012,** *12* (5), 901-905.
25. Sun, J.; Cui, D.; Li, Y.; Zhang, L.; Chen, J.; Li, H.; Chen, X., A high resolution MEMS based gas chromatography column for the analysis of benzene and toluene gaseous mixtures. *Sensors and Actuators B: Chemical* **2009,** *141* (2), 431-435.
26. Navaei, M.; Mahdavifar, A.; Dimandja, J.-M. D.; McMurray, G.; Hesketh, P. J., All silicon micro-GC column temperature programming using axial heating. *Micromachines* **2015,** *6* (7), 865-878.
27. Li, Y.; Du, X.; Wang, Y.; Tai, H.; Qiu, D.; Lin, Q.; Jiang, Y., Improvement of column efficiency in MEMS-Based gas chromatography column. *RSC Advances* **2014,** *4* (8), 3742-3747.
28. Radadia, A.; Salehi-Khojin, A.; Masel, R.; Shannon, M., The effect of microcolumn geometry on the performance of micro-gas chromatography columns for chip scale gas analyzers. *Sensors and Actuators B: Chemical* **2010,** *150* (1), 456-464.
29. Radadia, A. D.; Morgan, R. D.; Masel, R. I.; Shannon, M. A., Partially Buried Microcolumns for Micro Gas Analyzers. *Analytical Chemistry* **2009,** *81* (9), 3471-3477.
30. Nakai, T.; Nishiyama, S.; Shuzo, M.; Delaunay, J.; Yamada, I., Micro-fabricated semi-packed column for gas chromatography by using functionalized parylene as a stationary phase. *Journal of Micromechanics and Microengineering* **2009,** *19* (6), 065032.
31. MacNaughton, S. I.; Sonkusale, S., Gas Analysis System on Chip With Integrated Diverse Nanomaterial Sensor Array. *IEEE Sensors Journal* **2015,** *15* (6), 3500-3506.
32. Reidy, S.; Lambertus, G.; Reece, J.; Sacks, R., High-performance, static-coated silicon microfabricated columns for gas chromatography. *Analytical Chemistry* **2006,** *78* (8), 2623-2630.
33. Terry, S. C.; Jerman, J. H.; Angell, J. B., A gas chromatographic air analyzer fabricated on a silicon wafer. *IEEE Transactions on Electron Devices* **1979,** *26* (12), 1880-1886.
34. Matzke, C. M.; Kottenstette, R. J.; Casalnuovo, S. A.; Frye-Mason, G. C.; Hudson, M. L.; Sasaki, D. Y.; Manginell, R. P.; Wong, C. C. In *Microfabricated silicon gas chromatographic microchannels: fabrication and performance*, Micromachining and Microfabrication, SPIE: 1998; p 7.
35. Reston, R. R.; Kolesar, E. S., Silicon-micromachined gas chromatography system used to separate and detect ammonia and nitrogen dioxide. I. Design, fabrication, and integration of

the gas chromatography system. *Journal of Microelectromechanical Systems* **1994,** *3* (4), 134-146.
36. Radadia, A. D.; Masel, R. I.; Shannon, M. A.; Jerrell, J. P.; Cadwallader, K. R., Micromachined GC Columns for Fast Separation of Organophosphonate and Organosulfur Compounds. *Analytical Chemistry* **2008,** *80* (11), 4087-4094.
37. Bhushan, A.; Yemane, D.; Overton, E. B.; Goettert, J.; Murphy, M. C., Fabrication and Preliminary Results for LiGA Fabricated Nickel Micro Gas Chromatograph Columns. *Journal of Microelectromechanical Systems* **2007,** *16* (2), 383-393.
38. Gupta, N. K.; Gianchandani, Y. B., Thermal transpiration in mixed cellulose ester membranes: Enabling miniature, motionless gas pumps. *Microporous and Mesoporous Materials* **2011,** *142* (2-3), 535-541.
39. An, S.; Qin, Y.; Gianchandani, Y. B., A monolithic high-flow Knudsen pump using vertical Al 2 O 3 channels in SOI. *Journal of Microelectromechanical Systems* **2015,** *24* (5), 1606-1615.
40. Qin, Y.; An, S.; Gianchandani, Y. B., Arrayed architectures for multi-stage Si-micromachined high-flow Knudsen pumps. *Journal of Micromechanics and Microengineering* **2015,** *25* (11), 115026.
41. Narayanan, S.; Alfeeli, B.; Agah, M., A micro gas chromatography chip with an embedded non-cascaded thermal conductivity detector. *Procedia Engineering* **2010,** *5*, 29-32.
42. Narayanan, S.; Agah, M., Fabrication and characterization of a suspended TCD integrated with a gas separation column. *Journal of Microelectromechanical Systems* **2013,** *22* (5), 1166-1173.
43. Deng, C.; Yang, X.; Li, N.; Huang, Y.; Zhang, X., A novel miniaturized flame ionization detector for portable gas chromatography. *Journal of chromatographic science* **2005,** *43* (7), 355-357.
44. Xu, P.; Li, X.; Yu, H.; Xu, T., Advanced nanoporous materials for micro-gravimetric sensing to trace-level bio/chemical molecules. *Sensors* **2014,** *14* (10), 19023-19056.
45. Yeo, L. Y.; Friend, J. R., Ultrafast microfluidics using surface acoustic waves. *Biomicrofluidics* **2009,** *3* (1), 012002.
46. Ballantine Jr, D. S.; Wohltjen, H., Surface acoustic wave devices for chemical analysis. *Analytical Chemistry* **1989,** *61* (11), 704A-715A.
47. Cheng, C.-S.; Chen, Y.-Q.; Lu, C.-J., Organic vapour sensing using localized surface plasmon resonance spectrum of metallic nanoparticles self assemble monolayer. *Talanta* **2007,** *73* (2), 358-365.
48. Chen, Y.-Q.; Lu, C.-J., Surface modification on silver nanoparticles for enhancing vapor selectivity of localized surface plasmon resonance sensors. *Sensors and Actuators B: Chemical* **2009,** *135* (2), 492-498.
49. Kulkarni, G. S.; Reddy, K.; Zhong, Z.; Fan, X., Graphene nanoelectronic heterodyne sensor for rapid and sensitive vapour detection. *Nature communications* **2014,** *5*, 4376.
50. Lee, C. Y.; Sharma, R.; Radadia, A. D.; Masel, R. I.; Strano, M. S., On-Chip Micro Gas Chromatograph Enabled by a Noncovalently Functionalized Single-Walled Carbon Nanotube Sensor Array. *Angewandte Chemie International Edition* **2008,** *47* (27), 5018-5021.
51. Steinecker, W. H.; Rowe, M.; Matzger, A.; Zellers, E. In *Chemiresistor array with nanocluster interfaces as a micro-GC detector*, TRANSDUCERS, Solid-State Sensors, Actuators and Microsystems, 12th International Conference on, 2003, IEEE: 2003; pp 1343-1346.

52. Zhong, Q.; Steinecker, W. H.; Zellers, E. T., Characterization of a high-performance portable GC with a chemiresistor array detector. *Analyst* **2009,** *134* (2), 283-293.
53. Kim, S. K.; Chang, H.; Zellers, E. T. In *Prototype micro gas chromatograph for breath biomarkers of respiratory disease*, TRANSDUCERS 2009 - 2009 International Solid-State Sensors, Actuators and Microsystems Conference, 21-25 June 2009; 2009; pp 128-131.
54. Qin, Y.; Gianchandani, Y. B., A fully electronic microfabricated gas chromatograph with complementary capacitive detectors for indoor pollutants. *Microsystems &Amp; Nanoengineering* **2016,** *2*, 15049.
55. Patel, S.; Mlsna, T.; Fruhberger, B.; Klaassen, E.; Cemalovic, S.; Baselt, D., Chemicapacitive microsensors for volatile organic compound detection. *Sensors and Actuators B: Chemical* **2003,** *96* (3), 541-553.
56. Mlsna, T. E.; Cemalovic, S.; Warburton, M.; Hobson, S. T.; Mlsna, D. A.; Patel, S. V., Chemicapacitive microsensors for chemical warfare agent and toxic industrial chemical detection. *Sensors and Actuators B: Chemical* **2006,** *116* (1-2), 192-201.
57. Sun, Y.; Fan, X., Optical ring resonators for biochemical and chemical sensing. *Analytical and bioanalytical chemistry* **2011,** *399* (1), 205-211.
58. Reddy, K.; Guo, Y.; Liu, J.; Lee, W.; Oo, M. K. K.; Fan, X., On-chip Fabry–Pérot interferometric sensors for micro-gas chromatography detection. *Sensors and Actuators B: Chemical* **2011,** *159* (1), 60-65.
59. Scholten, K.; Reddy, K.; Fan, X.; Zellers, E. T., Vapor discrimination by dual-laser reflectance sensing of a single functionalized nanoparticle film. *Analytical Methods* **2013,** *5* (16), 4268-4272.
60. Giddings, J., Concepts and comparisons in multidimensional separation. *Journal of High Resolution Chromatography* **1987,** *10* (5), 319-323.
61. Davis, J. M.; Giddings, J. C., Statistical method for estimation of number of components from single complex chromatograms: theory, computer-based testing, and analysis of errors. *Analytical chemistry* **1985,** *57* (12), 2168-2177.
62. Davis, J. M.; Giddings, J. C., Statistical method for estimation of number of components from single complex chromatograms: application to experimental chromatograms. *Analytical chemistry* **1985,** *57* (12), 2178-2182.
63. Seeley, J. V.; Micyus, N. J.; Bandurski, S. V.; Seeley, S. K.; McCurry, J. D., Microfluidic deans switch for comprehensive two-dimensional gas chromatography. *Analytical chemistry* **2007,** *79* (5), 1840-1847.
64. David, F.; Jacq, K.; Sandra, P.; Baker, A.; Klee, M. S., Analysis of potential genotoxic impurities in pharmaceuticals by two-dimensional gas chromatography with Deans switching and independent column temperature control using a low-thermal-mass oven module. *Analytical and bioanalytical chemistry* **2010,** *396* (3), 1291-1300.
65. Beens, J.; Boelens, H.; Tijssen, R.; Blomberg, J., Quantitative Aspects of Comprehensive Two-Dimensional Gas Chromatography (GC× GC). *Journal of High Resolution Chromatography* **1998,** *21* (1), 47-54.
66. Beens, J.; Adahchour, M.; Vreuls, R. J.; van Altena, K.; Udo, A. T., Simple, non-moving modulation interface for comprehensive two-dimensional gas chromatography. *Journal of Chromatography A* **2001,** *919* (1), 127-132.
67. Collin, W. R.; Bondy, A.; Paul, D.; Kurabayashi, K.; Zellers, E. T., μGC× μGC: comprehensive two-dimensional gas chromatographic separations with microfabricated components. *Analytical chemistry* **2015,** *87* (3), 1630-1637.

68. Liu, J.; Seo, J. H.; Li, Y.; Chen, D.; Kurabayashi, K.; Fan, X., Smart multi-channel two-dimensional micro-gas chromatography for rapid workplace hazardous volatile organic compounds measurement. *Lab on a Chip* **2013,** *13* (5), 818-825.
69. Lee, J.; Zhou, M.; Zhu, H.; Nidetz, R.; Kurabayashi, K.; Fan, X., Fully automated portable comprehensive 2-dimensional gas chromatography device. *Analytical chemistry* **2016,** *88* (20), 10266-10274.

Chapter 2 Flow-through Microfluidic Photoionization Detectors for Rapid and Highly Sensitive Vapor Detection

Reproduced from Ref. 38 with permission from the Royal Society of Chemistry

2.1 Introduction

GC is widely used for analysis of volatile organic compounds (VOCs). Miniaturized GCs, *i.e.*, μGCs are being developed for possible field applications. One critical component inside a μGC device is the vapor detector, which is required to be lightweight, small footprint, rapid, sensitive, and operable using low power/voltage. In addition, non-destructive and flow-through characteristics are highly desirable for consecutive vapor analysis in multi-dimensional μGCs without destroying analytes or GC elution profiles[1].

Flame ionization detectors (FIDs) are commonly used vapor detectors in bench-top GC instruments. They have high sensitivities (pico-gram), large dynamic ranges (6 orders of magnitude), and zero dead volumes. Miniaturized FIDs (μFIDs) are being developed for portable applications[2-6]. However, FIDs and μFIDs are destructive and cannot be placed in the middle of the vapor flow path to monitor multi-dimensional GC separation. They are used only at the terminal end of a GC instrument. Furthermore, use of hydrogen hinders their broad acceptance in μGC devices. Thermal conductivity detectors (TCDs) and μTCDs have been used as non-destructive, flow-through vapor detectors[7-8]. However, TCDs suffer from low sensitivity (nano-gram) and require helium, an expensive carrier gas. Electron capture detectors (ECDs) are another type of non-destructive vapor detector[7]. While have high sensitivity, they have a limited dynamic range and use radioactive materials for analyte ionization. Recently, many other types of

miniaturized non-destructive vapor detectors have been developed for μGC applications, including surface acoustic wave (SAW) detectors[9-11], chemi-capacitors[12-13], chemi-resistors[9, 14], optical vapor sensors[15-22], and nanoelectronic sensors[23-24]. These sensors have small footprints and are non-destructive, but may suffer from large dead volumes[9-14], low sensitivities[9, 12-14], requirement of electrical-optical-electrical conversions (for all optical vapors sensors), or limited vapor types[23-24]. In addition, these vapor sensors usually require surface polymer coatings to capture analytes, which may reduce detection speed due to absorption/desorption.

A photoionization detector (PID) is another type of vapor detector that has been developed for 50 years[25-34]. They are sensitive (picogram level), non-destructive, applicable to a wide range of vapors, and have a large dynamic range (six orders of magnitude). Nevertheless, due to signal tailing resulting from the large ionization chamber and dead volume, application of PIDs in GC systems has been limited. A typical commercial PID has an ionization chamber volume of 40-200 μL with the dead volume being 1/4-1/6 of the chamber volume[29]. The corresponding response time is on the order of a few seconds. However, these sharp peaks were generated at an extremely high flow rate (30 mL/min) or using make-up gas (20 mL/min) [32, 35-37], neither of which is desirable for a μGC system due to complicated fluidic design required and/or significant reduction in sensitivity. Recently, improvements in the chamber design were made to reduce the chamber volume down to 10 μL. A 30 ms response time (defined as the time from the base to 90% of peak height) or 45 ms full-width-at-half-maximum (FWHM) was achieved with a flow rate of 30 mL/min[32]. However, the response speed is still limited by the relatively large chamber (and dead volume), which becomes problematic at the low flow rates typically used in μGC. For example, the chamber volume alone can lead to a peak broadening of 600 ms for a 1 mL/min flow rate, not to mention the additional broadening from the associated dead volume, for which the effective flow rate would

be much lower. In order to achieve rapid responses, a small ionization chamber volume and a small dead volume are needed. Unfortunately, a small chamber always comes at the expense of the size of the electrode (corresponding to ion collection efficiency) and UV illumination cross section (corresponding to ionization efficiency), which reduces the sensitivity of the PID. Recently, a micro helium discharge PID was also developed by Agah's group, which utilizes high energy plasma (~20 eV) generated by helium discharge to ionize analytes[33-34]. The initial result indicated a detection limit of 350 pg[33]. Other recent work reported micro-discharge PID integration with a micro-fabricated GC that resulted in a detection limit as low as approximately 10 pg[34]. The drawbacks of this type of PID include the need for helium and high voltage (>500 V) for plasma generation.

In this chapter, we developed a rapid, flow-through, and highly sensitive microfluidic PID[38] that is micro-fabricated directly on a conductive silicon wafer with an Archimedean spiral channel commonly used in μGC columns[39-40]. This PID can be operated with low voltages (<10 VDC, over 10 times lower than those used in regular PIDs[27, 32, 41]). The microfluidic PID has a significantly reduced ionization chamber volume of only 1.3 μL, nearly 10 times smaller than the state-of-the-art and over 100 times smaller than commercial PIDs. Moreover, it has virtually zero dead volume (~2 nL) owing to its flow-through design. Consequently, the response time of the microfluidic PID is considerably shorter, ultimately limited by its residence time (7.8 ms for 10 mL/min and 78 ms for 1 mL/min). Experimentally, the PID response similar to the standard flame ionization detector (FID) response, with a peak FWHM of 0.25 s and 0.085 s for a flow rate of 2.3 mL/min and 10 mL/min, respectively. Our studies further showed that the microfluidic PID was able to detect analytes down to the picogram level (at 3 standard deviations) due to the large UV illumination area and electrode area. A linear dynamic range of six orders of magnitude was achieved owing to

more uniform and sufficient UV ionization. Finally, because of the very short distance between the electrodes, only 6 VDC was needed for microfluidic PID operation. A detailed comparison between the micro-PID[32], micro-discharge PID[34], and microfluidic PID (current work) is given in Table 2.1.

Table 2.1 Comparison between micro-PID, plasma-based PID, and microfluidic PID.

	μPID (reported in Ref. [32])	**Plasma-based PID (Reported in Ref. [34])**	**Microfluidic PID (this work)**
Design concept	Traditional design concept, but with a smaller chamber volume	New concept with micro-discharge PID integrated on a chip	New microfluidic flow-through concept. Low chamber volume and dead volume. Large electrode area. Low voltage
Ionization source	UV lamp on top of the ionization chamber (10.6 eV)	UV + Plasma (~20 eV)	UV lamp on top of the ionization chamber (10.6 eV)
Discharge electrode degradation	No	Yes	No
Source/analyte contact	Non-contact	Contact	Non-contact
External helium flow required	No	Yes	No
High voltage required	Yes (150 V)	Yes (>500 V)	No (6 V)
Detection limit	5 ppb for benzene, toluene, and styrene (no mass detection limit reported)	~10 pg for n-Octane	~5 pg for benzene, toluene, ethylbenzene, and m-xylene
Chamber size	10 μL	Not reported	1.3 μL
Response time (baseline to 90% of the peak)	30 ms for 30 mL/min flow rate	170 ms for 2.5 mL/min flow rate	160 ms and 55 ms for 2.3 and 10 mL/min flow rate, respectively
Dynamic range	6 orders of magnitude	Not reported	6 orders of magnitude
Linearity	Non-linear (square root)	Not reported	Linear
Integration with μGC systems	Acceptable	Best	Better

Temperature stability	Not reported	Not reported	Tested (20-60 ^{o}C)
Flow rate stability	Not reported	Not reported	Tested (2.3 – 10 mL/min)
Undesirable negative peaks in signal	Not present	Present (reasons unknown)	Not present

2.2 Theoretical analysis

2.2.1 Response time

The response time of a PID (t_{PID}) is expressed in Equation 2.2.1.1 and contributes to GC peak broadening. t_{PID} is mainly governed by ionization chamber volume and dead volume

$$(t_{PID})^2 \approx (t_{residence})^2 + (t_{dead})^2 = (\frac{V_{flow}}{F})^2 + (\frac{V_{dead}}{F'})^2, \quad (2.2.1.1)$$

where $t_{residence}$ is the analyte residence time for the majority of an analyte to flow through the PID chamber and t_{dead} represents the residual time required for the analyte in the dead volume to be swept out of the PID. V_{flow} and V_{dead} are the chamber flow volume (*i.e.*, the volume in the chamber swept by the mobile phase) and dead volume (*i.e.*, the volume in the chamber not swept by the mobile phase), respectively. $V_{flow} + V_{dead}$ = total chamber volume. F and F' are the volumetric flow rate for the analyte residing in the chamber flow volume and the dead volume, respectively. For a non-flow-through PID, the dead volume is usually 1/6-1/4 of the chamber volume[29] and is responsible for the tailing effect in GC peaks. While t_{dead} is difficult to estimate, $t_{residence}$ for various PID designs can easily be calculated, as presented in Table 2.2. The PID response time is ultimately limited by its chamber volume (assuming the dead volume is zero). Figures 2.1 and 2.2 plot COMSOL simulation results for various chamber sizes and corresponding fall times in PID

responses. Small chamber size and careful fluidic design can significantly improve the PID response time.

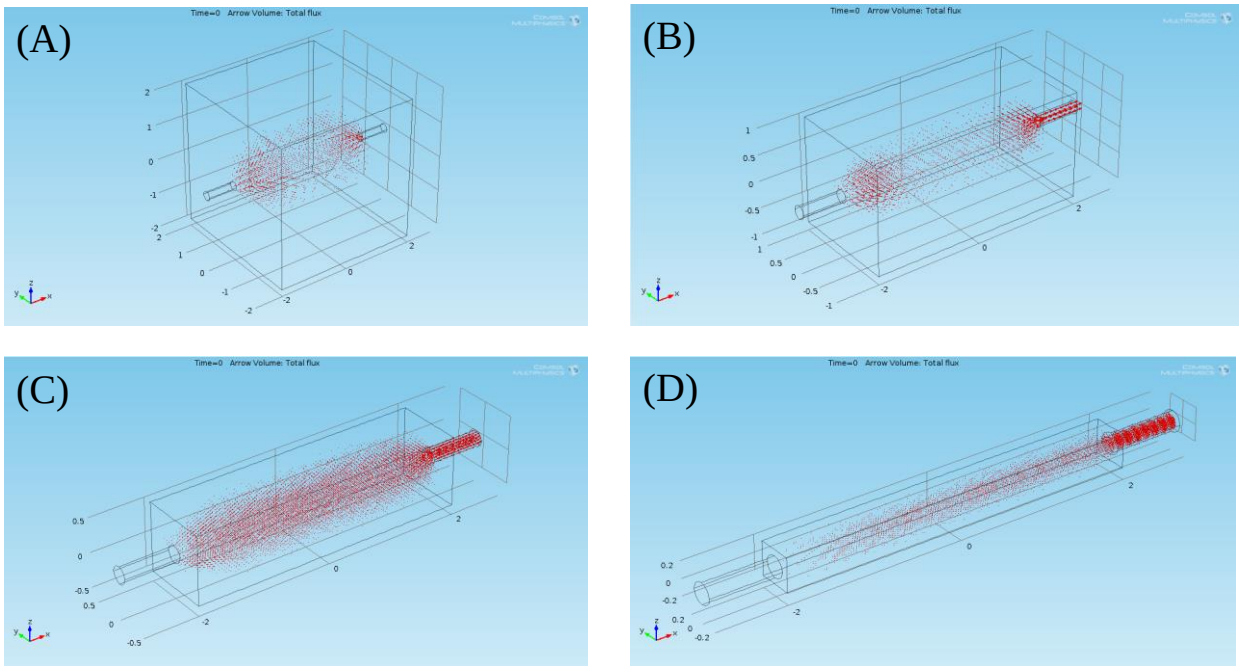

Figure 2.1 COMSOL simulation of analyte (toluene) concentrations for various chamber sizes. (A) 4x4x4 mm^3 = 64 μL. (B) 2x2x4 mm^3 = 16 μL. (C) 1x1x4 mm^3 = 4 μL. (D) 0.4x0.4x4 mm^3 = 0.64 μL. The inlet and outlet have a diameter of 0.25 mm. The chamber is initially filled homogeneously with toluene. Purging gas, helium, is flowed in at t=0 at a flow rate of 5 mL/min. The dead volume, defined as the region inside the chamber having a helium flow velocity less than 10% of the maximal velocity, is estimated to be 35.7 μL, 6.55 μL, 1.57 μL, and 0.24 μL, respectively, for (A)-(D).

Table 2.2 Analyte residence time for commercial, state-of-the-art, and microfluidic PIDs.

Chamber volume	Commercial PID (100 μL)	State-of-the-art PID (10 μL)	Microfluidic PID (1.3 μL)
$t_{residence}$ for 1 mL/min	6 s	0.6 s	0.078 s
$t_{residence}$ for 5 mL/min	1.2 s	0.12 s	0.016 s

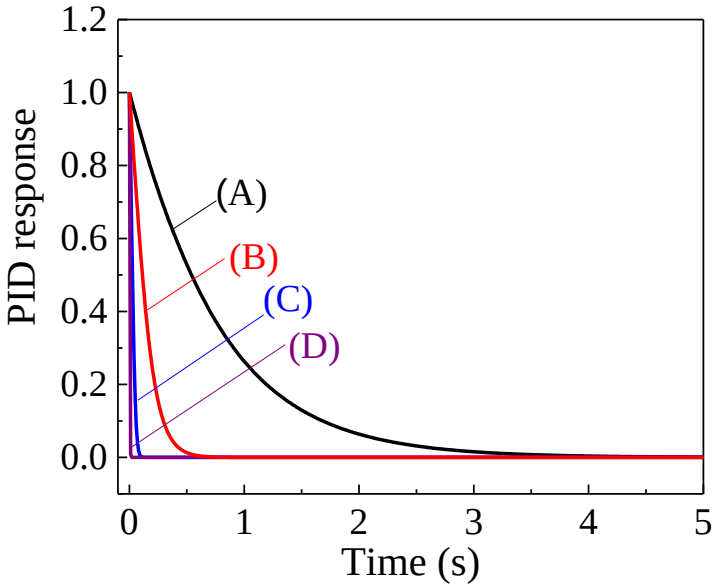

Figure 2.2 Normalized toluene concentration as a function of purging time for various chamber sizes. Curves (A)-(D) correspond to Figure 2.1 (A)-(D). The PID signal is linearly proportional to the analyte concentration inside the ionization chamber. Therefore, (A)-(D) represents the falling part of the PID peak. The fall time (*i.e.*, the time from the peak to 10% height) is 1.69 s, 0.3 s, 0.049s, and 0.0035 s, respectively, for (A)-(D).

2.2.2 Sensitivity

The current, i, generated by a PID can be expressed as[28-29]

$$i \propto C \cdot I_0 A \sigma_i [AB], \tag{2.2.2.1}$$

where I_0 is the vacuum ultraviolet (VUV) photon flux (# photons per m^2 per second), A is the effective VUV radiation area of an ionization chamber, σ_i is the ionization cross section, $[AB]$ is the analyte concentration, and C is the ion/electron collection efficiency at the electrodes. For a given analyte concentration and a given VUV light source, I_0, σ_I, and $[AB]$ are fixed; therefore, i is linearly proportional to the radiation area. Usually, the VUV light source has a relatively large output diameter (*e.g.*, 3.5 mm for the lamp used in this chapter). However, if we decrease the chamber volume for faster responses, the effective radiation area in the traditional PID design is

significantly reduced and the VUV lamp is significantly underutilized. In addition, in order to increase the ion collection efficiency, a relatively high voltage (a few hundred volts) is needed to reduce ion recombination and quenching that adversely impact the detection signal[27, 32, 41].

In contrast, the microfluidic PID uses a serpentine channel that reduces the chamber volume and eliminates dead volume while maintaining a large VUV illumination area. Furthermore, the ion collection efficiency is improved due to the significantly reduced distance between the two electrodes and the electrode area is also increased. The short distance increases the electric field strength for a given applied voltage and reduces ion recombination and quenching[28-29]. Consequently, the microfluidic PID can be operated with only 6 VDC. In addition, due to the short VUV illumination path, analytes at different depths can be ionized more uniformly to ensure detection linearity.

2.3 Experimental section

2.3.1 Materials

Highly doped p-type <100> single-sided polished conductive Si wafers with a resistivity of 0.001-0.005 Ω cm and a thickness of 380 μm, and 500 μm thick Pyrex glass wafers were purchased from University Wafer Company (Boston, MA, P/N 1318 and P/N 1112, respectively). A 10.6 eV VUV Kr lamp with a MgF_2 crystal window was purchased from Baseline-Mocon (P/N 043-257). GC guard columns (250 μm i.d. and 380 μm o.d.) and HP-5 coated columns (250 μm i.d., 380 μm o.d., 0.25 μm coating thickness) were purchased from Agilent. Optical adhesives (Norland® 81) were purchased from Norland (Cranbury, NJ). The commercial PID used for experimentation was acquired from Baseline-Mocon (P/N 043-234). The commercial flame ionization detector (FID) used was pre-installed on a Varian 3800 GC instrument. Benzene (P/N

270709), toluene (P/N 650579), ethylbenzene (P/N 03080), m-xylene (P/N 95670), and hexane (P/N 34859) were purchased from Sigma-Aldrich (St. Louis, MO, USA) and used without further purification. The relevant properties of these VOCs are listed in Table 2.3.

Table 2.3 Physical properties for experimental VOCs[42].

VOC	VP[a]	Density[b]	IP[c]
Benzene	75.1	876.50	9.25
Toluene	22.0	866.90	8.82
Ethylbenzene	7.15	866.50	8.76
m-Xylene	6.16	860.00	8.56
Hexane	121	654.80	10.18

[a]Vapor pressure (mm Hg) at 20 ^{o}C. [b]Mass density (kg m^{-3}). [c]Ionization potential (eV)

2.3.2 Fabrication and assembly

The microfluidic PID contained an Archimedean spiral microchannel and was fabricated on a conductive silicon wafer that was first anodically bonded to a Pyrex glass wafer (see Figure. 2.3(A)). Next, 2.0 μm of silicon dioxide was deposited on top of the silicon wafer using plasma-enhanced vapor deposition (PECVD) and patterned. After patterning, a 2.0 μm thick aluminum layer was deposited using lithography, evaporation, and liftoff. Deep reactive-ion etching (DRIE) was used to etch through the silicon wafer to form a final channel that had a cross section of 150 μm (width) × 380 μm (depth), a wall thickness of 50 μm, and a length of 2.3 cm. The entire channel area had an overall size of 15 mm × 15 mm ((see Figure. 2.3(B) for part of the chip). In order to reduce the dead volume at the interconnection between the GC column and the microfluidic channel, the terminals of the microfluidic channel were fabricated with a trapezoidal shape (400 μm (bottom width) × 150 μm (top width) × 100 μm (height)). The terminals of the microfluidic channel were connected to inlet/outlet ports (5.9 mm in length) so that guard columns

could be inserted (Figure. 2.3 (B) and (C)). The ionization chamber volume was 1.3 μL; the dead volume, which arises mainly from connections between the GC column and microfluidic PID inlet/outlet, was estimated to be ~2 nL.

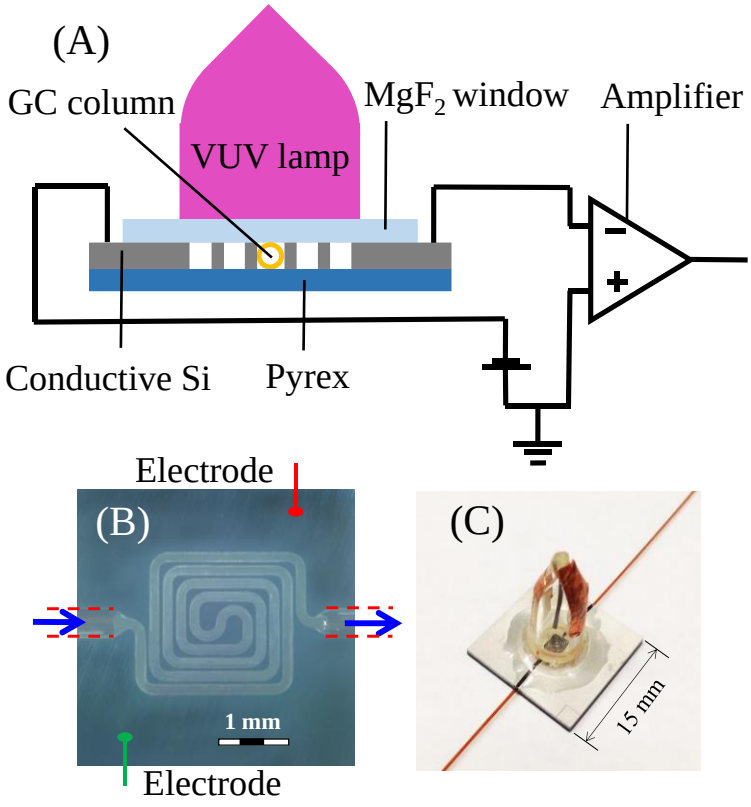

Figure 2.3 (A) Microfluidic PID structure. The microfluidic gas channel (width: 150 μm, depth: 380 μm, wall thickness: 50 μm, total length: 2.3 cm) was formed on a conductive silicon wafer, which also contained two electrodes. The top part of the microfluidic channel was sealed with a MgF_2 window on which a VUV lamp (3.5 mm effective diameter) was placed to cover the entire microfluidic channel area (2.4 mm x 2.4 mm). The PID working principle is illustrated in Figure 2.4. (B) Microscopic image of the microfluidic channel portion of the PID. The corresponding electrode layout is shown in Figure 2.5. (C) Picture of the microfluidic PID with inlet/outlet columns and a VUV lamp attached.

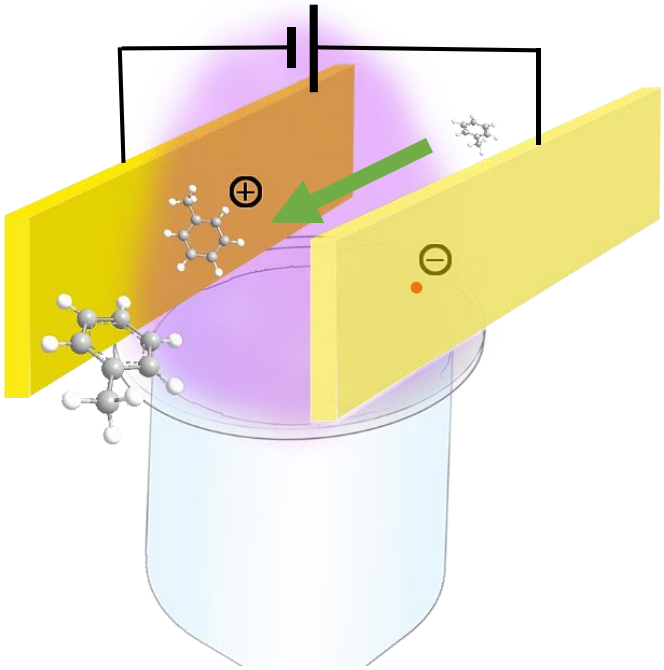

Figure 2.4 PID working principle.

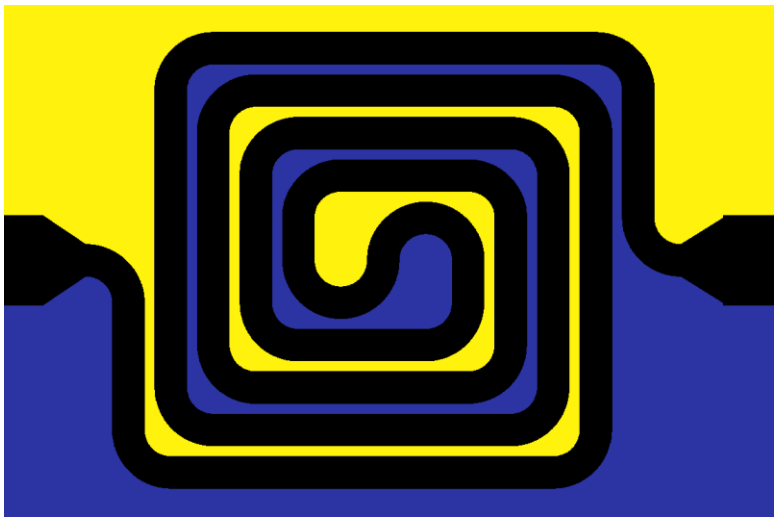

Figure 2.5 Electrode layout for the microfluidic PID. Blue and yellow: electrodes. Black: microfluidic channel.

After microfluidic channel fabrication, two electrodes were wire bonded to the aluminum layer on the microchannel and connected to the voltage supply and the amplifier, respectively (Figure 2.3 (A) and (B)). Then, the VUV Kr lamp was mounted on top of the microchannel and

sealed with optical adhesive. The lamp had an effective illumination diameter of 3.5 mm and covered the entire microfluidic PID area (2.4 mm x 2.4 mm). Finally, two 10 cm long guard columns were inserted into the inlet and outlet ports and sealed with optical adhesive.

2.3.3 Microfluidic PID operation

Details of microfluidic PID operation are illustrated in Figure 2.3 (A). In order to power the VUV lamp, we used a commercial power driving circuit (used to drive the commercial PID, usually connected to a 5 VDC external voltage supply). The two electrodes on the microfluidic channel were connected to -6 V DC and ground, respectively, which generated an electric field of approximately 400 V/cm across the channel. The electrodes were further connected to an amplifier (Stanford Research Systems SR560, input impedance = 100 MΩ + 25 pF) to form a closed circuit. Based on PID theory (see Equation 2.2.2.1) the PID signal is directly generated from charges on photoionized molecular fragments that produce current between the electrodes.[26, 28-29] According to Ohm's law, the final voltage signal is proportional to the current signal across the internal resistance of the amplifier. During operation, the amplifier bandwidth was maintained at 10 Hz. The output voltage was acquired through a DAQ card (NI USB-6009, National Instruments, Austin, TX) via LabView^{TM}. Note that although the p-type conductive silicon wafer has a high concentration of free holes, the photoelectric effect still occurred when the wafer was exposed to 10.6 eV VUV. As shown in Figure 2.6, when the VUV light was turned on, a baseline jump of approximately 94.3 mV with a noise of 0.68 mV (one standard deviation) was observed. Fig. 2.7 also characterizes the microfluidic PID temperature stability from 20 ^{o}C to 60 ^{o}C by placing the entire device inside a GC oven. When the temperature is below 40 ^{o}C, the baseline is nearly the same as for 20 ^{o}C. For temperatures close to the VUV lamp's specified maximal operating temperature (60 ^{o}C), a 44% increase in the baseline is observed. However, the microfluidic PID

noise remains constant (0.68 mV). In addition, the PID's sensitivity to analyte stays nearly unchanged (<10%), as shown in Figure 2.7 (B). For subsequent experiments reported here, the operating temperature is 20 ^{o}C unless otherwise specified. The corresponding baseline is subtracted for data analysis.

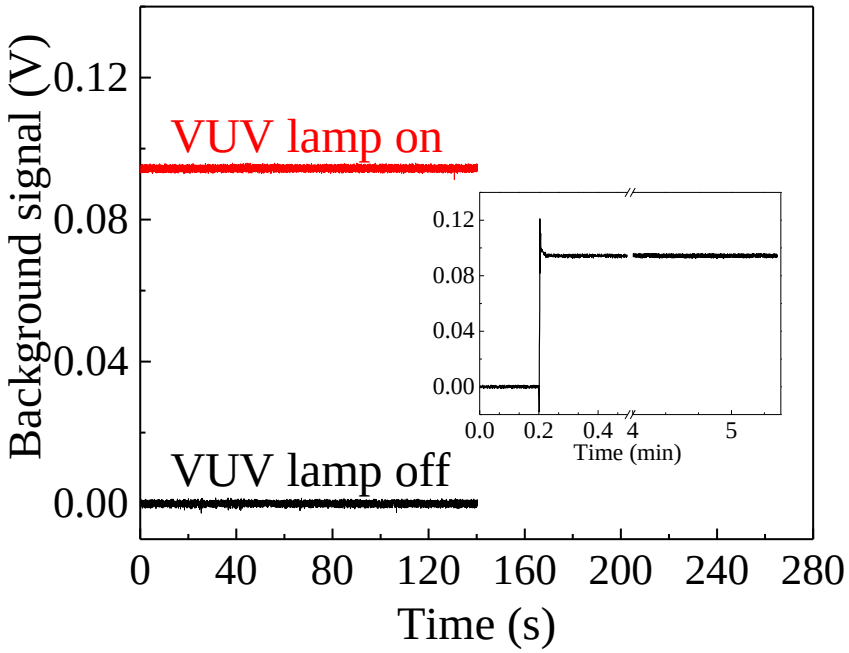

Figure 2.6 Voltage increases by 94.3 mV when the VUV lamp is turned on, which corresponds to a 94.3 pA current increase prior to amplification. The standard deviation of the noise is 0.68 mV. Amplification = 10x. Internal resistance of the amplifier = 100 MΩ + 25 pF. During measurement, helium was flowed through the microfluidic PID at a rate of 2 mL/min. Inset shows long-term stability up to 5.5 minutes.

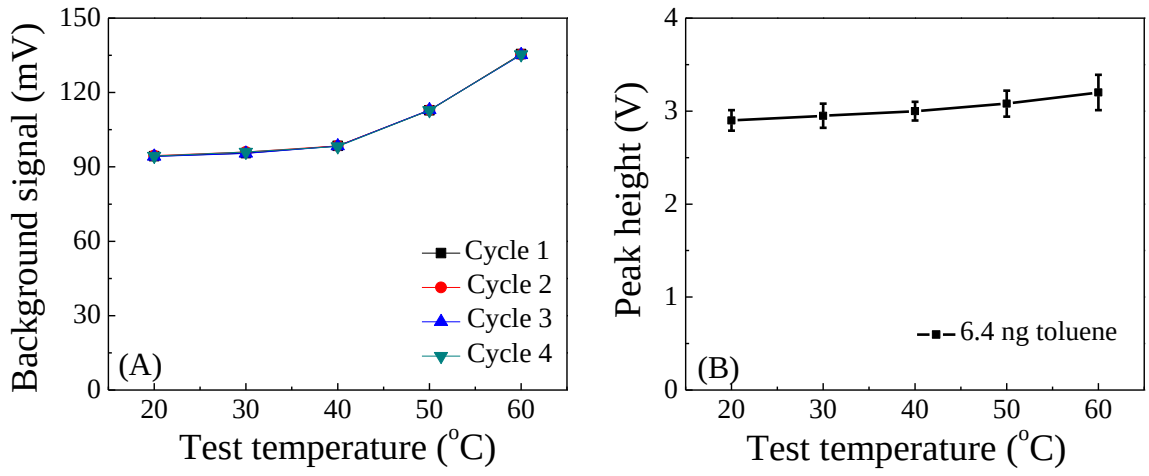

Figure 2.7 Microfluidic PID temperature stability tests. (A) Baseline as a function of device temperature. The noise level remains the same as for 20 ºC (Figure 2.6). (B) PID sensitivity to analyte as a function of temperature. The corresponding baselines are subtracted. Error bars are calculated based on 4 measurements. During testing, the entire device was placed inside a GC oven. 60 ºC is the maximal operating temperature.

2.3.4 Experimental setup

The experimental setup is shown in Figure 2.8. We tested five analytes to benchmark this system: benzene, toluene, ethylbenzene, m-xylene, and hexane. VOC samples were taken from the headspace of the corresponding screw-thread vials or diluted gaseous samples in Teflon septa sealed vials via a gas-tight syringe, then injected into a Varian 3800 GC instrument with a split ratio of 60. For detector characterization, the detector (microfluidic PID, commercial PID, or FID) was connected to the GC injection port via a 3 m long guard column. For VOC separation, a 6 m long HP-5 column was used to replace the guard column. Helium was used as the carrier gas.

For comparison purposes, we also performed VOC measurements by using a commercial PID and FID pre-installed on a Varian 3800 GC instrument to replace the microfluidic PID. To operate the commercial PID, we followed the instructions from the vendor. The GC column was

connected to the inlet port of the commercial PID, which was driven by 5 VDC. The signals from the FID and the commercial PID were recorded directly by the DAQ card without amplification.

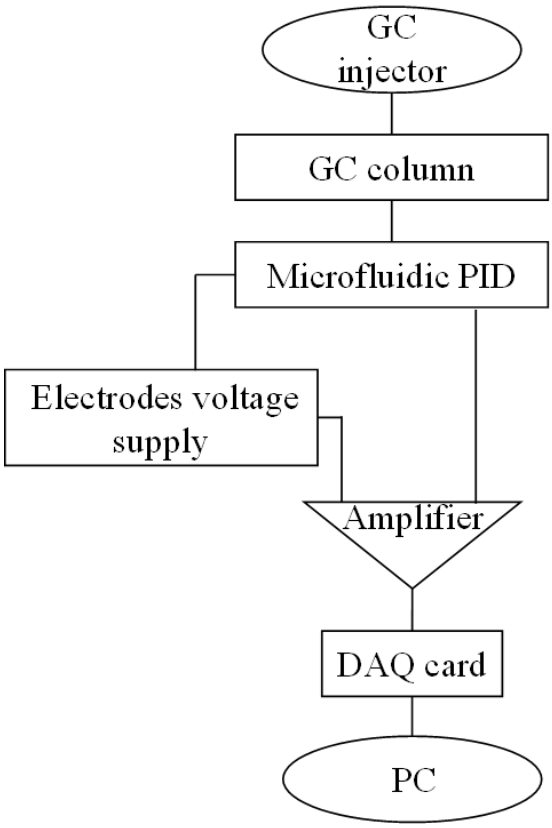

Figure 2.8 Experimental setup.

2.4 Results and discussion

2.4.1 Response time

Compared to previously reported PIDs and commercial PIDs, which usually have a fluidic chamber volume in the range of 10s to 100s of μL[27, 29, 32] and a dead volume of a few μL to 10s μL[29], the microfluidic PID has a significantly reduced chamber volume of only 1.3 μL with a nearly negligible dead volume (~2 nL). The smaller chamber volume and dead volume translate directly to a faster detector response time.

Figure 2.9 (A) compares the flow rate dependent FWHM for the microfluidic PID, commercial PID, and FID. As flow rate increases from 2.3 mL/min to 10 mL/min, the microfluidic PID peak width (FWHM) decreases from 0.25 s to 0.085 s. The peak width results mainly from the dead volume in the GC injector and longitudinal dispersion of the analyte (toluene) in the GC column. In fact, Figure 2.9 (B) and (C) show that the microfluidic PID generates a peak width and shape virtually identical to the FID, which has zero dead volume. The fastest response time (defined as the time from base to 90% of peak height, approximately 65% of FWHM) for the microfluidic PID is about 0.055 s at a 10 mL/min flow rate, close to the 0.03 s obtained with the state-of-the-art PID at 30 mL/min flow rate and with a very short (0.2 m) column (no longitudinal dispersion). In contrast, the commercial PID, which has a chamber volume of ~200 μL, has a peak width of 1-2.5 s, consistent with the peak width achieved by other commercial PIDs under high flow rates[32, 35-37]. Thus, the peak width of the microfluidic PID is easily reduced by 10-fold compared to the commercial PID. Ultimately, the peak width is limited by the residence time determined by the PID chamber volume and dead volume. For the current microfluidic PID, the detection speed can be as fast as 78 ms for a flow rate of 1 mL/min, which can further be improved by using a shorter channel length or smaller cross section.

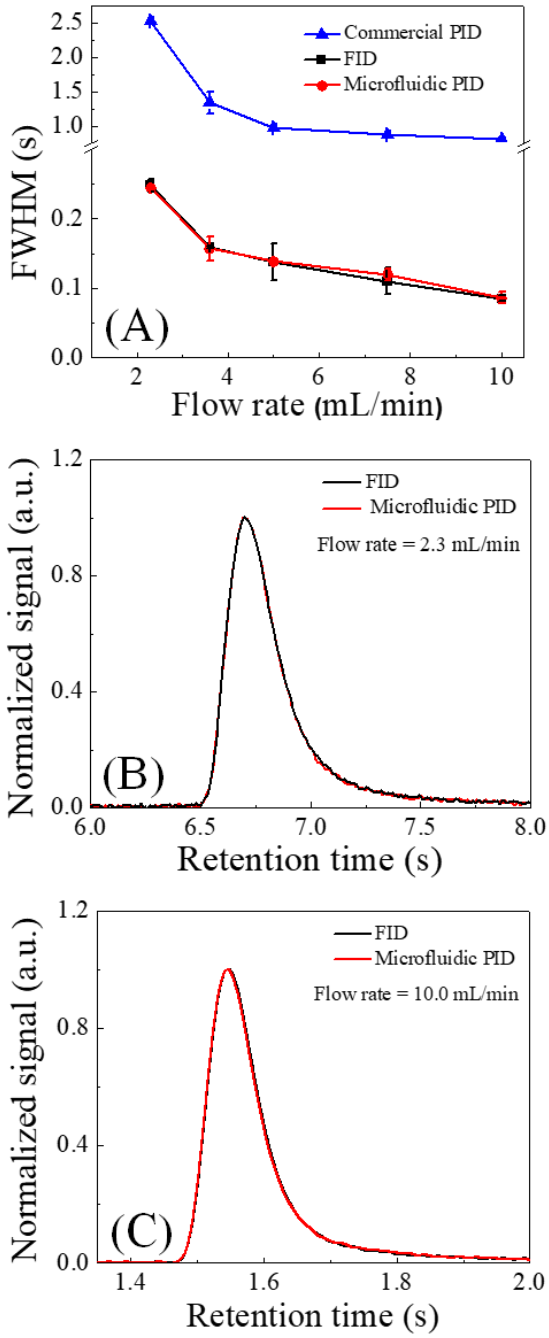

Figure 2.9 (A) Comparisons of FWHMs of toluenes peak obtained with commercial PID, FID, and microfluidic PID at various flow rates. Error bars are calculated based on four measurements. (B) and (C) Normalized toluene peaks obtained with FID and microfluidic PID at flow rates of 2.3 mL/min and 10 mL/min, showing FWHMs of 0.25 s and 0.085 s, respectively. The response time measured from the base to 90% of peak height is approximately 65% of FWHM. The corresponding toluene peaks obtained with a commercial PID are given in Figure 2.10.

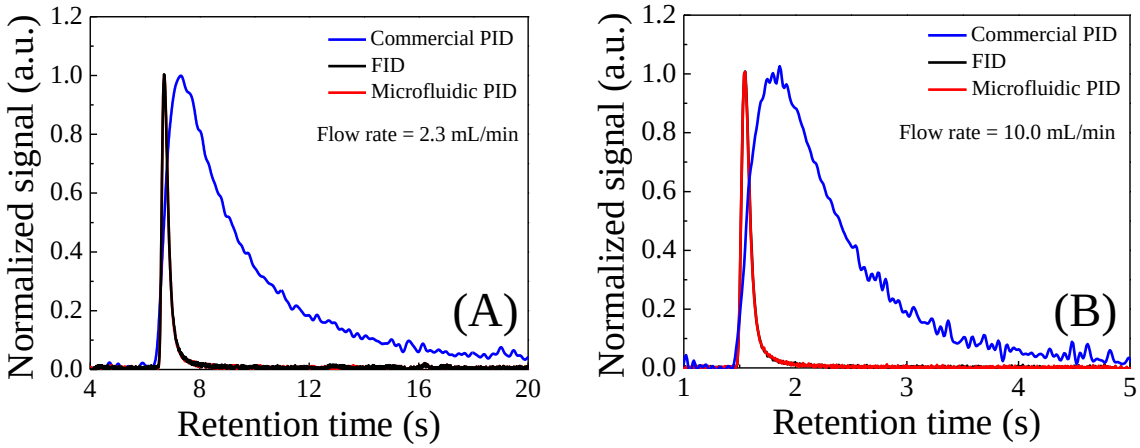

Figure 2.10 Normalized toluene peak obtained with commercial PID, FID, and microfluidic PID at flow rates of 2.3 mL/min and 10 mL/min, respectively. The corresponding magnified curves for FID and microfluidic PID are plotted in Figure 2.9.

2.4.2 Detection limit

Figure 2.11 plots the peak height as a function of injection mass for the five selected VOCs. While the peak height is similar for benzene, toluene, ethylbenzene, and m-xylene, it is much smaller for hexane, which is due to the high ionization potential (10.18 eV, close to the 10.6 eV light provided by the VUV lamp). At low injection masses, peak height increases linearly with injection mass (and with no change in peak width), which is reflected in the unity slope of those curves using a log-log scale. At high injection masses (~1 μg), the peak height starts to saturate and is accompanied by peak broadening.

To estimate the detection limit, we extrapolate using linearity of the peak height vs. mass, signal-to-noise ratio, and the noise (σ) of 0.68 mV for the microfluidic PID. The 3σ detection limit for a flow rate of 2.3 mL/min is presented in Table 2.4. For comparison, Table 2.4 also lists the detection limit for the commercial PID and FID. The microfluidic PID can detect VOCs down to the single pico-gram level (except for hexane, which has an ionization potential close to the VUV

photon energy). For the commercial PID, the detection limit is about 200 times higher than the microfluidic PID, which can partially be accounted for by the nearly 200 times larger chamber volume.

Table 2.4 Comparison of detection limit for FID, microfluidic PID, and commercial PID.

	Benzene	Toluene	Ethyl benzene	m-Xylene	Hexane
FID	0.62 pg (0.2 ppt)	0.90 pg (0.24 ppt)	1.46 pg (0.34 ppt)	1.47 pg (0.34 pg)	0.80 pg (0.23 ppt)
Microfluidic PID	4.25 pg (1.4 ppt)	4.48 pg (1.2 ppt)	5.68 pg (1.3 ppt)	5.00 pg (1.2 ppt)	30.6 pg (8.8 ppt)
Commercial PID	750 pg (240 ppt)	861 pg (230 ppt)	1354 pg (320 ppt)	1009 pg (230 ppt)	8081 pg (2300 ppt)

Part-per-trillion (ppt) is calculated for 1 L of gas at 1 atm. and 300 K.

The low detection limit of the microfluidic PID is achieved by a combination of large VUV illumination area, short illumination path, short electrode distance, and large electrode area. First, due to the serpentine structure of the microfluidic channel, the effective VUV illumination area is about 3.5 mm^2, about 60% of the entire area that the microfluidic channel occupies (2.4 mm x 2.4 mm, see Figure 2.3 (B)). In addition, due to the absorption of analytes, VUV light intensity decays very rapidly when it passes the ionization chamber. The short illumination path (380 μm) ensures that the analytes can be uniformly and efficiently ionized.

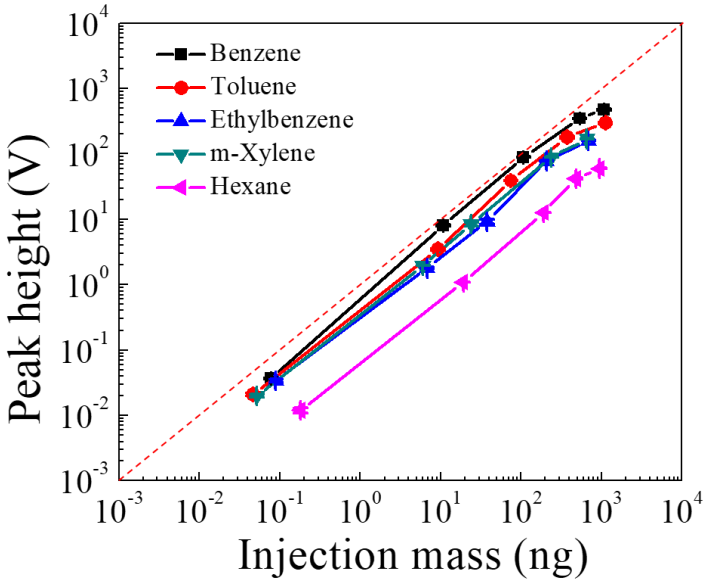

Figure 2.11 Peak height obtained by the microfluidic PID as a function of injection mass for five different VOCs plotted in log-log scale. The dashed line has a slope of unity for comparison. The detection limit (3σ) is 4.25 pg, 4.48 pg, 5.68 pg, 5.00 pg, and 30.6 pg for benzene, toluene, ethylbenzene, m-xylene, and hexane, respectively. The chromatographic peaks at the lowest injection mass are given in Figure 2.12.

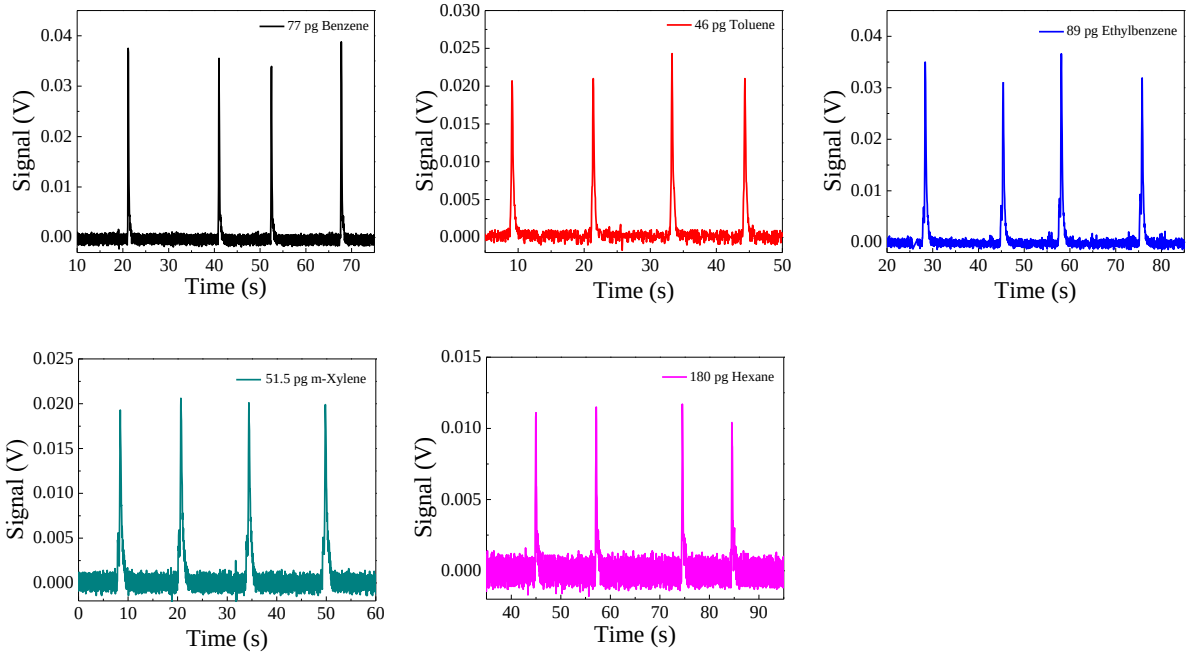

Figure 2.12 Microfluidic PID signals for repeatable measurements (4 times) of various analytes that were injected into the GC-PID system.

During the photoionization process, longer transit time for ions to reach the electrodes corresponds to increased recombination and quenching of anions and cations. Assuming a uniform electric field, the time for ions to move from one electrode to another, t, is given by Equation 2.4.2.1:

$$t = \sqrt{\frac{2m}{eV}} \cdot L, \tag{2.4.2.1}$$

where m and e are the mass and charge of an ion, respectively, L is the distance between the two electrodes, and V is the applied voltage.

Therefore, decreasing the electrode distance is a more effective way of decreasing the transit time (compared to increasing voltage). The short distance between the electrodes (150 μm) in the microfluidic PID results in a high electric field with only 6 VDC applied, and also results in suppression of recombination and quenching of ions. Together with the large electrode area (8.74 mm^2), this significantly enhances ion collection efficiency and uniformity. Improved PID performance is not only reflected in the detection limit, but also in the linearity of the device responsivity curve. A sub-linear responsivity curve indicates insufficient and non-uniform photoionization and ion collection.

2.4.3 Linearity

Besides high sensitivities and low detection limits, PIDs should exhibit a large linear detection range[7, 29]. Figure 2.13 presents the responsivity curves of the microfluidic PID for five different VOCs with injection masses ranging from below 50 pg to over 1000 ng. The peak areas in Figure 2.13 (A) show highly linear responses to the injection mass with an R^2 of 0.961-0.985 (see Table 2.5) in the linear regression analysis (forced zero Y-intercept at zero injection mass). Due to limitations in guard column capacity and sampling, the injection mass did not cover six

orders of magnitude experimentally. However, the detection limit of the microfluidic PID is only a few picograms and when using low injection masses, the peak area should decrease as the peak height decreases (Figure 2.11, but the peak width remains unchanged). Thus, we infer that the linear range for the microfluidic PID spans six orders of magnitude from a few pico-grams to a few micro-grams. In contrast, in Ref. 34, although the injection mass (or concentration) is increased by six orders of magnitude, the sensing signal increases only about 1000-fold, indicating imperfect fluidic design as well as insufficient and non-uniform photoionization and ion collection. Finally, the examined VOCs (except hexane, which has an ionization potential very close to the VUV photon energy and is difficult to ionize) have similar responsivity slopes when measured in units of Vs per mol (which is calculated by multiplying each slope in Vs/ng with the VOC's respective molecular weight, see Table 2.5). This suggests that the microfluidic PID detects the molar concentration of the analyte and does not perform mass-dependent detection, agreeing with the detection mechanism expected of a PID (see Equation 2.2.2.1).

Table 2.5 Linear curve fit parameters used in Figure 2.13(A).

	Benzene	**Toluene**	**Ethylbenzene**	**m-Xylene**	**Hexane**
Slope (Vs per ng)	0.10452	0.07719	0.04908	0.05752	0.01274
R^2	0.9856	0.96264	0.96136	0.9734	0.98119
Molecular weight (g/mol)	78	92	106	106	86
Slope (Vs per mol)	7.8×10^9	7.1×10^9	5.2×10^9	6.1×10^9	1.1×10^9

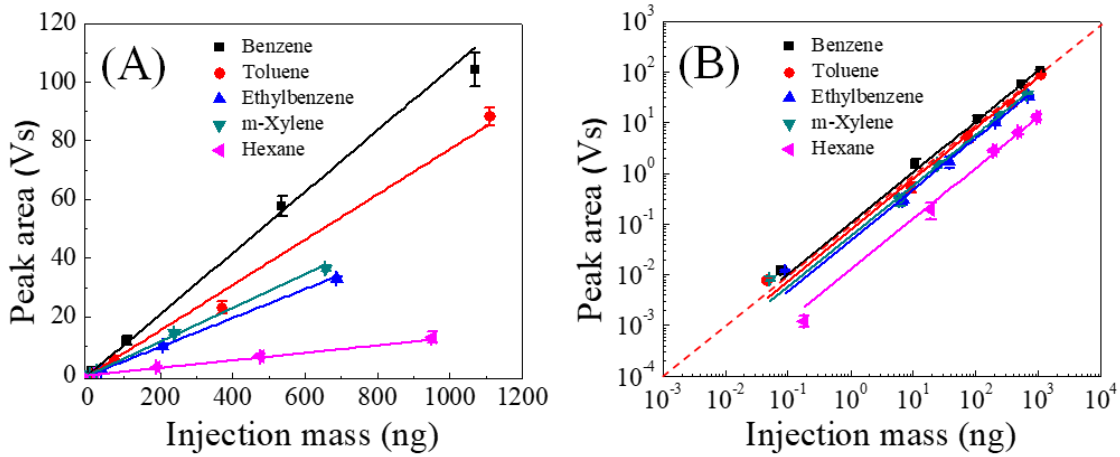

Figure 2.13 Microfluidic PID linearity for five different VOCs. (A) Peak area as a function of injection mass using a linear-linear scale. Solid lines are the linear fit (forced zero Y-intercept). The corresponding fit parameters are given in Table 2.5. Error bars are obtained with 4 measurements. (B) The corresponding data and curves in (A) plotted using a log-log scale. The dash line is linear with a slope of unity for comparison.

2.4.4 GC separation

To demonstrate the performance of the microfluidic PID for a GC system, we separated nine VOC analytes using a 6 m long HP-5 column. The analytes were sampled from the headspace of corresponding screw-thread vials, then injected into a Varian 3800 GC instrument with a split ratio of 60. High purity helium was used as the carrier gas at a flow rate of 2.0 mL/min. The column temperature was initially set to 40 ^{o}C for 0.2 minutes, then ramped to 75 ^{o}C at a rate of 30 ^{o}C/min. As shown in Figure 2.14, all peaks were symmetric with FWHMs around or below 1 s, which is a drastic improvement over previous GC separation results which used a commercial PID and make-up gas[37].

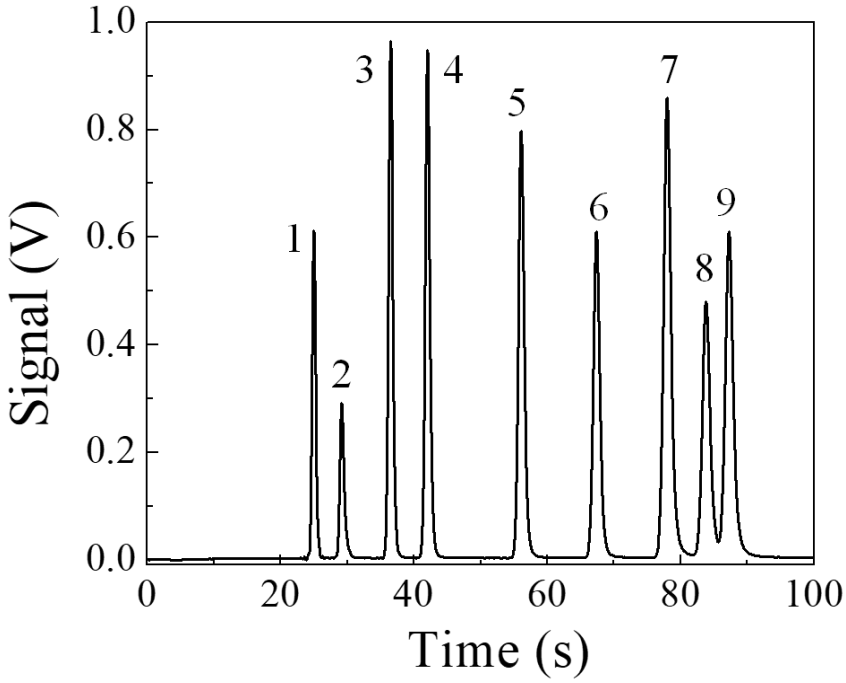

Figure 2.14 Microfluidic PID detection of 9 VOCs separated by GC using a 6 m long HP-5 column. The injected masses and FWHMs were: 1. vinylchloride (2.1 ng, 0.6 s); 2. cis-1,2-dichloroethene (1.0 ng, 0.7 s); 3. benzene (1.2 ng, 0.7 s); 4. trichloroethylene (2.1 ng, 0.8 s); 5. toluene (1.5 ng, 0.9 s); 6. tetrachloroethylene (1.1 ng, 1 s); 7. cholorobenzene (1.0 ng, 1.2 s); 8. ethylbenzene (1.5 ng, 1.2 s); 9. m-xylene (1.5 ng, 1.3 s). Temperature ramping: T=40 ºC for 0.2 min, then T=75 ºC ramped at a rate of 30 ºC/min. Helium was used as the carrier gas at a flow rate of 2.0 mL/min.

2.5 Conclusions

We have developed a microfluidic PID that can be used in a μGC system for rapid and highly sensitive VOC detection. Due to its flow-through design and non-destructive nature, the microfluidic PID can be placed nearly anywhere in the flow path. Furthermore, the simple and robust structure as well as low voltage operation enables field applications.

Additional work will involve the tasks at the component level, sub-system level, and GC system level. At the component level, improvements will be directed toward reducing the microfluidic PID base current and related noise to achieve even lower detection limits than those reported here. For example, a UV shielding layer can be deposited to cover the exposed silicon.

Different channel dimensions and serpentine structures will be explored to enhance VUV illumination and ion collection efficiency. A compact electronic circuit can replace the cumbersome amplifier and voltage supply. An electromagnetic shield can be constructed around the microfluidic PID to reduce electromagnetic interference. Furthermore, a micro-discharge based VUV light source that is micro-fabricated directly on chip can also be explored to replace the VUV lamp[33-34]. At the sub-system level, a μGC separation column will be co-constructed on the same chip with the microfluidic PID for multi-component integration. At the GC system level, the microfluidic PID will be installed in multi-dimensional μGC systems to monitor the analytes eluted from each dimension[1]. Finally, the microfluidic PID will be used in tandem with other electronic vapor sensors such as graphene nanoelectronic vapor detectors[24] to achieve better discrimination in vapor sensing.

2.6 References

1. Liu, J.; Seo, J. H.; Li, Y.; Chen, D.; Kurabayashi, K.; Fan, X., Smart multi-channel two-dimensional micro-gas chromatography for rapid workplace hazardous volatile organic compounds measurement. *Lab Chip* **2013,** *13* (5), 818-825.
2. Thurbide, K. B.; Hayward, T. C., Improved micro-flame detection method for gas chromatography. *Anal. Chim. Acta* **2004,** *519* (1), 121-128.
3. Deng, C. H.; Yang, X. H.; Li, N.; Huang, Y.; Zhang, X. M., A novel miniaturized flame ionization detector for portable gas chromatography. *J. Chromatogr. Sci.* **2005,** *43* (7), 355-357.
4. Wang, J. W.; Wang, H.; Duan, C. F.; Guan, Y. F., Micro-flame ionization detector with a novel structure for portable gas chromatograph. *Talanta* **2010,** *82* (3), 1022-1026.
5. Kuipers, W.; Müller, J., Sensitivity of a planar micro-flame ionization detector. *Talanta* **2010,** *82*, 1674-1679.
6. Kim, J.; Bae, B.; Hammonds, J.; Kang, T.; Shannon, M. A., Development of a micro-flame ionization detector using a diffusion flame. *Sens. Actuators B: Chemical* **2012,** *168*, 111-117.
7. Klee, M. S., Chapter 12: Detectors. In *Gas Chromatography*, Poole, C. F., Ed. Elsevier: New York, 2012.
8. Narayanan, S.; Agah, M., Fabrication and Characterization of a Suspended TCD Integrated With a Gas Separation Column. *IEEE JMEMS* **2013,** *22*, 1166-1173.
9. Cai, Q. Y.; Zellers, E. T., Dual-chemiresistor GC detector employing layer-protected metal nanocluster interfaces. *Anal. Chem.* **2002,** *74* (14), 3533-3539.
10. Lin, H. B.; Shih, J. S., Fullerene C60-cryptand coated surface acoustic wave quartz crystal sensor for organic vapors. *Sens. Actuators B: Chemical* **2003,** *92* (3), 243-254.
11. Lewis, P. R.; Manginell, R. P.; Adkins, D. R.; Kottenstette, R. J.; Wheeler, D. R.; Sokolowski, S. S.; Trudell, D. E.; Byrnes, J. E.; Okandan, M.; Bauer, J. M.; Manley, R. G.; Frye-Mason, G. C., Recent advancements in the gas-phase MicroChemLab. *IEEE Sens. J.* **2006,** *6* (3), 784-795.
12. McCorkle, D. L.; Warmack, R. J.; Patel, S. V.; Mlsna, T.; Hunter, S. R.; Ferrell, T. L., Ethanol vapor detection in aqueous environments using micro-capacitors and dielectric polymers. *Sens. Actuators B: Chemical* **2005,** *107* (2), 892-903.
13. Patel, S. V.; Hobson, S. T.; Cemalovic, S.; Mlsna, T. E., Detection of methyl salicylate using polymer-filled chemicapacitors. *Talanta* **2008,** *76* (4), 872-877.
14. Wright, L. K.; Zellers, E. T., A nanoparticle-coated chemiresistor array as a microscale gas chromatograph detector for explosive marker compounds: flow rate and temperature effects. *Analyst* **2013,** *138* (22), 6860-6868.
15. Shopova, S. I.; White, I. M.; Sun, Y.; Zhu, H.; Fan, X.; Frye-Mason, G.; Thompson, A.; Ja, S.-j., On-Column Micro Gas Chromatography Detection with Capillary-Based Optical Ring Resonators. *Anal. Chem.* **2008,** *80*, 2232-2238.
16. Liu, J.; Sun, Y.; Fan, X., Highly versatile fiber-based optical Fabry-Pérot gas sensor. *Opt. Express* **2009,** *17* (4), 2731-2738.
17. Liu, J.; Sun, Y.; Howard, D. J.; Frye-Mason, G.; Thompson, A. K.; Ja, S.-j.; Wang, S.-K.; Mengjun Bai; Taub, H.; Almasri, M.; Fan, X., Fabry-Perot Cavity Sensors for Multipoint On-Column Micro Gas Chromatography Detection. *Anal. Chem.* **2010,** *82*, 4370–4375.
18. Sun, Y.; Liu, J.; Howard, D. J.; Fan, X.; Frye-Mason, G.; Ja, S.-j.; Thompson, A. K., Rapid tandem-column micro-gas chromatography based on optofluidic ring resonators with multi-point on-column detection. *Analyst* **2010,** *135*, 165-171.

19. Reddy, K.; Guo, Y.; Liu, J.; Lee, W.; Khaing Oo, M. K.; Fan, X., Rapid, sensitive, and multiplexed on-chip optical sensors for micro-gas chromatography. *Lab Chip* **2012,** *12*, 901-905.
20. Reddy, K.; Liu, J.; Khaing Oo, M. K.; Fan, X., Integrated Separation Columns and Fabry-Perot Sensors for Microgas Chromatography Systems. *IEEE JMEMS* **2013,** *22*, 1174-1179.
21. Scholten, K.; Fan, X.; Zellers, E. T., Microfabricated optofluidic ring resonator structures. *Appl. Phys. Lett.* **2011,** *99* (14), 141108.
22. Scholten, K.; Fan, X.; Zellers, E. T., A microfabricated optofluidic ring resonator for sensitive, high-speed detection of volatile organic compounds. *Lab Chip* **2014,** *14* (19), 3873-3880.
23. Lee, C. Y.; Sharma, R.; Radadia, A. D.; Masel, R. I.; Strano, M. S., On-Chip Micro Gas Chromatograph Enabled by a Noncovalently Functionalized Single-Walled Carbon Nanotube Sensor Array. *Angew. Chem. Int. Ed.* **2008,** *47*, 5018-5021.
24. Kulkarni, G. S.; Reddy, K.; Zhong, Z.; Fan, X., Graphene nanoelectronic heterodyne sensor for rapid and sensitive vapour detection. *Nature Commun.* **2014,** *5*, 4376.
25. Lovelock, J. E., A sensitive detector for gas chromatography. *J. Chromatogr. A* **1958,** *1*, 35-46.
26. Price, J. G. W.; Fenimore, D. C.; Simmonds, P. G.; Zlatkis, A., Design and operation of a photoionization detector for gas chromatography. *Anal. Chem.* **1968,** *40* (3), 541-547.
27. Ostojić, N.; Šternberg, Z., A new photoionization detector for gas chromatography. *Chromatographia* **1974,** *7* (1), 3-5.
28. Freedman, A. N., The photoionization detector: Theory, performance and application as a low-level monitor of oil vapour. *J. Chromatogr. A* **1980,** *190* (2), 263-273.
29. Verner, P., Photoionization detection and its applications in gas chromatography. *J. Chromatogr.* **1984,** *300*, 249-264.
30. Driscoll, J. N.; Duffy, M., Photoionization detector a versatile tool for environmental analysis. *Chromagr.* **1987,** *2*, 21-27.
31. Edwards, S. J.; Lewis, A. C.; Andrews, S. J.; Richard T. Lidster; Hamilton, J. F.; Rhodes, C. N., A compact comprehensive two-dimensional gas chromatography (GCXGC) approach for the analysis of biogenic VOCs. *Anal. Methods* **2013,** *5*, 141-150.
32. Sun, J.; Guan, F.; Cui, D.; Chen, X.; Zhang, L.; Chen, J., An improved photoionization detector with a micro gas chromatography column for portable rapid gas chromatography system. *Sens. Actuators B.* **2013,** *188*, 513– 518.
33. Narayanan, S.; Rice, G.; Agah, M., A micro-discharge photoionization detector for micro-gas chromatography. *Microchim. Acta* **2014,** *181*, 493-499.
34. Akbar, M.; Shakeel, H.; Agah, M., GC-on-Chip: Integrated Column and Photo Ionization Detector. *Lab Chip* **2015, DOI: 10.1039/C4LC01461H**.
35. Cox, R. D.; Earp, R. F., Determination of Trace Level Organics in Ambient Air by High-Resolution Gas Chromatography with Simultaneous Photoionization and Flame Ionization Detection. *Anal. Chem.* **1982,** *54*, 2265-2270.
36. Simpson, A. T.; Hardwick, K. R.; Walsh, P. T.; Brown, R. C.; Hemingway, M. A., Evaluation of diffusive samplers and photoionisation detectors for measuring very short peak exposures in the workplace. *J. Environ. Monit.* **2003,** *5*, 732-738.
37. Jian, R.-S.; Huang, Y.-S.; Lai, S.-L.; Sung, L.-Y.; Lu, C.-J., Compact instrumentation of a μ-GC for real time analysis of sub-ppb VOC mixtures. *Microchem. J.* **2013,** *108*, 161–167.

38. Zhu, H.; Nidetz, R.; Zhou, M.; Lee, J.; Buggaveeti, S.; Kurabayashi, K.; Fan, X., Flow-through microfluidic photoionization detectors for rapid and highly sensitive vapor detection. *Lab on a Chip* **2015,** *15* (14), 3021-3029.
39. Lambertus, G.; Elstro, A.; Sensenig, K.; Potkay, J.; Agah, M.; Scheuering, S.; Wise, K.; Dorman, F.; Sacks, R., Design, Fabrication, and Evaluation of Microfabricated Columns for Gas Chromatography. *Anal. Chem.* **2004,** *76* (9), 2629-2637.
40. Reidy, S.; Lambertus, G.; Reece, J.; Sacks, R., High-Performance, Static-Coated Silicon Microfabricated Columns for Gas Chromatography. *Anal. Chem.* **2006,** *78* (8), 2623-2630.
41. Liess, M.; Leonhardt, M., New operation principle for ultra-stable photo-ionization detectors. *Meas. Sci. Technol.* **2003,** *14*, 427-432.
42. Baysinger, G. CRC Handbook of Chemistry and Physics. National Institute of Standards and Technology, 2014.

Chapter 3 Low Power Miniaturized Helium Dielectric Barrier Discharge Photoionization Detectors for Highly Sensitive Vapor Detection

3.1 Introduction

Photoionization detectors (PIDs) are being widely used in GC systems due to their high sensitivity and large dynamic range[1-3]. In a typical design, a PID consists of a VUV lamp filled with low-pressure rare gases such as xenon, krypton, and argon, which generate photons ranging from 9.6 eV to 11.8 eV, and a sealing window made of a UV transparent crystal (*e.g.*, LiF, MgF_2, and CaF_2). However, these PIDs suffer from a very limited lifetime of a few hundred to a couple thousand hours and encounter gradual performance degradation due to gas leakage and window degradation caused by crystal solarization, water etching, and contamination by chemical compounds[4]. Thus, constant maintenance and calibration are needed during their entire operation lifetime. Furthermore, although these PIDs are able to provide sufficient photon energy (*e.g.*, 11.8 eV from argon based PIDs with a LiF window) to ionize most chemical compounds, there still exist many important compounds with ionization potentials (IPs) above or close to 11.8 eV, such as Freon (IP: 11.77 eV - 12.91 eV), methane (IP: 12.98 eV), chlorine trifluoride (IP: 12.65 eV), dichlorofluoromethane (IP: 12.39 eV), phosgene (IP: 11.77 eV), and ethane (IP: 11.65 eV), all of which cannot be analyzed with these PIDs.

Atmospheric pressure rare gas discharge based PIDs usually have a windowless design, which maximizes UV transmission and can potentially extend the PID lifetime. Helium is typically used in this type of PID and is used for Hopfield emission, which results from the transition from

the diatomic helium state to the dissociative helium state. By this process, photons ranging from 13.5 eV to 17.5 eV can be generated during helium discharge, making the helium discharge PID (HDBD-PID) virtually a universal detector for gas analysis[5]. In an HDBD-PID, helium plasma is usually generated by direct current (DC) discharge[6-8], pulsed discharge[5, 9-18], or dielectric barrier discharge (DBD)[19-22]. DC discharge relies on high voltages (or electric field) to break down helium into positive ions and electrons, thus generating gas plasma[23]. Recently, a miniaturized HDBD-PID based on DC discharge was developed, and used 550 VDC across a 20 μm gap with a power consumption of only 1.4 mW[7-8, 24]. A detection limit on the order of 10 pg was achieved[8]. Pulsed discharge is also called pulsed DC discharge. The operating principle is similar to DC discharge, but uses 1 kHz – 1 MHz pulses to decrease average power consumption and achieve more stable ionization/excitation[23]. Recently, a micro-pulsed discharge PID was also developed with a size of 10 cm^3 and a detection limit of a few pg[13, 25]. One of the major drawbacks of regular DC discharge is the sputtering effect, *i.e.* high-speed ions continuously bombard the cathode material[23], which limits the lifetime of the detector and requires constant maintenance of electrodes and chambers (such as electrode replacement and discharge chamber cleaning). In pulsed discharge, since the duty cycle and average electrical power are lower, the overall sputtering effect is lower. However, due to high instantaneous power, sputtering cannot be completely prevented. Widely used PIDs from Valco Instruments are based on pulsed discharge technology[5, 10-12, 17-18].

DBD uses high-voltage (1-100 kV) high-frequency (up to a few MHz) potentials to generate atmospheric pressure plasma. In DBD, dielectric materials (*e.g.*, glass, polymer, and quartz, *etc*.) are placed on the electrode surface facing the discharge chamber, thus forming a protection layer[23]. Compared to the two aforementioned methods, DBD provides more homogenous discharge[23, 26] and very long electrode operation lifetime. Thus, DBD has become the

preferred method for atmospheric pressure plasma generation in numerous applications[27-32]. Recently, a few DBD based helium discharge PIDs have become commercially available (BID-2010 Plus from Shimadzu and DBDID from ABB Inc.) with the detection limit ranging from a few tens of picograms to sub-picogram[33]. However, the existing DBD based HDBD-PIDs (BID-2010 Plus and DBDID) are bulky (similar to the dimensions and weight of a commercial FID), power intensive (DBDID: 12 W), require large auxiliary helium flow rates (50-100 mL/min), and have long warm-up times. While these HDBD-PIDs can be used in benchtop GC systems, they are not suitable for portable or micro-GC systems for field applications.

Here, we developed a DBD based on chip micro-HDBD-PID (μHDBD-PID) with dimensions of ~15 mm × ~10 mm × ~0.7 mm and a weight of ~0.25 g. It offers low power consumption (<400 mW), low helium consumption (5.8 mL/min), rapid responses (similar to FID), quick warm-up times (~5 min), low detection limit (few pg), large linear dynamic range (>4 orders of magnitude), and maintenance-free operation. Furthermore, the μHDBD-PID can be driven with a miniaturized (~5 cm × ~2.5 cm × ~2.5 cm), light (22 g), and low cost (~$2) power supply with a 1.5 VDC input. Here we report the design, fabrication, and characterization of a new μHDBD-PID and demonstrate application to GC separation. A detailed comparison of the present μHDBD-PID with other HDBD-PIDs is summarized in Table 3.1.

Table 3.1 A detailed comparison of our μHDPID with other HDPIDs

	Mesoscale Pulsed discharge helium ionization detector	VICI PD-D2-IM	Shimadzu BID	Integrated μDPID	μHDPID
Minimum or typical auxiliary helium flow rate (mL/min)	35	10	50 - 100	1	5.8
Limit of detection	Few pg	Low to sub-pg	Low to sub-pg	10 pg	Few pg
Dimensions	Approximately the size of an AA battery (7.7 mL)	~308 mL	Equivalent to commercial FID	On-chip scale	On-chip scale
Power consumption	N/A	N/A	N/A	1.4 mW (without power source power consumption included)	385 mW (all-inclusive)
Type of chemicals	Universal	Universal	Universal	Selective	Universal
Electrodes destruction	Yes	Yes	No	Yes	No
Warm up time	N/A	Few minutes	Overnight	4 hours	<5 min
Comments	Sensitive and small footprint, but high helium consumption and electrode maintenance is required	Very sensitive, quick warm up, and affordable helium consumption, but electrode maintenance work is needed	Very sensitive and maintenance-free, but high helium consumption, lengthy warm up time, and bulky size	Sensitive, tiny footprint, and low helium consumption, but requires maintenance and unexpected negative signals can be detected.	

Device fabrication and assembly

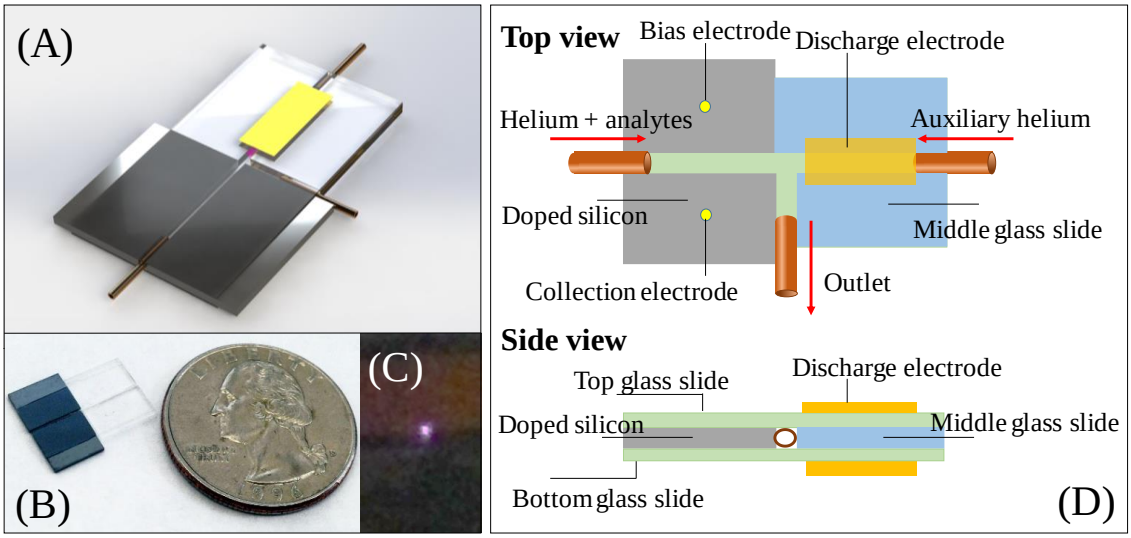

Figure 3.1 (A) 3-dimensional rendering of a micro-helium discharge photoionization detector (μHDBD-PID). (B) Picture of a μHDBD-PID (without discharge electrodes). (C) Plasma generated by a μHDBD-PID (most of the plasma was blocked by the electrode). (D) Detailed structure of a μHDBD-PID. See Figure 3.2 for all dimensions.

All silicon and glass wafers were purchased from University Wafer Company (Boston, MA). As shown in Figure 3.1 and Figure 3.2, a 100 μm thick Borofloat® 33 glass wafer (P/N 1737) was diced into 15 mm × 10 mm rectangular pieces and used as the top and bottom substrates. A 500 μm thick P-type <100> silicon wafer with double-side-polished 500 nm thick thermal oxide layers (P/N 2078) was diced into a 7.5 mm × 6 mm rectangular shape, followed by wet etching using 49% buffered HF to remove the oxide layer. As illustrated in Figure 3.1 (D), two pieces of such silicon wafers were then bonded onto the bottom glass substrate using UV-curable optical glue (Norland® 81). The gap between the two silicon wafers was 380 μm and created a fluidic channel for analytes and carrier gas (helium). The two silicon wafers also acted as the bias and the collection electrodes. A 500 μm thick Borofloat® 33 glass wafer (P/N 517) was diced into two rectangular pieces (7.5 mm × 4.8 mm and 7.1 mm × 4.8 mm) and then bonded

using the same UV-curable glue onto the bottom glass substrate with a 380 µm gap between each other to create a fluidic channel for auxiliary helium. Another gap of 380 µm was also created between the silicon wafer and the glass wafer to form the third fluidic channel as the outlet. Finally, the top glass substrate was bonded onto the middle silicon and glass pieces using the same UV-curable optical glue. After assembly, three guard columns with 380 µm OD and 250 µm ID were inserted into the two inlets and the outlet of the fluidic channels and sealed with optical glue.

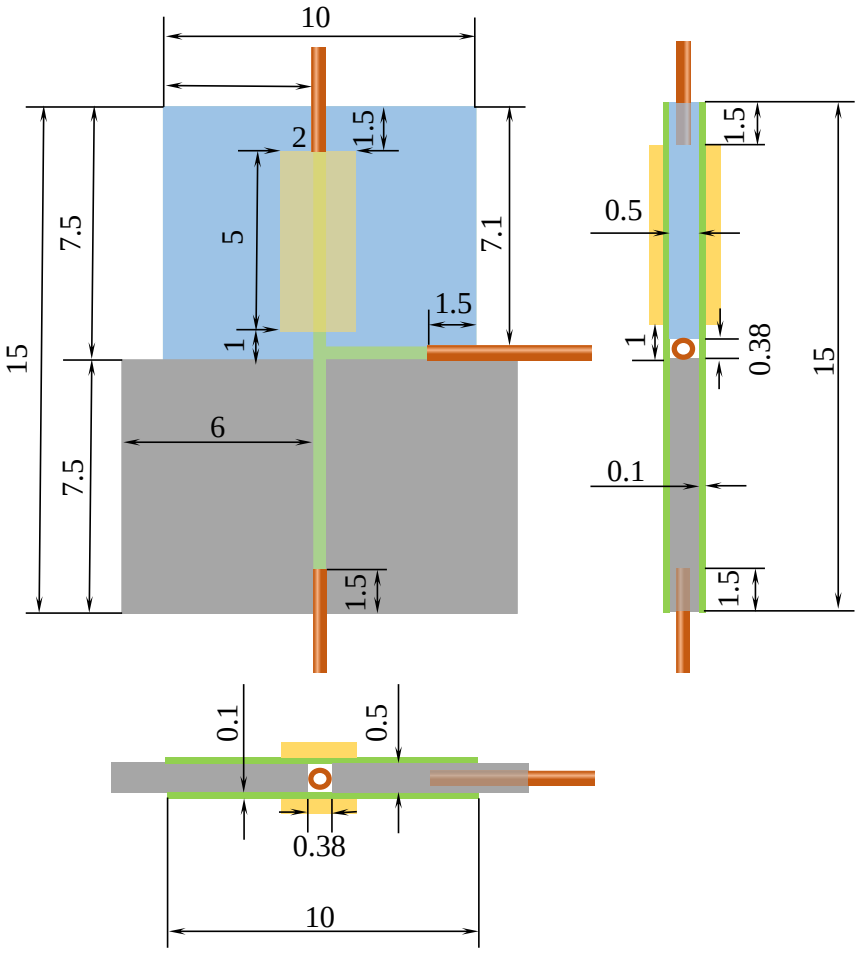

Figure 3.2 3-view diagram of the µHDPID. Units: mm.

To excite helium plasma, a low-cost miniaturized high-voltage high-frequency power supply was developed in-house based on a flyback transformer circuit (shown in Figure 3.3 (A)). It has dimensions of ~5 cm × ~2.5 cm × ~2.5 cm (Figure 3.3 (B)) and weighs about 22 g. With a

1.5 VDC input (257 mA), it outputs 4 kV at 7.7 kHz. The high voltage output and the ground of the power supply were connected to the top and the bottom glass substrates, respectively, via two pieces of copper tape (dimension: 5 mm × 2 mm. See Figure 3.1 (D) and Figure 3.2 for illustration).

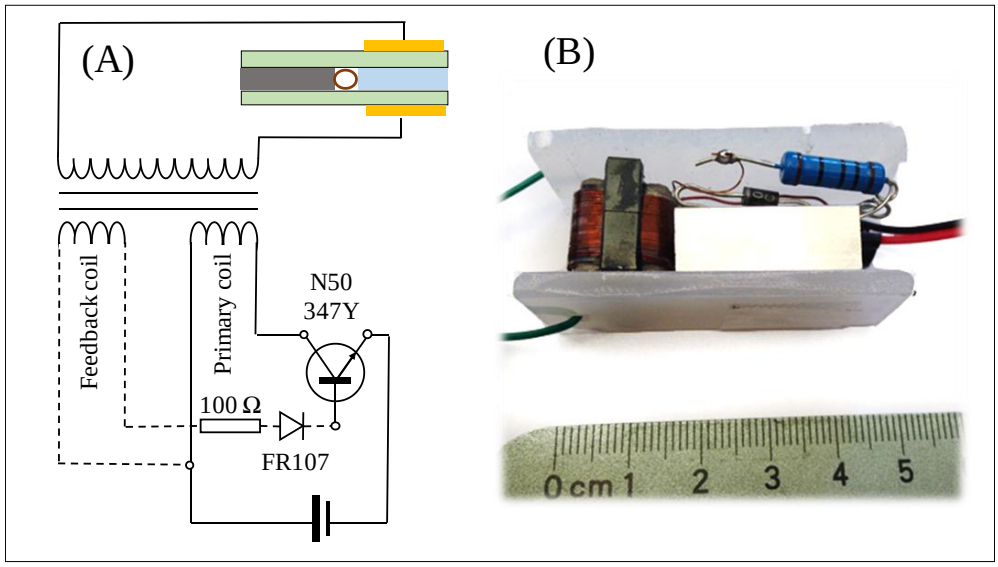

Figure 3.3 (A) Circuitry for helium discharge plasma excitation. DC input: 1.5 V and 257 mA. AC output: 7.7 kHz, 4 kV. (B) Picture of the power supply.

To read signals, a variable DC bias voltage (nominal voltage: 40 VDC) was applied between the collection and the bias electrodes (Figure 3.4). The obtained current was converted to voltage and amplified by an amplifier (Stanford Research Systems SR560, input impedance = 100 MΩ + 25 pF) with a gain of 5 and low pass cutoff frequency of 1 Hz. The final voltage was recorded using LabVIEW^{TM} via a DAQ card (NI USB-6210, National Instruments, Austin, TX) with a digital low pass cutoff frequency of 25 Hz and a data acquisition rate of 14.5 Hz. For this chapter, the operation temperature of the μHDBD-PID is 20 ^{o}C unless otherwise specified.

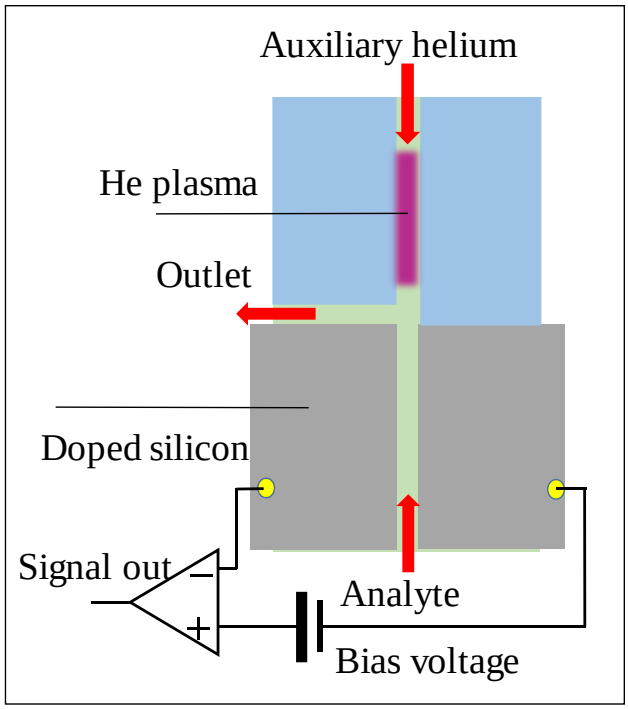

Figure 3.4 Circuitry for signal read-out.

3.2 Experimental section

Methanol (P/N 322415), Pentane (P/N 236705), Carbon tetrachloride (P/N 289116), Heptane (P/N 246654), Benzene (P/N 270709), Toluene (P/N 244511), Ethylbenzene (P/N 03079), p-Xylene (P/N 317195), n-Nonane (P/N 296821), EPA 8260 VOC mix (P/N 500607), Aliphatics mix (C5-C12) (P/N UST157), and Mol Sieve 5A PLOT (P/N 2423) columns for permanent gas separation were all purchased from Sigma-Aldrich (St. Louis, MO) and used without further purification or treatment. Ultrapure helium (99.999%) used as auxiliary gas and carrier gas in all experiments was purchased from Cryogenic Gases (Ann Arbor, MI). GC guard columns (Catalog# 10059), separation columns Rtx®-VMS (Catalog# 19915) and Rtx®-1 (Catalog# 10105) were purchased from Restek Corp. (Bellefonte, Pa).

The experimental setup is illustrated in Figure 3.5. All analytes were injected from the 1177 injector equipped on Varian 3800 GC with a split ratio of 100. A 1 m long guard column was used

to connect the separation column and the μHDBD-PID, unless otherwise specified. The outlet of the μHDBD-PID was connected to a commercial FID equipped on Varian 3800 GC via a short guard column during non-destructive verification only, and was connected to atmosphere at all other times. The auxiliary and carrier gas flow rates were measured at the inlet of the auxiliary channel and analyte channel, respectively, with an Ellutia-6000 GC flowmeter.

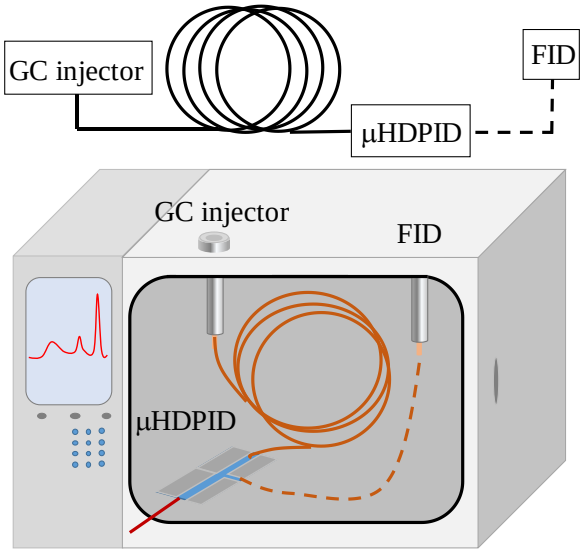

Figure 3.5 Experiment setup.

3.3 Results and discussion

3.3.1 Low voltage and low power operation

The breakdown voltage is propositional to the dietetic layer thickness[34] and the gap between the excitation electrodes[26]. In our design, the dielectric barrier is100 μm thick and the electrodes are 380 μm apart, which enables the onset of helium plasma at a relatively low voltage (4 kV) and low power (385 ± 3 mW, Agilent E3649A, 1.5 VDC at 257 mA).

The power consumption was measured with an unloaded circuit (*i.e.* open circuit test). The actual power consumption of the μHDBD-PID (closed circuit, while generating plasma) differs from the unloaded circuit configuration by 3 mW, which is similar to the theoretically calculated power

dissipation (see "Warm-up time"). It is noted that the μHDBD-PID was designed to operate at room temperature, and the power specified above was mainly for the helium discharge circuit. Extra power is needed if operation at an elevated temperature is desired.

3.3.2 Warm-up time

Low AC voltage and low power consumption also translate to a shorter warm-up time. The helium discharge efficiency depends on a number of factors, such as electrode gap, dielectric barrier thickness, temperature, AC frequency, and voltage. With all other factors fixed, temperature becomes the dominant factor in determining the plasma fluctuation. The longer it takes for the device's temperature to stabilize, the longer the warm-up time.

The excitation electrode geometry in our setup can be modeled as a capacitor. Power dissipation occurs when AC voltage is applied and can be calculated as[35]:

$$P = V^2 \omega C(DF) \tag{3.3.2.1}$$

where P is the dissipated power, V is the applied AC voltage, ω is angular frequency, C is capacitance, and DF is the dissipation factor. At equilibrium, the dissipated power increases device temperature[36]. Using V=4000 V, ω=$2\times \pi \times 7700$ rad/s, C=0.9 pf, and DF=0.003, the dissipated power is ~2 mW, resulting in a very small increase in device temperature and hence quick temperature stabilization. Experiment showed that the temperature of the μHDBD-PID during operation was 20.7 ºC (measured with a Southwire™ 31030s non-contact IR thermometer), only 0.4 ºC above the ambient temperature. Consequently, as shown in Figure 3.6, the μHDBD-PID can be stabilized within 5 minutes.

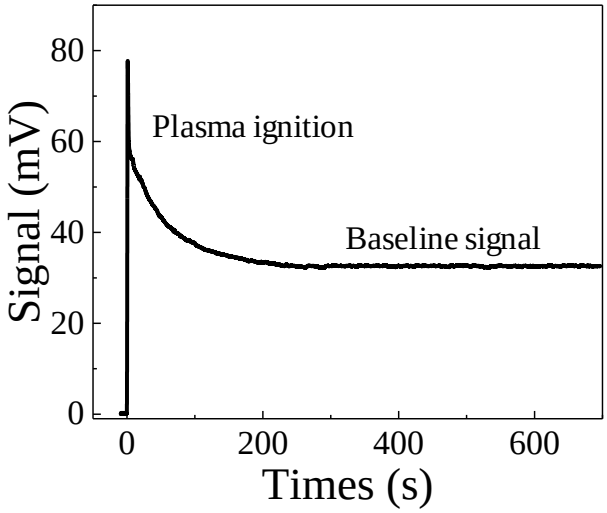

Figure 3.6 Plasma ignition. It took about 5 minutes for the μHDBD-PID to warm up and for the baseline to settle. The baseline level was 32.7 mV and the standard deviation (σ) was 0.153 mV. Bias voltage: 40 V, carrier gas flow rate: 1 mL/min, auxiliary flow pressure: 1 psi, ambient temperature: 20 ºC.

Bias voltage optimization

Following photoionization, analyte ions driven toward the collection electrode by an electric field. Strong electric fields can reduce ion flux traveling time and increase ion collection efficiency by preventing ion recombination and quenching. However, excessive electric field not only increases the noise without proportionally increasing the signal, but also requires more expensive power supplies and other componetns. In order to optimize the bias voltage for the μHDBD-PID, we performed a benchmark using 2.356 ng of heptane. As shown in Figure 3.7, the peak height and the signal-to-noise ratio (SNR) initially increase when the bias voltage is in the range of 10 V to 30 V, and level off when the bias voltage is beyond 40 V. Therefore 40 V is the minimum bias voltage for maximal ion collection efficiency and SNR and was used as the bias voltage for subsequent experiments.

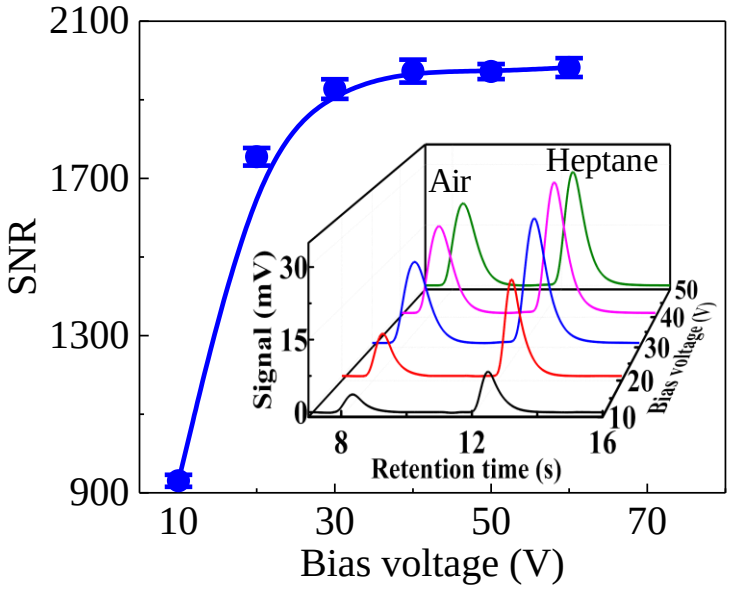

Figure 3.7 Signal to noise ratio (SNR) for 2.356 ng heptane as a function of bias voltage at 20 °C. The response is defined as the peak value of the analyte signal. Carrier gas flow rate was 1 mL/min. Auxiliary flow pressure was 1 psi. 1 m Rtx-1 column was used for air and heptane separation. Error bars were obtained with 4 measurements. Inset: The corresponding chromatogram recorded by the μHDBD-PID. The solid, blue SNR curve is a cubic B-Spline interpolation fit.

3.3.3 Flow dependence

The auxiliary helium flow rate is related to the deep UV plasma intensity[37]: the peak height (*i.e.*, signal) increases with increased auxiliary helium flow rate, as shown in Figure 3.8(A). However, at an excessive auxiliary helium flow rates, plasma jets are generated, accompanied by a drastic increase in the noise level. Consequently, the SNR has a bell shape with a maximum at about 16 mL/min (measured at the auxiliary flow inlet with a corresponding gas source pressure of 3 psi). For further experiments, we used an auxiliary helium flow rate of 5.8 mL/min (measured at the auxiliary flow inlet with a corresponding gas source pressure of 1 psi) in order to reduce helium consumption, while noting that SNR is reduced by 30-40% from maximal SNR (at 16 mL/min).

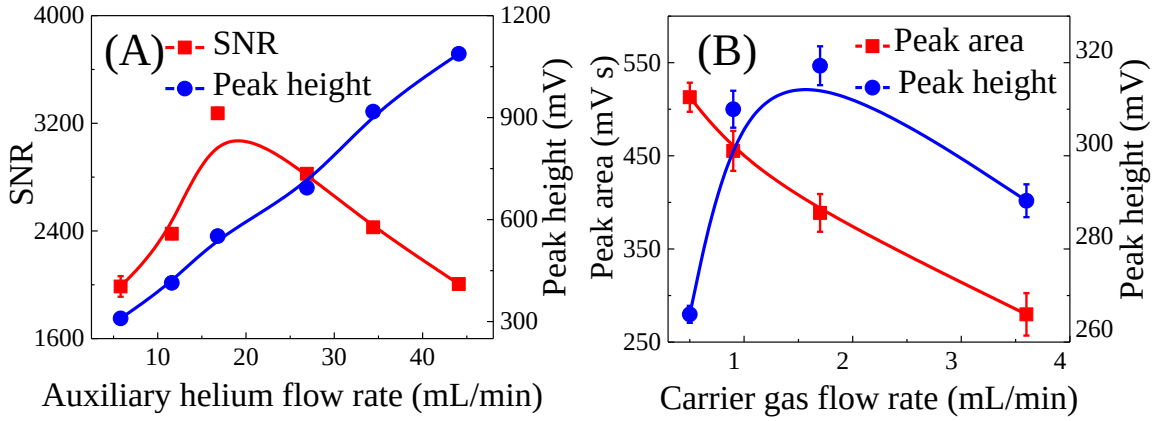

Figure 3.8 (A) Responses (peak heights) and corresponding signal to noise ratios (SNR) for 2.356 ng heptane at various auxiliary helium flow rates. Carrier gas flow was fixed at 1 mL/min. (B) Responses and corresponding signal to noise ratios (SNR) for 2.356 ng heptane at various carrier gas flow rates. Auxiliary helium pressure was fixed at 1 psi. 1 m Rtx-1 column was used for air and heptane separation. The response is defined as the peak value of the analyte. Ambient temperature was 20 ºC. Error bars were obtained with 4 measurements. The solid curves are cubic B-Spline interpolation fits.

At a fixed auxiliary helium inlet pressure (1 psi), changing the carrier gas flow rate also affects the performance of the μHDBD-PID, since the absolute auxiliary helium flow rate decreases when the carrier gas flow increases. Thus, with increased carrier gas flow rates, a slight decrease in the analyte peak area can be observed (see Figure 3.8 (B)) due to decreased plasma emission, as discussed previously. The peak height is also affected by the carrier gas flow rate (Figure 3.8 (B)). Under low carrier flow conditions (*e.g.* 0.5 mL/min), the peak height for a given quantity of analyte is low due to peak broadening resulting from long elution times. On the other hand, at high carrier flow conditions (*e.g.* 3.6 mL/min), the decrease in the auxiliary helium flow rate dominates and the peak height decreases (even though the peak becomes sharper, see Figure 3.9) due to decrease in plasma emission. For the current μHDBD-PID, a maximal peak height was achieved with a carrier flow rate of 1-2 mL/min (Figure 3.8 (B)).

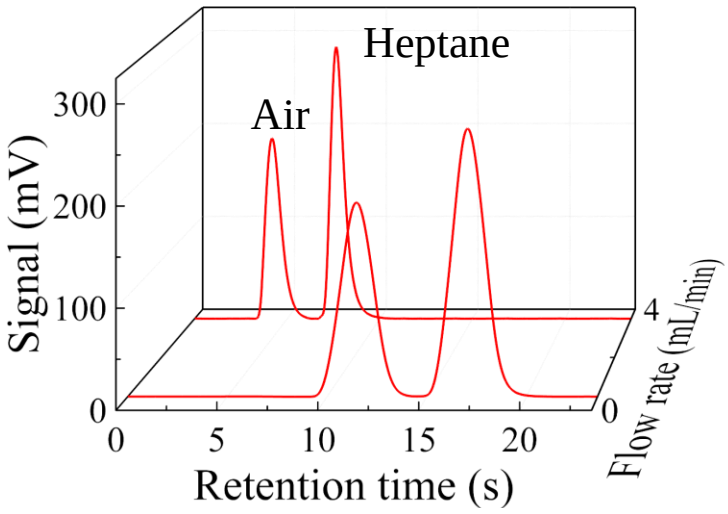

Figure 3.9 Eluted peaks become sharper and elution time becomes shorter at a higher carrier gas flow rates.

Figure 3.9 shows how auxiliary helium flow rate and carrier gas flow rate affect analyte peak height and peak area. Since the auxiliary flow rate is usually adjusted by tuning the gas source pressure, the absolute auxiliary flow rate is affected by the carrier gas flow rate (at a given auxiliary gas source pressure). As a result, GC separation based on pressure ramping[8] cannot be employed if an HDBD-PID is used for quantitative analysis, unless the same auxiliary flow rate can be maintained independently from the carrier gas flow rate during pressure ramping.

3.3.4 Temperature effects

Previous studies have shown that temperature affects helium discharge performance[38]; thus, we benchmarked the new µHDBD-PID under varying temperatures. The µHDBD-PID was heated by a thermoelectric Peltier plate (P/N CP30138 purchased from Digi-Key) from 20 ºC to 80 ºC (maximum operation temperature of the plate) for four cycles. The results shown in Figure 3.10 are highly repeatable in multi-cycle heating processes, attesting to the thermal robustness of the µHDBD-PID. As the temperature increases from 20 ºC to 80 ºC, the peak height of 2.356 ng heptane increases 2.5 times and the noise level increases slightly more, resulting in a 5% decrease

in SNR. In practice, to obtain reliable performance, the temperature of the μHDBD-PID should be kept constant and thermal crosstalk between the separation column and the μHDBD-PID should be avoided when temperature ramping is used in GC separation.

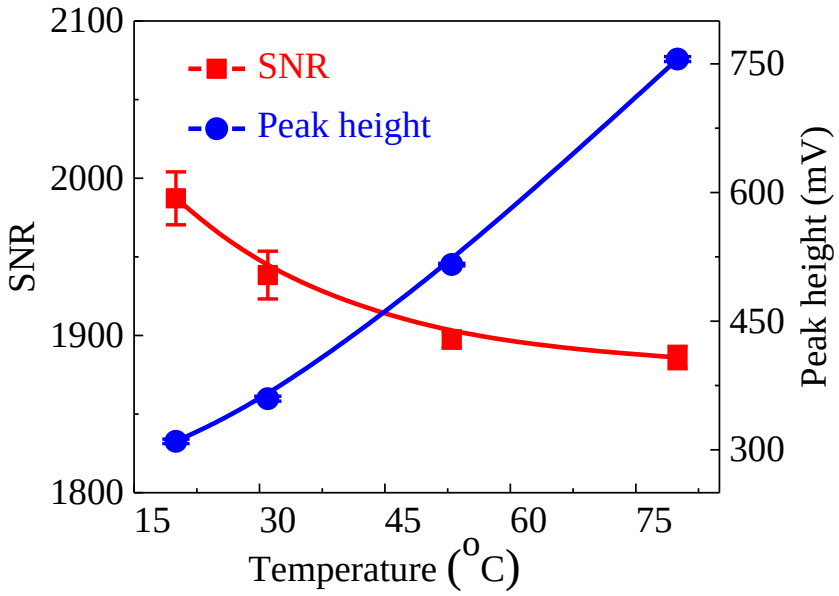

Figure 3.10 Peak height and corresponding signal to noise ratio (SNR) for 2.356 ng heptane as a function of temperature. The response (peak height) is defined as the peak value of the analyte. Carrier gas flow rate was 1 mL/min. Auxiliary flow pressure was 1 psi. 1 m Rtx-1 column was used for air and heptane separation. Error bars were obtained with 4 measurements. Solid curve is a cubic B-Spline interpolation fit.

3.3.5 Response time

Owing to the flow-through design, the μHDBD-PID has a rapid response to analyte signals. A comparison between the μHDBD-PID and a commercial FID is shown in Figure 3.11 (A), showing nearly identical peak widths. The internal chamber volume of the μHDBD-PID was only 1.4 μL, corresponding to an ultimate peak width as sharp as 56 ms (calculated from the gas sweeping time with a 1.5 mL/min flow rate). The dead volume of the μHDBD-PID is estimated to be 6 nL from the COMSOL simulation shown in Fig. 3.11(B), thus the tailing effect is negligible.

We further characterized the response time of the μHDBD-PID in Figure 3.12 using VOCs with lower volatilities (C_8-C_{12}, vapor pressure at 25 °C: ~1500 Pa – 18 Pa). In this case, the μHDBD-PID was placed outside the GC oven at room temperature, and connected to a 7 m long separation column (Rtx®-VMS) via a 1 m long guard column. The commercial FID was directly connected to the same separation column (Rtx®-VMS) and heated to 300 °C. A comparison is given in Fig. S5 and shows no difference in peak widths for C_8-C_{12}. Therefore, our μHDBD-PID can be used at room temperature to analyze VOCs with volatilities higher than C_{12} (vapor pressure=187 Pa at 25 °C), which reduces energy required for detector heating. Later, we will show that our μHDBD-PID is able to detect VOCs with even lower vapor pressures without condensation occurring (see "Application to GC separation").

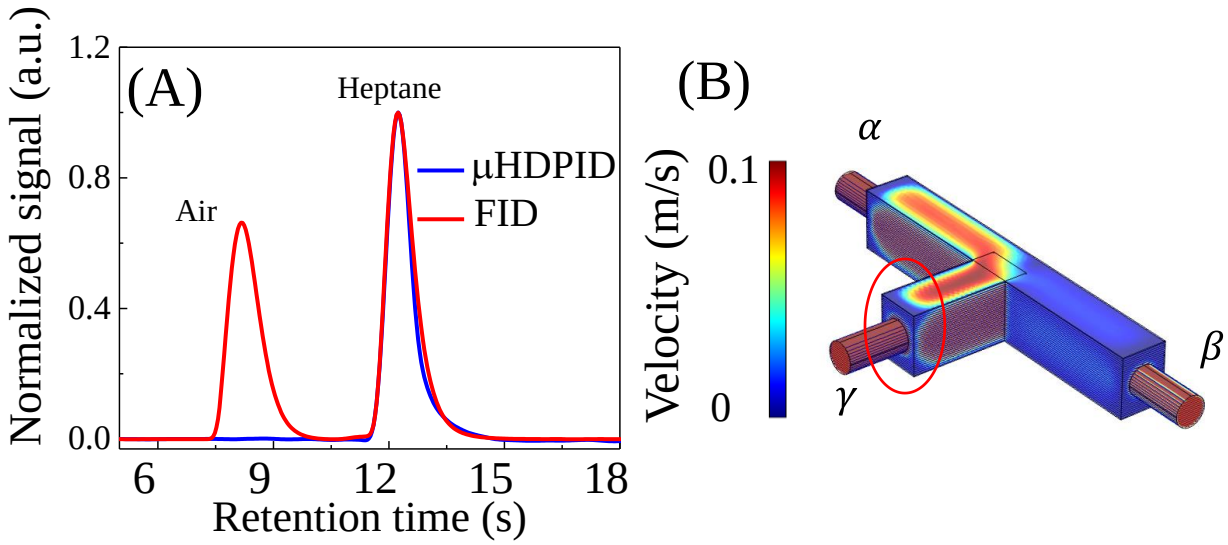

Figure 3.11 (A) Normalized signal obtained with μHDBD-PID and FID. Carrier gas flow rate was 1 mL/min. Auxiliary flow pressure was 1 psi. FWHMs of 0.85 s and 0.72 s were obtained for μHDBD-PID and FID, respectively. 1 m Rtx-1 column was used for air and heptane separation. (B) COMSOL Multiphysics® 3D simulation of helium flow with an auxiliary helium flow rate of 5.8 mL/min from inlet α and a carrier gas flow rate of 1 mL/min from inlet β. Outlet γ serves as a common outlet with a pressure of 101.35 kPa. The internal chamber volume is estimated to be 1.4 μL and the dead volume, defined as the region having a helium flow velocity less than 0.1 m/s, is estimated to be 6 nL (see the circled part).

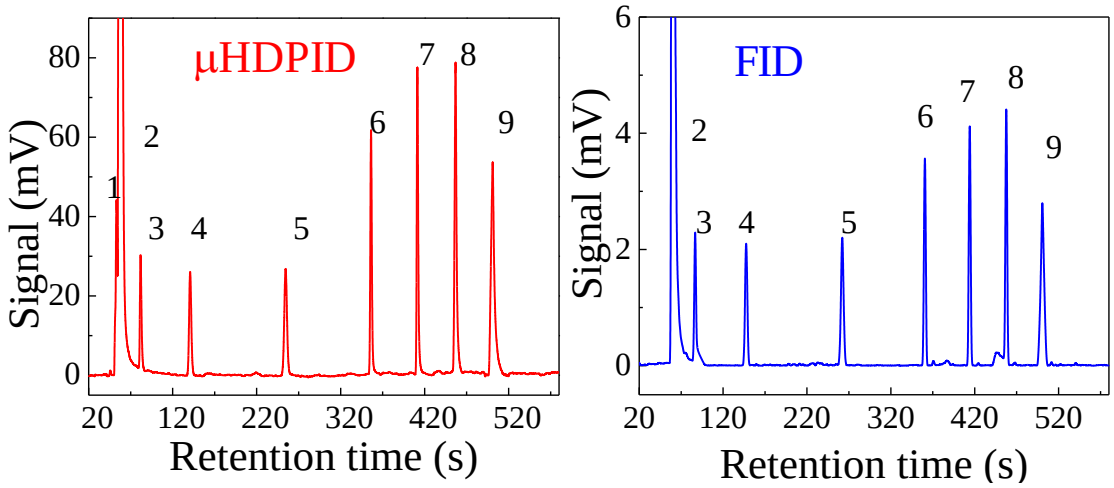

Figure 3.12 0.1 µL (100 split ratio) aliphatic mixture (C_5-C_{12}) was detected by µHDPID and FID, respectively. The mixture was separated via a 7-m long Rtx®-VMS column at a flow rate of 1.5 mL/min with temperature ramping from T=40 ºC for 2 min to 200 ºC at a rate of 30 ºC/min. 1. Water, 2. Methanol and Pentane, 3. Hexane, 4. Heptane, 5. Octane, 6. Nonane, 7. Decane, 8. Undecane, 9. Dodecane. FWHMs of Dodecane for µHDPID and FID were 4.06 s and 4.14 s, respectively.

3.3.6 Linearity

For accurate quantitative analysis, a linear µHDBD-PID response is desirable. Peak height response curves of eights representative analytes with injection masses ranging from few tens of pg to few tens of ng (limited by the sample capacity of the separation column, which is a couple hundred ng) were obtained. Results are shown in Figures 3.13 and 3.14 and show high linearity (see Table 3.2 for linear regression parameters). Considering the detection limit of only a few pg for the above analytes (see next section) a linear dynamic range of more than 4 orders of magnitude can be obtained.

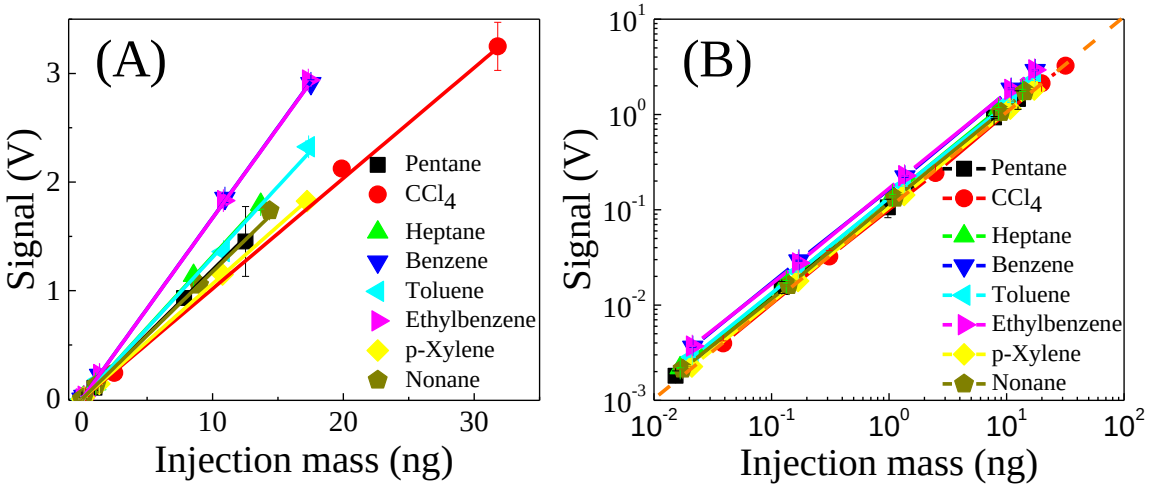

Figure 3.13 μHDBD-PID linearity experiment for eight VOCs. (A) Peak height as a function of injection mass using a linear-linear scale. Solid curves are linear fits with related parameters given in Table 3.2. (B) Corresponding data and curves in (A) plotted using a log-log scale. The dashed line has a slope of unity. The slope of each curve is 0.9979, 1.0205, 1.00103, 0.99626, 0.99403, 0.99491, 0.99807, 0.99845 from Pentane to Nonane, respectively. Error bars were obtained with 4 measurements. Auxiliary flow pressure was 1 psi.

Table 3.2 Linear regression parameters for signal vs mass curves of eight VOCs with intercepts set to zero.

	Slope	Adjusted R	P-value
Pentane	0.1191	0.9998	7.81E-04
Carbon tetrachloride	0.1017	0.9978	2.15E-03
Heptane	0.1317	0.9999	3.96E-04
Benzene	0.1681	0.9997	1.31E-03
Toluene	0.1321	0.9992	1.64E-03
Ethylbenzene	0.1698	0.9992	2.21E-03
p-Xylene	0.1068	0.9999	3.35E-04
Nonane	0.1189	0.9993	1.45E-03

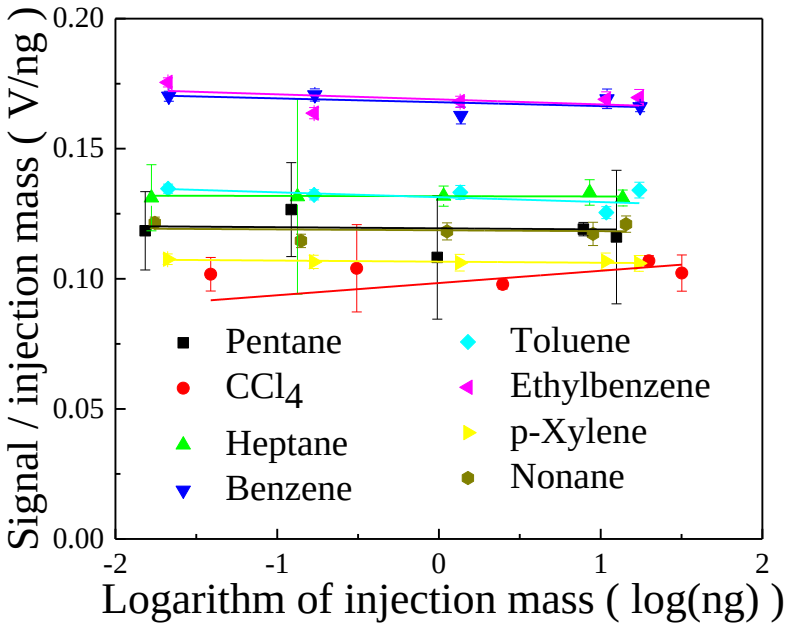

Figure 3.14 Plot of peak height divided by injection mass as a function of logarithm of injection mass for eight VOCs with data calculated from Fig. 3.13. The slopes of each curve are: Pentane (-4.27×10^{-4}), CCl_4 (4.7×10^{-3}), Heptane (-1.06×10^{-4}), Benzene (-1.48×10^{-3}), Toluene (1.87×10^{-3}), Ethylbenzene (-1.94×10^{-4}), p-Xylene (-4.21×10^{-4}), Nonana (-3.35×10^{-4}).

3.3.7 Detection limit

The detection limit was calculated based on minimum injection mass results from the above linearity tests (see Figure 3.15, the limit was taken at 3 standard deviations above the noise level). The detection limits and physical properties of the eight VOCs are given in Table 3.3.

Table 3.3 Detection limit parameters and physical properties[39] of eight VOCs.

VOC	DL[a]	IP[b]	PH[c]	SD[d]
Pentane	4.6	10.35	1.81	0.3
CCl_4	5.3	11.47	3.95	0.25
Heptane	4.2	10.08	2.19	0.21
Benzene	3.2	9.25	3.64	0.04
Toluene	4.0	8.82	2.85	0.04

Ethylbenzene	3.1	8.76	3.71	0.03
p-Xylene	5.1	8.56	2.26	0.04
n-Nonane	4.5	9.72	2.13	0.04

[a]Detection limit at 3σ (pg), $\sigma = 0.18$ mV. [b]Ionization potential (eV). [c]Peak height (mV). [d]Standard deviation of peak height (mV).

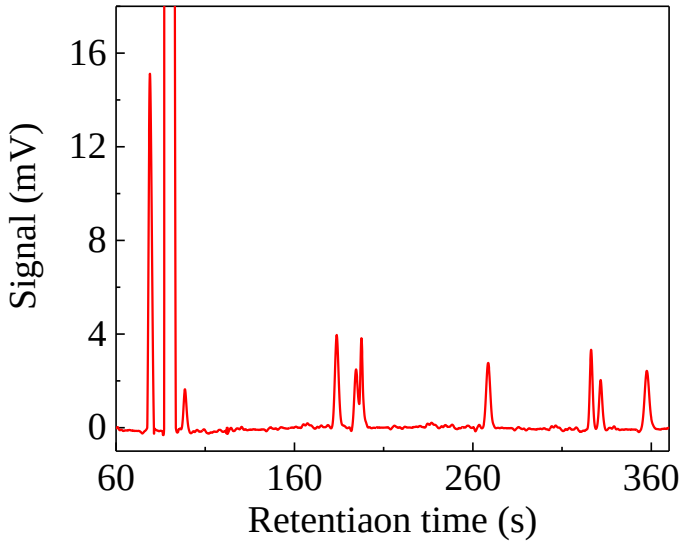

Figure 3.15 μHDPID detection of VOC mixtures prepared in methanol with 195 ppm (V/V) concentration for all eight VOCs. The mixture was separated by GC using a 7-m long Rtx®-VMS column. The injected mass and FWHM were: 1. Water (trace, 2.00 s); 2. Methanol (N/A, 2.01 s); 3. Pentane (15.28 pg, 1.84 s); 4. Carbon tetrachloride (38.83 pg, 2.33 s); 5. Heptane (16.7 pg, 2.34 s); 6. Benzene (21.39 g, 1.52 s); 7. Toluene (21.17 pg, 2.58 s); 8. Ethylbenzene (21.14 pg, 1.79 s); 9. p-Xylene (21.02 pg, 1.98 s); 10. n-Nonane (17.53 pg, 2.91 s). Temperature ramping: T=25 ºC for 0.6 min and then to 200 ºC at a rate of 30 ºC/min. Helium was used as the carrier gas at a flow rate of 1.5 mL/min.

We have specifically designed our μHDBD-PID to help improve the detection limit. The analyte channel and helium discharge channel in the μHDBD-PID are fluidically separated (see Figure 3.11 (B)), which prevents analyte dilution caused by incoming auxiliary flow. Furthermore, the μHDBD-PID electrodes are composed of the entire sidewall of the p-type silicon wafers. Such a long electrode (6 mm) along the UV illumination pathway increases the collection area and facilitates the low detection limit. This is similar to recent studies[10, 25], in which multiple collection

electrodes were used to improve the sensitivity. Finally, the small gap of only 380 µm between the two electrodes ensures efficient collection of ions and electrons generated by photoionization.

3.3.8 Application to GC separation

In Figures 3.16 and 3.17, the overall performance of the µHDBD-PID was tested by detection of permanent gases and EPA 8260 standard reagent, respectively. The mixture of permanent gases (hydrogen, nitrogen, and oxygen) was prepared in a Tedlar® bag with an arbitrary volume ratio and separated with a PLOT column. Even though the ionization potential of nitrogen is 15.58 eV, it can still be ionized and detected by the µHDBD-PID, which substantiates the universal applicability of our detector. There are 52 VOCs in the EPA 8260 standard reagent. Figure 3.17 compares an FID and the µHDBD-PID, showing that 47 peaks are detected by both detectors (see also Figure 3.18 for model peaks). Except for some coeluted compounds, all separated eluents exhibit a symmetric peak shape and comparable peak width for both detectors. Additionally, an enlarged view of the EPA 8260 chromatogram (Figure 3.19) shows that peak widths between FID and µHDBD-PID detection in the semivolatile range are similar. Therefore, the µHDBD-PID can be used to detect some semivolatile compounds without heating.

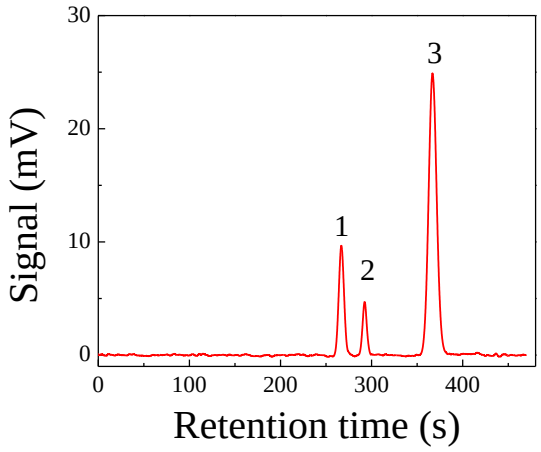

Figure 3.16 µHDBD-PID detection of permanent gases: 1. Hydrogen (30% V/V); 2. Oxygen (10% V/V); and 3. Nitrogen (60% V/V), with a total injection volume of 10 µL via gas-tight

syringes with shut-off valves (50R-V-GT SGE) and a spilt ratio of 100. Separation was achieved by using a 30 m Mol Sieve 5A PLOT column (320 µm ID and average coating thickness of 15 µm) at a helium flow rate of 1 mL/min and under isothermal conditions (35 ºC).

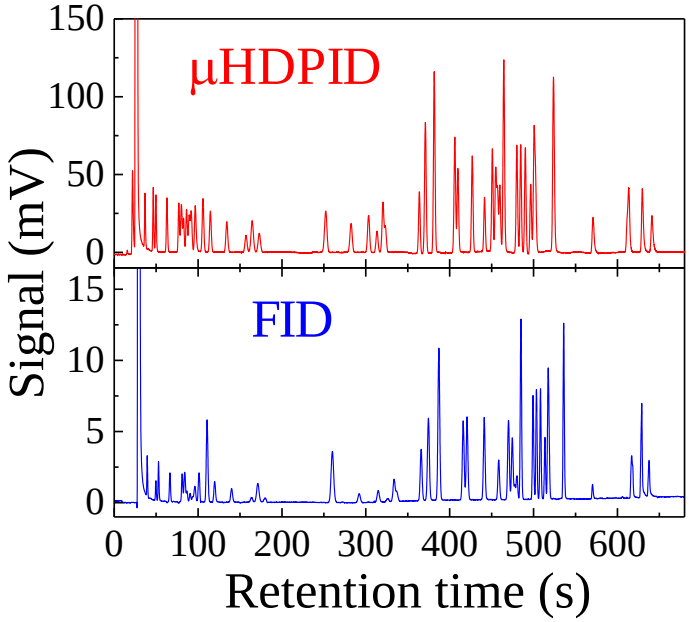

Figure 3.17 Detection of 0.1 µL (with a 100-split ratio) EPA 8260 VOC mixture (purchased from Sigma-Aldrich P/N 500607, containing 52 analytes) with 47 VOC peaks obtained by both µHDBD-PID and FID. The five remaining VOCs were missing due to co-elution. Separation was achieved by using a using a 7-m long Rtx®-VMS column at a carrier flow rate of 1 mL/min. Temperature ramping: T=35 ºC for 4 min to 160 ºC at a rate of 18 ºC/min.

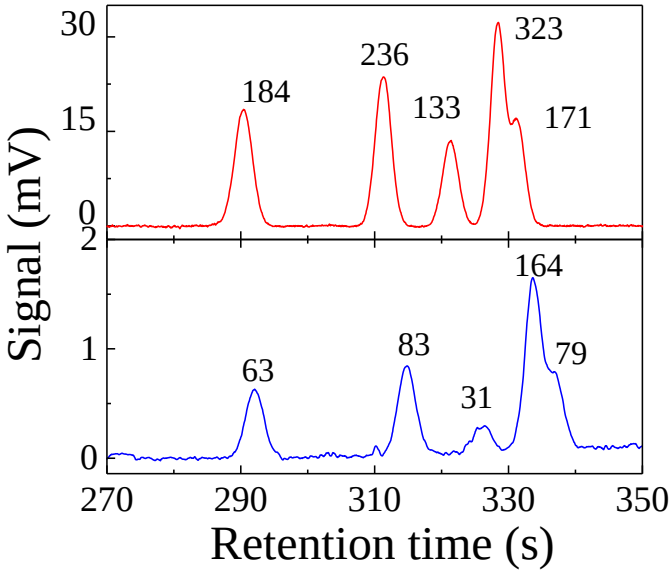

Figure 3.18 Enlarged peaks from Figure 3.17 with SNR labeled on corresponding peaks. Slight offset in peak elution times between the HDBD-PID and FID result from a slight difference in temperature ramping during the two separations.

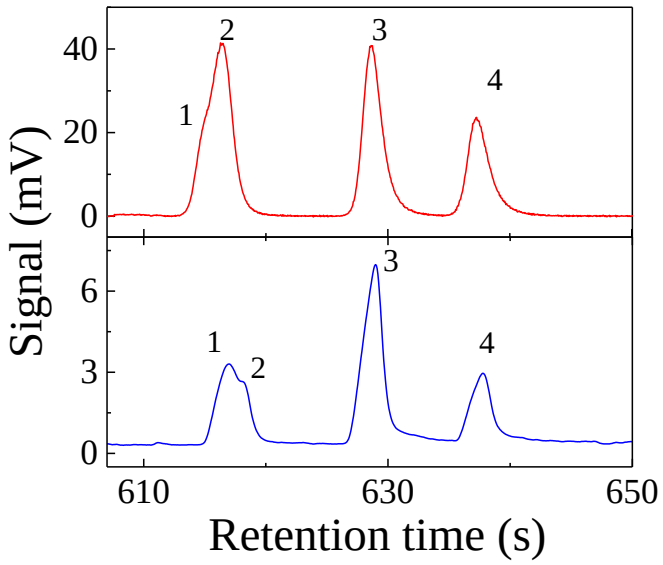

Figure 3.19 Enlarged peaks from Figure 3.17. Identified peaks and FWHM values of HDBD-PID and FID were: 1. Hexachloro-1,3-butadiene (NA/NA), 2. 1,2,4-trichlorobenzene (NA/NA), 3. Naphthalene (1.78 s / 1.95 s), 4 1,2,3-trichorobenzene (1.93 s / 2.14 s). Slight offset in the peak elution times between the HDBD-PID and FID results from a slight difference in temperature ramping during the two separations.

3.3.9 Non-destructive and long-term operation evaluation

We tested the non-destructive nature of the μHDBD-PID by connecting the FID to the μHDBD-PID via a 40 cm long guard column (Figure 3.20). The peak height of the FID was taken with μHDBD-PID plasma "ON" and "OFF" and found to be same for both cases (using a t-test). Finally, the μHDBD-PID exhibited excellent robustness with no failure observed during operation for three weeks.

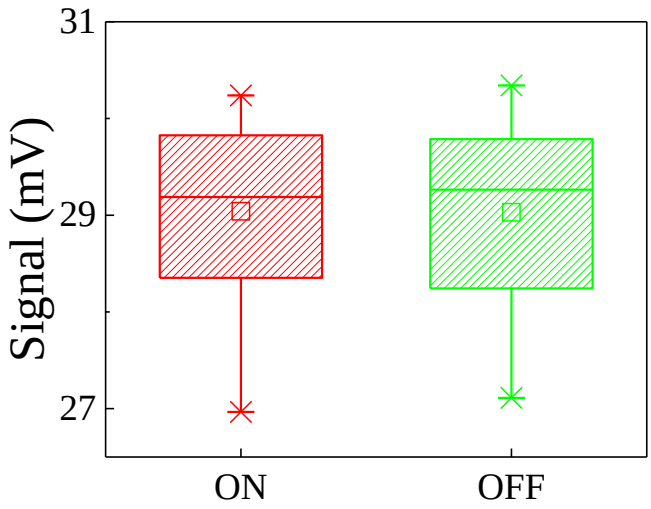

Figure 3.20 Testing of non-destructive nature of the μHDBD-PID. Boxplot of 15 injections of 2.356 ng heptane under the plasma "ON" and "OFF" conditions. A p-value of 0.9779 was calculated using an unpaired two sample t-test for equal population means with the same sample size.

3.4 Conclusion

In this chapter we demetreate the development of a novel μHDBD-PID that exhibits superior characteristics and performance in size, weight, ease of fabrication, cost, power consumption, detection limit, dynamic range, response time, and detector lifetime. It can be broadly used in portable and micro-GC systems for *in situ*, real time, and high sensitivity gas analysis.

3.5 References

1. Driscoll, J. N., Evaluation of a new photoionization detector for organic compounds. *Journal of Chromatography A* **1977,** *134* (1), 49-55.
2. Zhu, H.; Nidetz, R.; Zhou, M.; Lee, J.; Buggaveeti, S.; Kurabayashi, K.; Fan, X., Flow-through microfluidic photoionization detectors for rapid and highly sensitive vapor detection. *Lab on a Chip* **2015,** *15* (14), 3021-3029.
3. Zhou, M.; Lee, J.; Zhu, H.; Nidetz, R.; Kurabayashi, K.; Fan, X., A fully automated portable gas chromatography system for sensitive and rapid quantification of volatile organic compounds in water. *RSC Advances* **2016,** *6* (55), 49416-49424.
4. Lee, J.; Zhou, M.; Zhu, H.; Nidetz, R.; Kurabayashi, K.; Fan, X., In situ calibration of micro-photoionization detectors in a multi-dimensional micro-gas chromatography system. *Analyst* **2016**.
5. Forsyth, D. S., Pulsed discharge detector: theory and applications. *Journal of Chromatography A* **2004,** *1050* (1), 63-68.
6. Jin, Q.; Yang, W.; Yu, A.; Tian, X.; Wang, F., Helium direct current discharge ionization detector for gas chromatography. *Journal of Chromatography A* **1997,** *761* (1), 169-179.
7. Narayanan, S.; Rice, G.; Agah, M., Characterization of a micro-helium discharge detector for gas chromatography. *Sensors and Actuators B: Chemical* **2015,** *206*, 190-197.
8. Akbar, M.; Shakeel, H.; Agah, M., GC-on-chip: integrated column and photoionization detector. *Lab on a Chip* **2015,** *15* (7), 1748-1758.
9. Lasa, J.; Mochalski, P.; Pusz, J., Evaluation of a pulse-discharge helium ionisation detector for the determination of neon concentrations by gas chromatography. *Journal of Chromatography A* **2004,** *1035* (2), 261-264.
10. Cai, H.; Stearns, S. D., Pulsed discharge helium ionization detector with multiple combined bias/collecting electrodes for gas chromatography. *Journal of Chromatography A* **2013,** *1284*, 163-173.
11. Cai, H.; Wentworth, W. E.; Stearns, S. D., Characterization of the pulsed discharge electron capture detector. *Analytical chemistry* **1996,** *68* (7), 1233-1244.
12. Gremaud, G.; Wentworth, W.; Zlatkis, A.; Swatloski, R.; Chen, E.; Stearns, S. D., Windowless pulsed-discharge photoionization detector application to qualitative analysis of volatile organic compounds. *Journal of chromatography A* **1996,** *724* (1), 235-250.
13. Mowry, C. D.; Pimentel, A. S.; Sparks, E. S.; Moorman, M. W.; Achyuthan, K. E.; Manginell, R. P., Pulsed Discharge Helium Ionization Detector for Highly Sensitive Aquametry. *Analytical Sciences* **2016,** *32* (2), 177-182.
14. Sun, K.; Wentworth, W. E.; Stearns, S. D., Development and characterization of chlorine-selective pulsed discharge emission detector for gas chromatography. *Journal of Chromatography A* **2000,** *872* (1), 141-165.
15. Winniford, B. L.; Sun, K.; Griffith, J. F.; Luong, J. C., Universal and discriminative detection using a miniaturized pulsed discharge detector in comprehensive two-dimensional GC. *Journal of separation science* **2006,** *29* (17), 2664-2670.
16. Wentworth, W. E.; Huang, J.; Sun, K.; Zhang, Y.; Rao, L.; Cai, H.; Stearns, S. D., Non-radioactive electron-capture detector. *Journal of Chromatography A* **1999,** *842* (1–2), 229-266.
17. Wentworth, W. E.; Cai, H.; Stearns, S., Pulsed discharge helium ionization detector universal detector for inorganic and organic compounds at the low picogram level. *Journal of Chromatography A* **1994,** *688* (1), 135-152.

18. Wentworth, W. E.; D'Sa, E. D.; Cai, H.; Stearns, S., Environmental Applications of the Pulsed-Discharge Electron-Capture Detector. *Journal of Chromatographic Science* **1992,** *30* (12), 478-485.
19. Han, B.; Jiang, X.; Hou, X.; Zheng, C., Dielectric barrier discharge carbon atomic emission spectrometer: universal GC detector for volatile carbon-containing compounds. *Analytical chemistry* **2013,** *86* (1), 936-942.
20. Li, C.; Jiang, X.; Hou, X., Dielectric barrier discharge molecular emission spectrometer as gas chromatographic detector for amines. *Microchemical Journal* **2015,** *119*, 108-113.
21. Li, W.; Zheng, C.; Fan, G.; Tang, L.; Xu, K.; Lv, Y.; Hou, X., Dielectric barrier discharge molecular emission spectrometer as multichannel GC detector for halohydrocarbons. *Analytical chemistry* **2011,** *83* (13), 5050-5055.
22. Meyer, C.; Müller, S.; Gurevich, E.; Franzke, J., Dielectric barrier discharges in analytical chemistry. *Analyst* **2011,** *136* (12), 2427-2440.
23. Bogaerts, A.; Neyts, E.; Gijbels, R.; van der Mullen, J., Gas discharge plasmas and their applications. *Spectrochimica Acta Part B: Atomic Spectroscopy* **2002,** *57* (4), 609-658.
24. Narayanan, S.; Rice, G.; Agah, M., A micro-discharge photoionization detector for micro-gas chromatography. *Microchimica Acta* **2014,** *181* (5-6), 493-499.
25. Manginell, R. P.; Mowry, C. D.; Pimentel, A. S.; Mangan, M. A.; Moorman, M. W.; Sparks, E. S.; Allen, A.; Achyuthan, K. E., Development of a Mesoscale Pulsed Discharge Helium Ionization Detector for Portable Gas Chromatography. *Analytical Sciences* **2015,** *31* (11), 1183-1188.
26. Yu, B. G.; Maiorov, V. A.; Behnke, J.; Behnke, J. F., Modelling of the homogeneous barrier discharge in helium at atmospheric pressure. *Journal of Physics D: Applied Physics* **2003,** *36* (1), 39.
27. Na, N.; Zhang, C.; Zhao, M.; Zhang, S.; Yang, C.; Fang, X.; Zhang, X., Direct detection of explosives on solid surfaces by mass spectrometry with an ambient ion source based on dielectric barrier discharge. *Journal of mass spectrometry* **2007,** *42* (8), 1079-1085.
28. Gras, R.; Luong, J.; Monagle, M.; Winniford, B., Gas Chromatographic Applications with the Dielectric Barrier Discharge Detector. *Journal of Chromatographic Science* **2006,** *44* (2), 101-107.
29. Na, N.; Zhao, M.; Zhang, S.; Yang, C.; Zhang, X., Development of a Dielectric Barrier Discharge Ion Source for Ambient Mass Spectrometry. *Journal of the American Society for Mass Spectrometry* **2007,** *18* (10), 1859-1862.
30. Kuklya, A.; Engelhard, C.; Uteschil, F.; Kerpen, K.; Marks, R.; Telgheder, U., Low-Temperature Plasma Ionization Differential Ion Mobility Spectrometry. *Analytical Chemistry* **2015,** *87* (17), 8932-8940.
31. Jafari, M. T., Low-Temperature Plasma Ionization Ion Mobility Spectrometry. *Analytical Chemistry* **2011,** *83* (3), 797-803.
32. Andrade, F. J.; Shelley, J. T.; Wetzel, W. C.; Webb, M. R.; Gamez, G.; Ray, S. J.; Hieftje, G. M., Atmospheric Pressure Chemical Ionization Source. 1. Ionization of Compounds in the Gas Phase. *Analytical Chemistry* **2008,** *80* (8), 2646-2653.
33. Shinada, K.; Horiike, S.; Uchiyama, S.; Takechi, R.; Nishimoto, T., Development of new ionization detector for gas chromatography by applying dielectric barrier discharge. *Shimadzu Hyoron* **2012,** *69*, 255-263.

34. Guangliang, S.; Wenzheng, L.; Chuanhui, L.; Rongrong, Z., The generation characteristics of dielectric barrier glow discharge plasma in air. *Journal of Physics: Conference Series* **2013,** *441* (1), 012023.
35. Johnson, G. L., Solid State Tesla Coil. *Inductors and Transformers: Kansas State University* **2001**.
36. Corke, T. C.; Enloe, C. L.; Wilkinson, S. P., Dielectric barrier discharge plasma actuators for flow control*. *Annual Review of Fluid Mechanics* **2010,** *42*, 505-529.
37. Cheng, X.; Sherman, J.; Murphy, W.; Ratovitski, E.; Canady, J.; Keidar, M., The Effect of Tuning Cold Plasma Composition on Glioblastoma Cell Viability. *PLoS ONE* **2014,** *9* (5), e98652.
38. Ravi, V.; Mok, Y. S.; Rajanikanth, B. S.; Kang, H.-C., Temperature effect on hydrocarbon-enhanced nitric oxide conversion using a dielectric barrier discharge reactor. *Fuel Processing Technology* **2003,** *81* (3), 187-199.
39. Haynes, W. M., *CRC handbook of chemistry and physics*. CRC press: 2014.

Chapter 4 Rapid and Sensitive Detection of Formaldehyde Using Portable 2-dimensional Gas Chromatography Equipped with Photoionization Detectors

The content in Chapter 4 has been adapted from the following manuscript which will be submitted in the future: Hongbo Zhu, Jinyan She, Menglian Zhou and Xudong Fan

4.1 Introduction

Air pollution is a major environmental concern to human health. Indoor air pollution has an especially significant impact due to higher accumulation level of toxic volatile organic compounds (VOCs)[1]. Formaldehyde is one of the most common polluting VOCs, whose presence can be due to smoking, cooking, heating, decoration materials, furniture finishing, and chemical reactions between VOCs and ozone[2]. Formaldehyde can cause symptoms such as burning sensations in the eyes, nose, and throat, coughing, wheezing, nausea, and skin irritation by short-term exposure[3], and can be carcinogenic with long-term exposure[4]. Therefore, health and environmental organizations (*e.g.*, World Health Organization (WHO), US National Institute for Occupational Safety and Health (NIOSH), and California Air Resources Board) have established regulated exposure limits, which are summarized in Table 4.1.

Table 4.1 Regulated formaldehyde exposure limits.

Institution	Regulated exposure limit ppb (V/V)	Remarks
National Institute for Occupational Safety and Health (USA)	16[I]	Time weighted average (TWA) concentrations for up to a 10-hour workday during a 40-hour workweek
	100[II]	No more than 15 minute exposure at any time during a day
	750[III]	Eight hour TWA, an average exposure value over an eight hour work shift.

Occupational Safety and Health Administration (USA)	2000[II]	Average value over 15 minutes of exposure
American Conference of Governmental Industrial Hygienists	300[IV]	Recommended ceiling, not to be exceeded at any time during a day
World Health Organization	81	Maximum level in non-occupational settings
California Air Resources Board	2[V]	

I, Recommended exposure limit
II, Ceiling, should not be exceeded
III, Permissible exposure limits, maximum concentrations of chemicals to which a worker may be exposed
IV, Threshold limit values, guidelines for the level of exposure that the typical worker can be exposed to without adverse health effects.
V, Chronic reference exposure limit

To date, a number of analytical methods, such as spectrophotometry[5], high-performance liquid chromatography[6], GC coupled with mass spectrometry (GC/MS)[7-8], and fluorimetry[9] have been developed for formaldehyde detection. While capable of obtaining accurate and repeatable results, these instruments suffer from bulky size, complicated processes (such as derivatization), and/or inability for real-time on-site measurement. Few portable devices are currently available for on-site formaldehyde detection. A handheld formaldehyde detector based on an electrochemical thin-film metal oxide sensor has a reasonably good detection limit (ppb level) and quick response time (6 s of rise time to reach 90% of the maximum response and 6 s of recovery time to decrease to 10% of the maximum response)[10]. However, because of poor selectivity, this type of device often produces false positives, particularly with high VOC backgrounds, and requires frequent calibration. Paper-based colorimetric measurement is simple, low cost, and user-friendly[11] , but suffers from limited shelf time and imprecise measurement results. To overcome these issues, miniaturized spectrophotometers[12-14] and fluorometers[13] have been developed.

However, these devices require manual operation and special reaction reagents, which are cumbersome and limit their capability to detect multiple VOCs.

In order to provide better capabilities for rapid on-site monitoring of air quality (particularly formaldehyde), we developed an automated, miniaturized, heart-cutting two-dimensional (2-D) GC. In this device, the first-dimensional GC column was coupled to the second-dimensional GC column via a micro-Deans switch. A flow-through micro-photoionization detector (μPID) and a micro-helium dielectric barrier discharge photoionization detector (μHDBD-PID) were installed at the end of first- and second-dimensional columns, respectively. Owning to the high photon energy (up to 17.5 eV) of the μHDBD-PID, formaldehyde, which was cut from the first-dimensional column into the second-dimensional column, can be detected directly without complicated derivatization processes used in traditional GC methods. Other air quality related VOCs (such as benzene, toluene, ethylbenzene, and xylene) can be separated by the first-dimensional column and subsequently detected by the μPID. The device is highly portable (weight: 1.3 kg, dimensions: 27 cm x 24 cm x 12 cm) and is capable of detecting formaldehyde down to 0.5 ppb (V/V) with a signal-to-noise ratio of 6 in only 11 minutes (including 6 minutes of sampling time).

4.2 Materials

Analytes and glass beads (212 ~ 300 μm i.d., used for the flow resistor) were purchased from Sigma-Aldrich (St. Louis, MO) and used without further purification. Adsorbent materials Carbopack™ X (P/N 10437-U), Carbopack™ B (P/N 20273), and Carboxen® 1000 (P/N 10478-U) were obtained from Supelco (Bellefonte, PA). The micro two-port (P/N LHDB1252115H) and three-port valves (P/N LHDA1221311H) were purchased from Lee Company (Westbrook, CT). The K-type thermocouple (P/N SA3-K) was obtained from Omega Engineering (Stamford, CT). The capillary GC

column Rtx®-VMS (5 m x 0.25 mm i.d., 1.4 μm film thickness), Rt® Q-BOND (3 m x 0.32 mm i.d., 10 μm film thickness), deactivated fused silica capillary (0.53 mm i.d.), and universal quick seal connectors were obtained from Restek (Bellefonte, PA). A data acquisition card, USB-6003 OEM (16 bits), was purchased from National Instruments (Austin, TX). A mini-diaphragm pump was purchased from Parker Hannifin (P/N E134-11-120, Cleveland, OH). DI water was purified by a Milli-Q water purification system (Thermo Fisher Scientific, Wayne, MI). Ultrapure helium (99.999%) used as auxiliary and system carrier gas was purchased from Cryogenic Gases (Ann Arbor, MI). Nickel 200 wire (26 AWG) and Nichrome 80 wire (32 AWG) used as heating wires for the capillary column and preconcentrator, respectively, were purchased from Newegg (Industry, CA).

4.3 Methods

4.3.1 System layout

Figure 4.1 A illustrates the layout of the GC device. It was housed in the plastic box shown in Figure 4.1 B, which had compact dimensions of 27 cm x 24 cm x 12 cm and weighed around 1.3 kg. A power adapter with a maximum output of 45 W provided 24 V DC for the entire device. The DC-DC converters and MOSFET modules were integrated on a home-made printed circuit board to power and control electrical components, such as valves, pump, μPID, μHDBD-PID, preconcentrator, thermal injector, and heaters on the GC columns. The average power consumption of the entire device was about 25 W. A LabView™ program was developed for automated operation and data processing, including sampling, sample injection, gas flow routing, column temperature control, and data acquisition, processing, and storage.

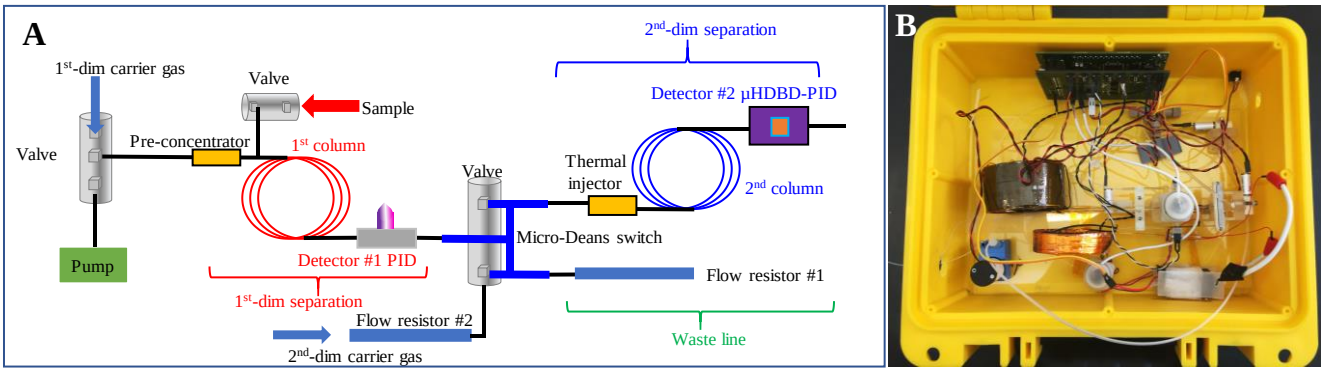

Figure 4.1 (A) Layout of the portable 2-D heart cutting GC. (B) Picture of the device housed in a plastic box with dimensions of 27 cm x 24 cm x 12 cm. It weighed 1.3 kg excluding the helium cartridge.

4.3.2 GC columns

The columns used in this system were 5 m Rtx®-VMS and 3 m Rt® Q-BOND for the first- and second-dimensional separation, respectively. The GC column was wrapped by a heat shrinkable tube along with a Nickel 200 heating resistance wire and coiled into a single layer helix 10 cm in diameter. As shown in Figure 4.2 A, the miniaturization of the GC column in this system was achieved through a fan-less design. A conventional GC system uses forced air convection heat transfer with a fan to reduce the column temperature gradient; however, for the miniaturized system, uniform temperature was achieved by placing a highly thermally conductive material (stainless steel foil) alongside the column coil, which increased heat transfer efficiency. Infrared thermal imaging in Figure 4.3 shows uniform temperature distribution with a maximal temperature difference of only 3 °C in the column coil. The column temperature programmable control was achieved by a pulse-width-modulated trigger (100 Hz, 5 V square wave) to MOSFET via USB-6003 OEM digital output and the column temperature was monitored by a thermocouple embedded in the column coil. The single point temperature measurement via thermocouple accurately reports

the column temperature and is used with an accurate temperature feedback control to help maintain stable analyte retention time.

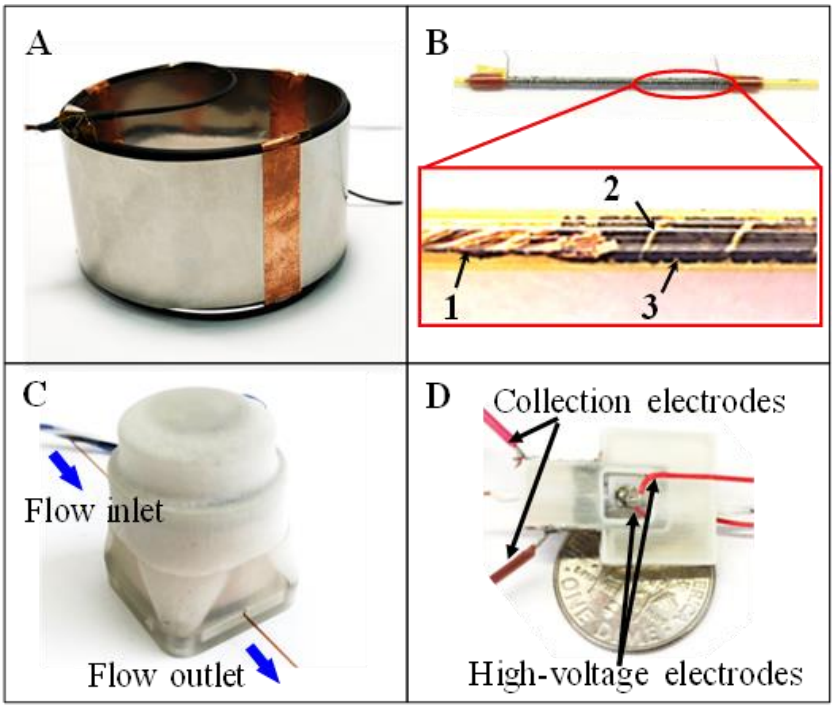

Figure 4.2 (A) Picture of an Rtx®-VMS 5 m long GC column coil packaged in stainless steel foil. (B) Picture of a preconcentrator. The enlarged portion shows the (1) sealing wire, (2) internal helix copper wire, and (3) adsorption material (Carbopack™ B beads) (C) Picture of a µPID packaged in a 3D printed case with a section of guard column (250 µm i.d.) connected on each side. (D) Assembled µHDBD-PID with signal collection and high-voltage electrodes.

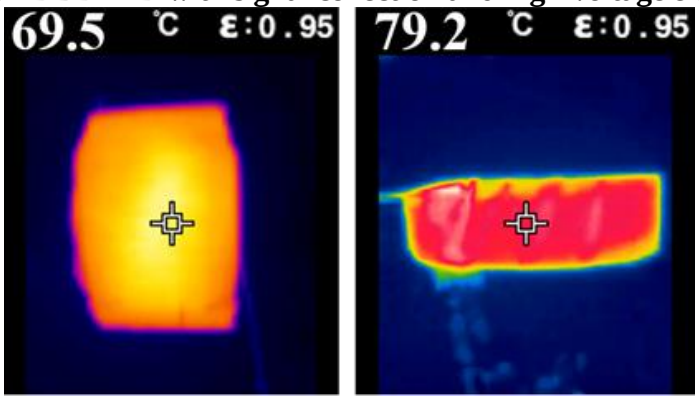

Figure 4.3 Infrared thermal image of the (A) heated first–dimensional column and (B) heated second–dimensional column taken with a FLIR TG165 infrared camera. The observed temperature difference on the column coil edge was not physically real, as shown by multi-point inspection with a thermocouple; this be caused by infrared reflection from wrinkles on the column coil surface.

4.3.3 Preconcentrator and thermal injector

The preconcentrator and thermal injector were used to trap/concentrate VOCs at room temperature with adsorption materials then quickly inject the trapped VOCs into the GC column. The preconcentrator consisted of a deactivated fused silica tube (0.53 mm i.d. and 0.69 mm o.d.) filled with three segments of absorption materials (Carbopack™ B, Carbopack™ X, and Carboxen® 1000 with a weight of 1 mg each) sealed with a segment of copper wire on each end (see Figure 4.2 B). A Nichrome 80 wire with a resistance of 18 Ω was wrapped tightly around the outer wall of the tube. In order to enhance thermal conductivity in the section containing adsorption materials, a 2 cm long helix of copper wire was inserted into the tube. The thermal injector was designed similarly, with the only difference being that only 1 mg of Carboxen® 1000 was used as the adsorption material (used for trapping highly volatile compounds such as formaldehyde). The preconcentrator and thermal injector were preconditioned at 300 °C for 12 hours under helium flow prior to use. During operation 24 VDC was applied to the heating wire for 0.5 seconds to rapidly heat the preconcentrator/thermal injector to 300 °C for rapid injection. Subsequently, a 10% pulse-width-modulated 24 VDC was applied to maintain the temperature at 300 °C for 7.5 seconds in order to completely desorb VOCs. Owing to the low thermal mass design, the total energy consumption of each injection was estimated to be 40 J, which is negligible when compared with the system's overall energy consumption (25 W X 500 s = 12.5 kJ).

4.3.4 Detectors

A flow-through μPID (shown in Figure 4.2 C) was adapted from our previously reported version[15]. The dimensions of the microfluidic channel were increased to 380 μm x 400 μm x 2.5 cm. Due to the wider channel width, the baseline signal was reduced. Because of the nondestructive nature of the μPID, analytes eluted from the first-dimensional column can be detected by the μPID while still

being flowed through to the next dimension. The μPID used in this study provides sensitive detection (tens of picograms) of VOCs with photoionization potentials under 10.6 eV.

The μHDBD-PID (shown in Figure 4.2 D) installed in the second-dimensional column was adapted from our previously reported version[16] and used to detect formaldehyde (photoionization potential: 10.88 eV). The current version decreased the discharge electrode gap to 580 μm, lowering the plasma inducing voltage and power consumption. A home-made high-voltage, high-frequency converter [16] with a 1 V DC input and 1.2 kV @ 7.7 kHz output was used to drive the helium plasma. The power consumption was estimated to be 90 mW. Signals from both μPID and μHDBD-PID were acquired by a USB 6003 OEM analog input channel with a 10 Hz digital low pass filter. Further details of the μHDBD-PID can be found in the Supplementary Information.

4.3.5 μHDBD-PID design and fabrication

A sandwich structure (glass/silicon/glass) was employed to build the helium plasma chamber, fluidic channel, and ionization channel. The fabrication process is described in Figure 4.4. 380-μm thick silicon was anodically bonded to 100-μm thick glass (Figure 4.4 A), followed by deep reactive-ion etching through the silicon wafer to create the features shown in Figure 4.4 B. Finally, a 100-nm thick platinum electrode for high-voltage barrier discharge induction was deposited on the outer surface of the glass wafer on each side after a second glass/silicon-glass anodic bonding. A schematic of the μHDBD-PID is shown in Figure 4.4 E. Since the gas flow insulation design included four venting ports and a shielding wall, isolation between the plasma chamber and analyte inlet channel was improved (Figure 4.5 B). Thus, the auxiliary helium flow lowered while still avoiding contamination by flow from the ionization channel. In addition, the shielding wall reduced the baseline signal and prevented signal overload caused by electric arcs in the plasma chamber. A flow resistor (Figure 4.7 A) was applied maintain an auxiliary flow rate of 5 mL/min for all experiments.

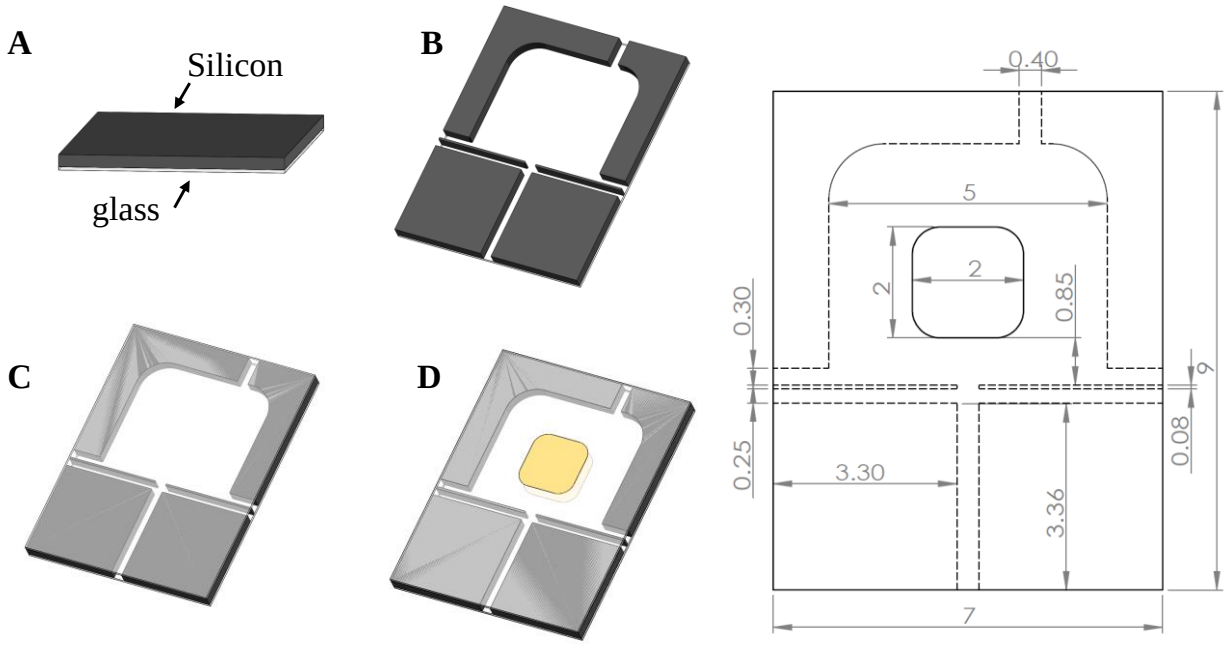

Figure 4.4 µHDBD-PID fabrication procedure (A) Anodically bonded glass and silicon. (B) Plasma chamber, fluidic channel, and ionization channel created by deep reactive-ion etching. (C) Another layer of glass anodically bonded to silicon. (D) Illustration of µHDBD-PID after high-voltage barrier discharge electrode deposition. (E) µHDBD-PID schematic with all units in mm.

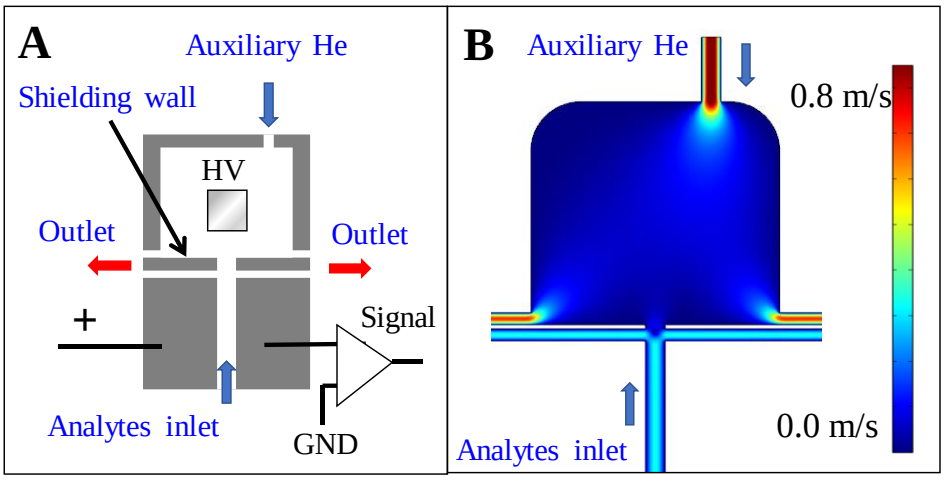

Figure 4.5 (A) µHDBD-PID electric and fluidic connections (B) Fluidic simulation using COMSOL Multiphysics® with a flow rate of 2 mL/min and 5 mL/min at the analyte inlet and auxiliary He inlet, respectively.

4.3.6 Micro-Deans switch

The micro-Deans switch serves as a gas flow router that operates through use of auxiliary gas. By switching the auxiliary gas inlet (using a miniaturized three-port valve), the first-dimensional flow can be directed to one of the outlets (see Figure 4.6 A). The flow channel of the micro-Deans switch was similar in size (150 µm wide and 380 µm deep) to a GC column; thus, the micro-Deans switch dead volume was negligible. Additionally, a buffer line connected to both auxiliary gas inlets further reduced the dead volume in those regions. In order to properly control flow routing, the auxiliary gas pressure was required to be equal to or greater than the inlet pressure (Figure 4.6 B). Flow limiting/balance was achieved by using flow resistors (Figure 4.7 A). Compared to an electric pressure controller, the flow resistor was lower cost, lower energy consumption, more robust, and smaller.

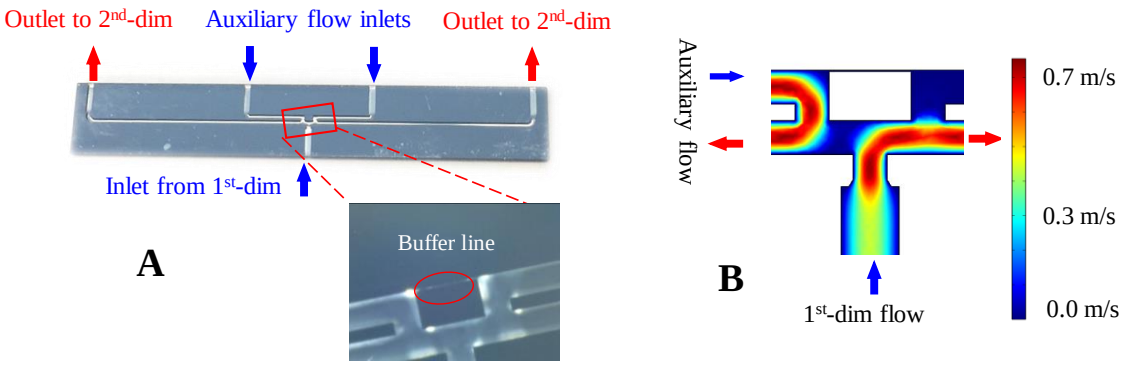

Figure 4.6 (A) Picture of the micro-Deans switch and (enlarged) buffer line area. (B) Fluidic simulation for the enlarged area in (A) using COMSOL Multiphysics®. Equal pressures were applied on the auxiliary inlet and the first-dimensional inlet. The auxiliary flow and first-dimensional flow are directed to the left and right outlet, respectively, without interference between the two.

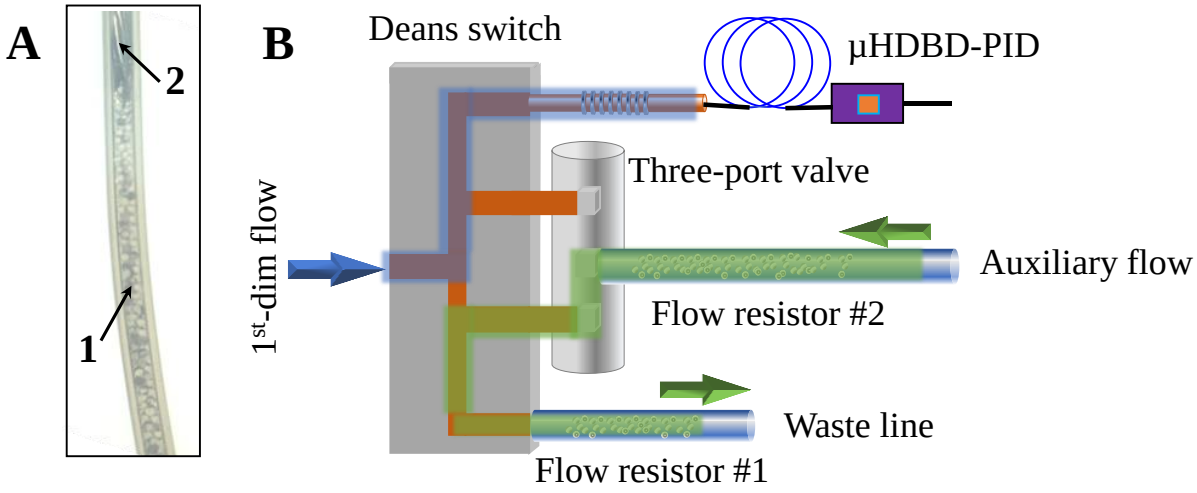

Figure 4.7 (A) Flow resistor made from polytetrafluoroethylene tube (1/32 inch o.d., 0.48 mm i.d.) filled with glass beads (1) and sealed by a metal wire (2). (B) Fluidic schematic of the micro-Deans switch. Flow resistor #1 provided the same flow resistance as the second–dimensional fluidic resistance (including the thermal injector, second–dimensional column, and μHDBD-PID) and was installed on the waste line for flow balance. Flow resistor #2 provided the same flow resistance as the first–dimensional fluidic resistance and was installed upstream of the three-port valve that controlled the auxiliary flow of the micro-Deans switch.

4.3.7 GC operation

Vapor was collected by the preconcentrator through a 20-cm long tube at a sampling flow rate of 40 mL/min. The flow was provided by a vacuum pump during sampling. The sampling time was adjustable and usually was a few minutes. After sampling, the flow was switched to carrier gas and run for 30 s for stabilization. Then, the preconcentrator was heated to inject the analytes into the first-dimensional column, which was preheated to 23 °C and initially connected to the waste line. The heart-cutting window was applied from 34 s to 50 s by the micro-Deans switch to send formaldehyde (along with other vapors within the window) to the thermal injector for the second-dimensional column. The thermal injector was heated to inject the samples into the second-dimensional column, which was maintained isothermally at 80 °C. Eluates from the second-dimensional column were detected by the μHDBD-PID. Simultaneously, other analytes were continuously separated by the first-dimensional

column and detected by the μPID. Flow rates for the first- and second-dimensional column were kept at 2 mL/min. Details of gas flow layouts at sampling, first-dimensional separation, target cutting, and first- and second-dimensional separation can be found in Figure 4.8.

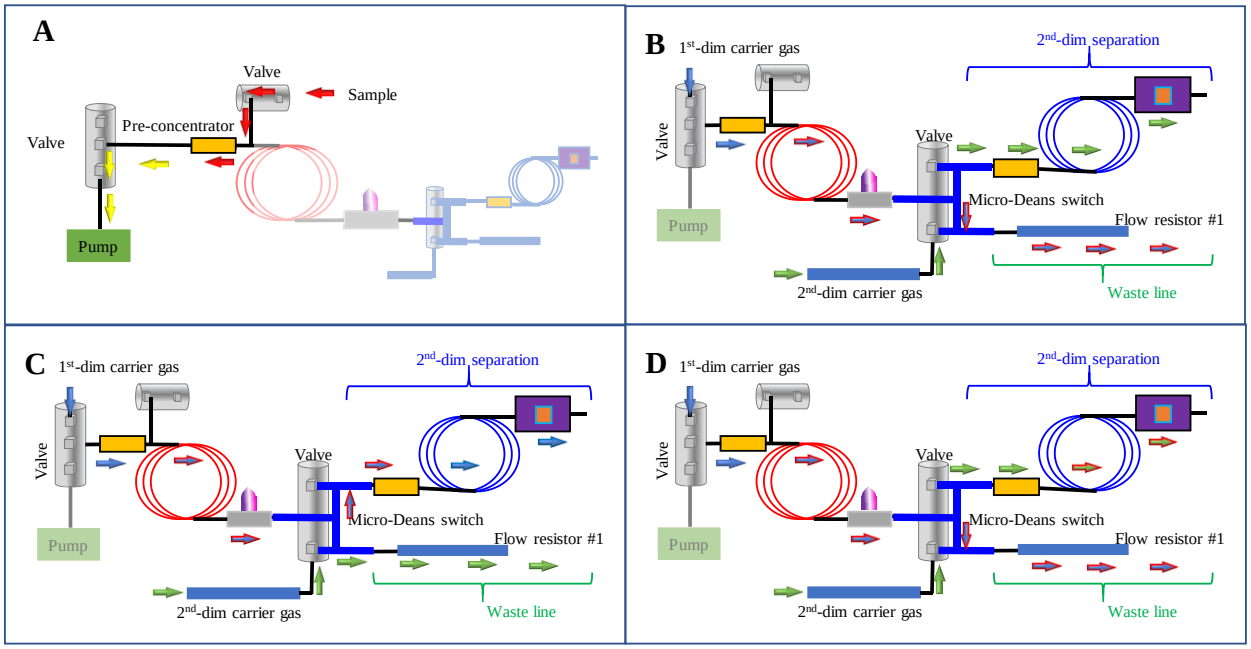

Figure 4.8 Gas flow layouts at (A) sampling, (B) 1-D separation, (C) target cutting, and (D) first- and second-dimensional separation.

4.3.8 Sample preparation

Various concentrations of formaldehyde vapor were generated by corresponding aqueous solutions. The vapor-liquid equilibrium is calculated by Equation 4.3.8.1[17]

$$[HCHO(aq)] = 10^{\left[\left(\frac{4538}{T}\right)-11.34\right]}[HCHO(g)]^{\left[\left(\frac{252.2}{T}\right)+0.2088\right]} \quad (4.3.8.1)$$

where $[HCHO(aq)]$ (M) is the formaldehyde molar concentration in water, T(K) is temperature (294 K), and $[HCHO(g)]$ (atm) is the formaldehyde vapor pressure. Based on purge efficiency theory reported by Zhou et al.[18], the formaldehyde purge efficiency is almost zero due to the high Henry's constant (4415 mol L^{-1} atm^{-1}, which is converted from 32 mol m^{-3} Pa^{-1} at 298.15 K with a temperature dependent constant of 6800 K)[19]. Therefore, we assume that the vapor-liquid equilibrium is maintained

during experimentation. Table 4.2 lists formaldehyde concentrations tested as benchmarks for our system. The sample purge setup is shown in Figure 4.9. A 20-mL sample vial filled with 10 mL of sample solution was sealed with a metal cap containing a polytetrafluoroethylene septum. Purified air was flowed into the vial at a flow rate of 40 mL/min. The relative humidity at the outlet was measured to be 63%~65% at 23 °C by a Dewpoint sensor (see Figure 4.10). Vapors were collected from vial headspaces and trapped by the preconcentrator.

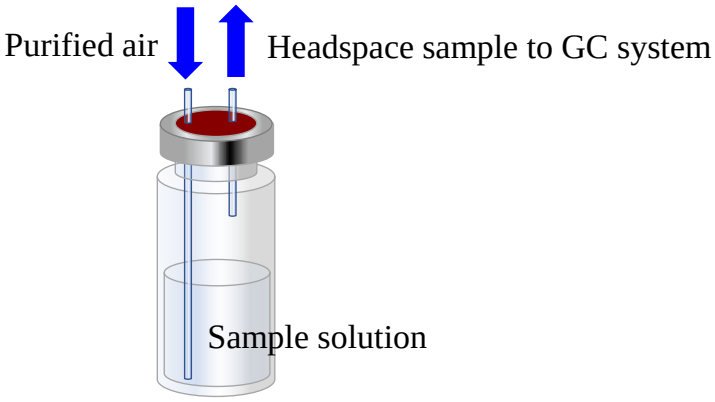

Figure 4.9 VOC vapor generation setup that consisted of a 20-mL vial filled with 10 mL of sample solution. The cap contained an inlet and an outlet for purified purging air and GC sampling, respectively.

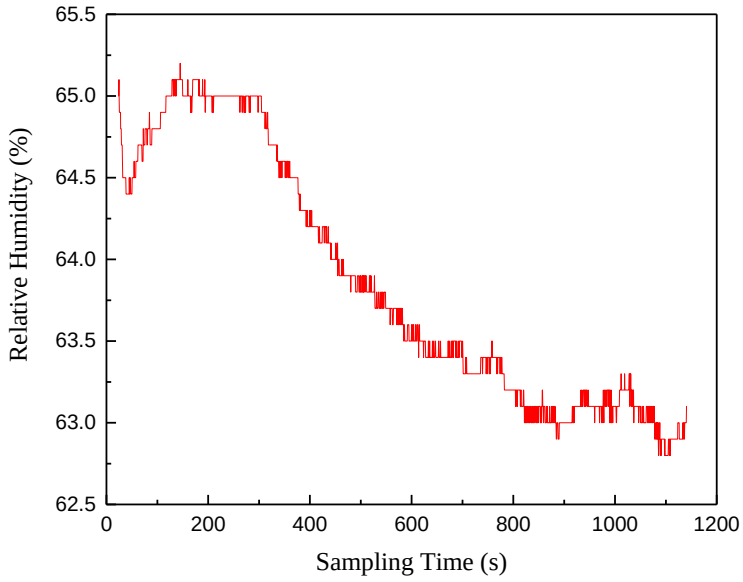

Figure 4.10 Relative humidity level measured via Dewpoint sensor at the sample outlet of the purge-and-trap setup at 23 °C.

4.4 Results and discussion

4.4.1 Formaldehyde retention time

Figure 4.11 A shows an example second-dimensional chromatogram cut from the window of 34 s to 50 s from the first-dimensional separation. The formaldehyde retention time (defined as peak position) is 141.1 s with a FWHM of 27.3 s. Formaldehyde retention statistics obtained from 15 measurements at various concentrations are summarized as a box plot in Figure 4.11 B. The average retention time is found to be 141.1 s with the standard deviation of only 0.2 s. The low retention time variation is due to the stable flow rate and accurate temperature control in our device. The total assay time is less than 11 minutes, including <6 minutes of sampling, <1 minute for first-dimensional separation and <4 minutes for second-dimensional separation.

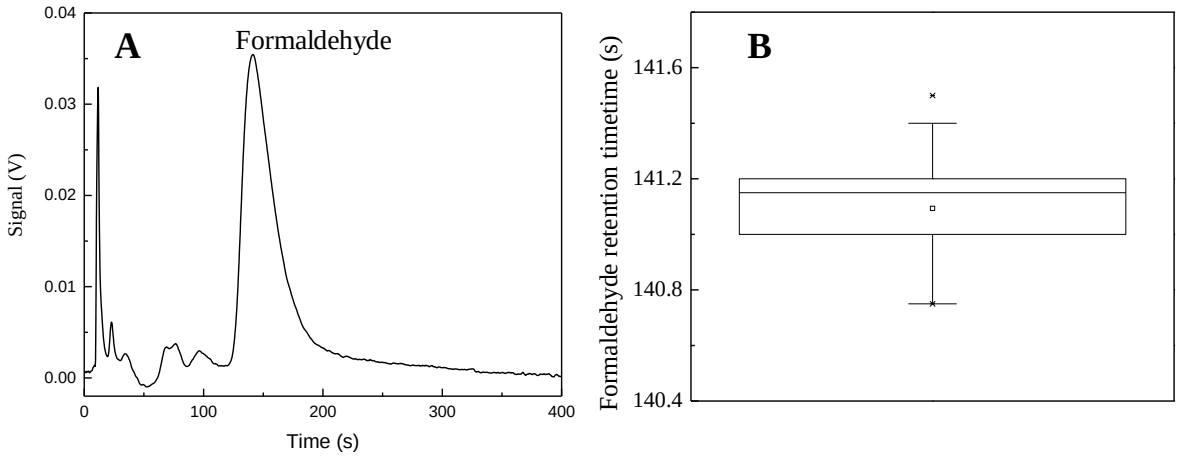

Figure 4.11 (A) Second-dimensional chromatogram cut from the window of 34 s to 50 s in the first-dimension. The formaldehyde (31.5 ppb) peak is located at 141.3 s with a FWHM of 27.9 s. (B) Box plot of 15 measurements (3 measurements of vapor volume concentrations at 0.5 ppb, 2 ppb, 8 ppb, 31.5 ppb, and 100 ppb) of formaldehyde retention time in second–dimensional separation with a maximum value of 141.5 s, minimum value of 140.75 s, and mean value at 141.1 s.

4.4.2 Sampling time dependency

As discussed above, the liquid-vapor equilibrium is assumed to be maintained during the sampling process. To verify this, we detected 2 ppb (V/V) formaldehyde with varying sampling times as 1 min, 2 min, 4 min, 6 min, and 8 min. Formaldehyde peak area (integrated from the second-dimensional chromatogram) versus sampling time is plotted in Figure 4.12, showing high linearity. Therefore, the purging setup in Figure 4.8 provides a constant formaldehyde vapor concentration source.

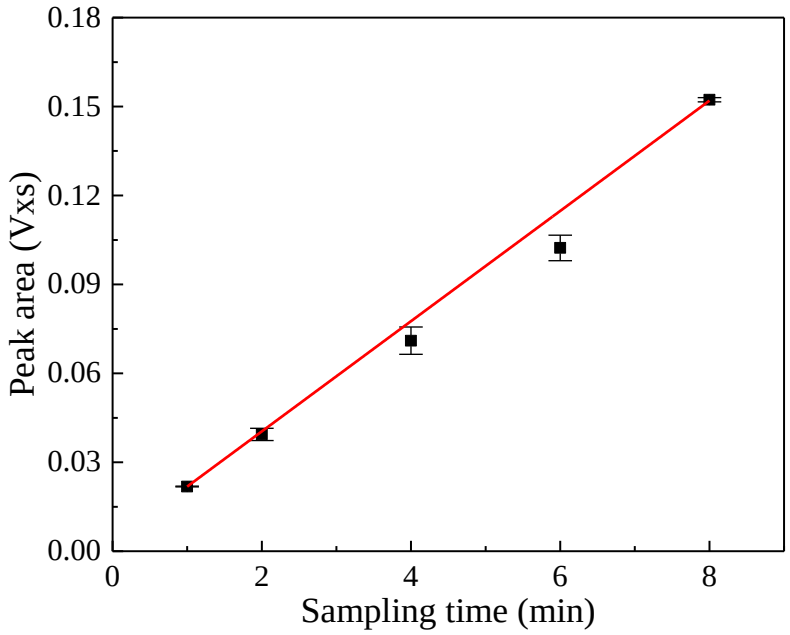

Figure 4.12 Formaldehyde peak area (from the second-dimensional chromatogram) as a function of different sampling times for 2 ppb (V/V) formaldehyde at a sample flow rate of 40 mL/min. The solid line is a linear fit with a slope of 0.01859, intercept of 0.00322, and R^2 value of 0.99958. The error bars for each data point were obtained from 3 measurements.

4.4.3 Linearity and sensitivity

Linearity and sensitivity characterization of formaldehyde detection was carried out using the concentrations listed in Table 4.2 under conditions described in Methods. Formaldehyde peak areas were obtained by integrating signals from the second-dimensional chromatogram. Error bars were calculated from the standard deviation of formaldehyde peak area in 3 repeated tests. A highly linear response to vapor volume concentration ranging from 0.5 ppb to 100 ppb was obtained as shown in

Figure 4.13. The low detection limit (LOD) for 6 minutes of sampling was calculated to be 0.23 ppb (V/V) from Equation 4.4.3.1.

$$LOD = \frac{3\sigma}{S} \tag{4.4.3.1}$$

where S (2.2 mV/ppb) is sensitivity (at 0.5 ppb V/V) and σ (0.169 mV) is the standard deviation of the baseline noise. Given that the lowest regulated formaldehyde vapor concentration is 2 ppb (V/V) (see Table 4.1), our device satisfactorily meets current formaldehyde detection requirements.

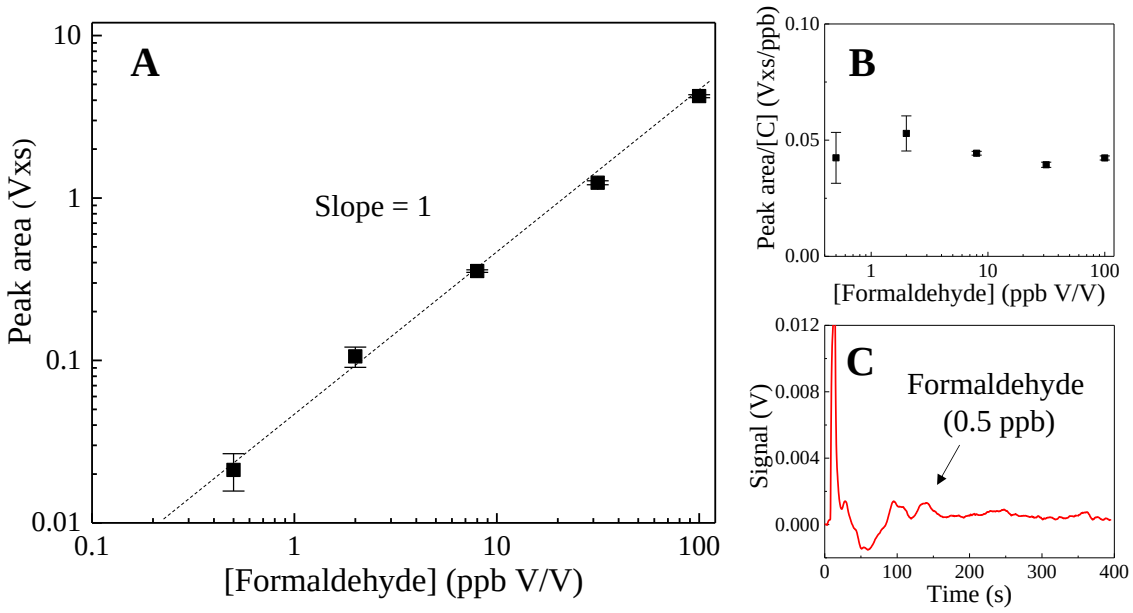

Figure 4.13 Formaldehyde detection linearity and sensitivity. (A) Peak area as a function of formaldehyde concentration using a log-log scale. The dashed line is linear with a slope of unity. (B) Peak areas normalized to corresponding concentrations versus formaldehyde concentration. (C) Representative second-dimensional chromatogram for a formaldehyde concentration of 0.5 ppb. In all measurements, the sampling time was 6 minutes. Error bars for each data point were obtained from 3 measurements.

Table 4.2 Vapor volume concentrations and corresponding solution concentrations of formaldehyde.

Vapor concentration ppb (V/V)	Solution concentration (μmol/L)
0.5	1.671
2	7.323
8	32.10
31.5	138.6
100	474.0

4.4.4 Simultaneous analysis of formaldehyde and other VOCs

In practice, such as in indoor air analysis, other VOCs should be analyzed along with formaldehyde. Here, we demonstrate simultaneous, rapid analysis of formaldehyde and BTEX (benzene, toluene, ethylbenzene, and p-xylene). Formaldehyde was separated by the first- and second-dimensional columns and detected by a μHDBD-PID, whereas BTEX was separated by temperature-ramping the first-dimensional column and detected by a μPID. A sample solution containing formaldehyde (32.1 μmol/L), benzene (0.064 μmol/L), toluene (0.083 μmol/L), ethylbenzene (0.094 μmol/L), and p-xylene (0.094 μmol/L) was prepared. The flow rate was 40 mL/min and the sampling time was 6 minutes. From previously published experimental results[18], the purge efficiency for BTEX was approximately 80 %. Thus, the equivalent vapor volume concentrations of formaldehyde and BTEX were 8 ppb, 51 ppb, 70 ppb, 75 ppb, and 75 ppb, respectively. A representative chromatogram is presented in Figure 4.14. The first-dimensional column temperature was initially maintained at 23 °C for 100 s, then heated to 53 °C at a rate of 4.5 °C/min. Separation and detection of formaldehyde in the second-dimensional column were performed in parallel with BTEX separation and detection in the first-dimensional column. Total analysis time was 14 min and can be further reduced by applying a more rapid temperature ramping profile.

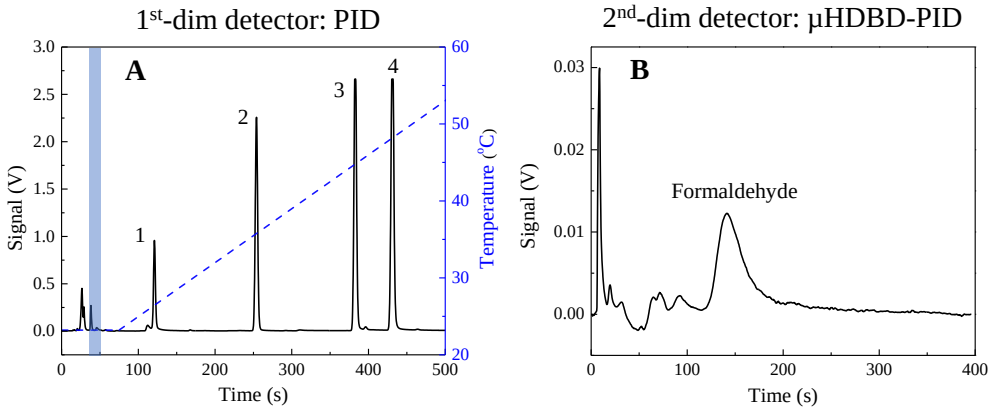

Figure 4.14 (A) First-dimensional separation signals for formaldehyde and BTEX (1: benzene; 2: toluene; 3: ethylbenzene, 4: p-xylene). The formaldehyde heart-cutting window is given by the

shaded area. The dashed blue line indicates the temperature ramping profile (T = 23 °C for 100 s then to 53 °C at a rate of 4.5 °C/min). (B) Second-dimensional chromatogram of VOCs cut out from first-dimension. The second-dimensional column was maintained isothermally at 80 °C. The flow rate for both columns was kept at 2 mL/min.

4.5 Conclusion

In this chapter, we present the development and characterization of a portable 2-D GC device based on heart-cutting technology for sensitive, rapid, and on-site formaldehyde detection. Miniaturization of GC components resulted in compact size and light weight. Experimental results of elution time, sampling time dependence, linearity, and sensitivity show that our portable 2-D GC system can carry out accurate and repeatable formaldehyde detection with a detection limit (at 3σ) of 0.23 ppb (V/V) with only 6 minutes of sampling time. Integration of open tubular columns (for the first-dimension) and porous PLOT columns (for the second-dimension) provides an effective solution for high volatility compound separation: heart-cutting from the first-dimensional separation alleviates potential contamination to the PLOT column by other VOCs with lower volatilities. In addition to formaldehyde, other common VOCs such as BTEX can be detected rapidly and simultaneously with the first dimension. We envision that this fully automated GC device will have a broad range of applications in continuous monitoring of air pollution and other toxic, volatile materials.

4.6 References

1. Brown, S. K.; Sim, M. R.; Abramson, M. J.; Gray, C. N., Concentrations of Volatile Organic Compounds in Indoor Air – A Review. *Indoor Air* **1994,** *4* (2), 123-134.
2. Blondel, A.; Plaisance, H., Screening of formaldehyde indoor sources and quantification of their emission using a passive sampler. *Building and Environment* **2011,** *46* (6), 1284-1291.
3. Gupta, K. C.; Ulsamer, A. G.; Preuss, P. W., Formaldehyde in indoor air: Sources and toxicity. *Environment International* **1982,** *8* (1), 349-358.
4. Squire, R. A.; Cameron, L. L., An analysis of potential carcinogenic risk from formaldehyde. *Regulatory Toxicology and Pharmacology* **1984,** *4* (2), 107-129.
5. Chung, P.-R.; Tzeng, C.-T.; Ke, M.-T.; Lee, C.-Y., Formaldehyde gas sensors: a review. *Sensors* **2013,** *13* (4), 4468-4484.
6. Beasley, R. K.; Hoffmann, C. E.; Rueppel, M. L.; Worley, J. W., Sampling of formaldehyde in air with coated solid sorbent and determination by high performance liquid chromatography. *Analytical Chemistry* **1980,** *52* (7), 1110-1114.
7. Sugaya, N.; Nakagawa, T.; Sakurai, K.; Morita, M.; Onodera, S., Analysis of aldehydes in water by head space-GC/MS. *Journal of health science* **2001,** *47* (1), 21-27.
8. del Barrio, M.-A.; Hu, J.; Zhou, P.; Cauchon, N., Simultaneous determination of formic acid and formaldehyde in pharmaceutical excipients using headspace GC/MS. *Journal of Pharmaceutical and Biomedical Analysis* **2006,** *41* (3), 738-743.
9. Belman, S., The fluorimetric determination of formaldehyde. *Analytica Chimica Acta* **1963,** *29*, 120-126.
10. Güntner, A. T.; Koren, V.; Chikkadi, K.; Righettoni, M.; Pratsinis, S. E., E-Nose Sensing of Low-ppb Formaldehyde in Gas Mixtures at High Relative Humidity for Breath Screening of Lung Cancer? *ACS Sensors* **2016,** *1* (5), 528-535.
11. Wang, X.; Si, Y.; Wang, J.; Ding, B.; Yu, J.; Al-Deyab, S. S., A facile and highly sensitive colorimetric sensor for the detection of formaldehyde based on electro-spinning/netting nano-fiber/nets. *Sensors and Actuators B: Chemical* **2012,** *163* (1), 186-193.
12. Yang, X.; Wang, Y.; Liu, W.; Zhang, Y.; Zheng, F.; Wang, S.; Zhang, D.; Wang, J., A portable system for on-site quantification of formaldehyde in air based on G-quadruplex halves coupled with A smartphone reader. *Biosensors and Bioelectronics* **2016,** *75*, 48-54.
13. Toda, K.; Tokunaga, W.; Gushiken, Y.; Hirota, K.; Nose, T.; Suda, D.; Nagai, J.; Ohira, S.-I., Mobile monitoring along a street canyon and stationary forest air monitoring of formaldehyde by means of a micro-gas analysis system. *Journal of Environmental Monitoring* **2012,** *14* (5), 1462-1472.
14. Suzuki, Y.; Nakano, N.; Suzuki, K., Portable Sick House Syndrome Gas Monitoring System Based on Novel Colorimetric Reagents for the Highly Selective and Sensitive Detection of Formaldehyde. *Environmental Science & Technology* **2003,** *37* (24), 5695-5700.
15. Zhu, H.; Nidetz, R.; Zhou, M.; Lee, J.; Buggaveeti, S.; Kurabayashi, K.; Fan, X., Flow-through microfluidic photoionization detectors for rapid and highly sensitive vapor detection. *Lab on a Chip* **2015,** *15* (14), 3021-3029.
16. Zhu, H.; Zhou, M.; Lee, J.; Nidetz, R.; Kurabayashi, K.; Fan, X., Low-Power Miniaturized Helium Dielectric Barrier Discharge Photoionization Detectors for Highly Sensitive Vapor Detection. *Analytical Chemistry* **2016,** *88* (17), 8780-8786.
17. Dong, S.; Dasgupta, P. K., Solubility of gaseous formaldehyde in liquid water and generation of trace standard gaseous formaldehyde. *Environmental Science & Technology* **1986,** *20* (6), 637-640.
18. Zhou, M.; Lee, J.; Zhu, H.; Nidetz, R.; Kurabayashi, K.; Fan, X., A fully automated portable gas chromatography system for sensitive and rapid quantification of volatile organic compounds in water. *RSC Advances* **2016,** *6* (55), 49416-49424.
19. Sander, R., Compilation of Henry's law constants (version 4.0) for water as solvent. *Atmospheric Chemistry & Physics* **2015,** *15* (8).

Chapter 5 Micro-Gas Chromatography Peak Focusing Based on Stationary Phase Thickness Gradient

The content in Chapter 5 has been adapted from the following manuscript which will be submitted in the future: Hongbo Zhu, Jinyan She, Maxwell Wei-Hao Li, Ziqi Li, Katsuo Kurabayashi, and Xudong Fan

5.1 Introduction

Micro-gas chromatography (μGC) devices have advantages over traditional benchtop GC systems in portability and rapid analysis for real-time field applications. Microcolumns, which are usually microfabricated on silicon wafers, are one of the key components in μGC. Compared to regular, circular-shaped columns, the separation capability of microcolumns is currently limited by many factors such as sharp turns and pooling of the stationary phase in anisotropic channel corners. Optimization of the fluidic channel layout[1-5], column chip material[1, 5-12], channel configuration[13-16], and stationary phase[14, 17-21] has led to significantly improved microcolumn performance in recent years.

Negative temperature gradient separation (NTGS) is another method for improving column performance[22-26]. NTGS has been implemented in regular GC columns[27] and microfabricated columns[16, 28] to sharpen elution peaks. NTGS works by partially heating the inlet end of a column and generating a temperature gradient via thermal exchange with the ambient environment. Since the temperature is lower towards the column outlet, the front part of a peak travels more slowly than its tail, effectively focusing the peak. However, NTGS has a number of drawbacks. First, since NTGS relies on thermal exchange with the ambient environment to create the temperature gradient, any variation in ambient temperature, humidity, air convection rate, and thermal

conductivity of the packing material, causes fluctuations in the peak position and width, thus making the separation considerably less repeatable and predictable. Although a sophisticated heat control module can be used to stabilize the temperature gradient, it adds additional size, weight, complexity, and cost to the GC device. Second, for the separation of low volatility compounds, when the inlet (hot) end reaches the upper limit of the operating temperature (usually defined by the thermal decomposition temperature of the stationary phase material and the maximal allowable temperature of the connection interface), the temperature at the outlet (cold) end may still be relatively low for those compounds. Consequently, the entire applicable temperature range is not fully utilized. Third, separation of high volatility compounds usually is performed at a temperature very close to the ambient temperature, meaning that the temperature gradient and hence NTGS are virtually non-existent. Fourth, NTGS results in energy loss due to thermal exchange, which can be challenging for microsystems with limited energy resources.

In this chapter, we proposed and demonstrated another method for peak focusing by creating a stationary phase thickness gradient along a column, as illustrated in Figure 5.1 A. Based on the GC theory (discussed later in detail), a positive film thickness gradient can generate the same peak focusing effect as a negative temperature gradient. However, in contrast to NTGS, the film thickness gradient is fixed once the stationary phase coating process is complete. It does not require thermal exchange with the ambient environment and the focusing effect is present for both low and high volatility compounds. In this work, a 10 m long film thickness gradient column (FTGC) was microfabricated and subsequently coated with the stationary phase using dynamic coating. The film thickness increased from ~140 nm at the inlet to ~190 nm at the outlet, thus generating a positive thickness gradient. The FTGC exhibited a focusing effect for high volatility compounds with room temperature isothermal separation as well as for low volatility compounds

(such as C_{40} and C_{44}) separated using temperature ramping to 350 °C. A focusing rate of up to 35% was observed.

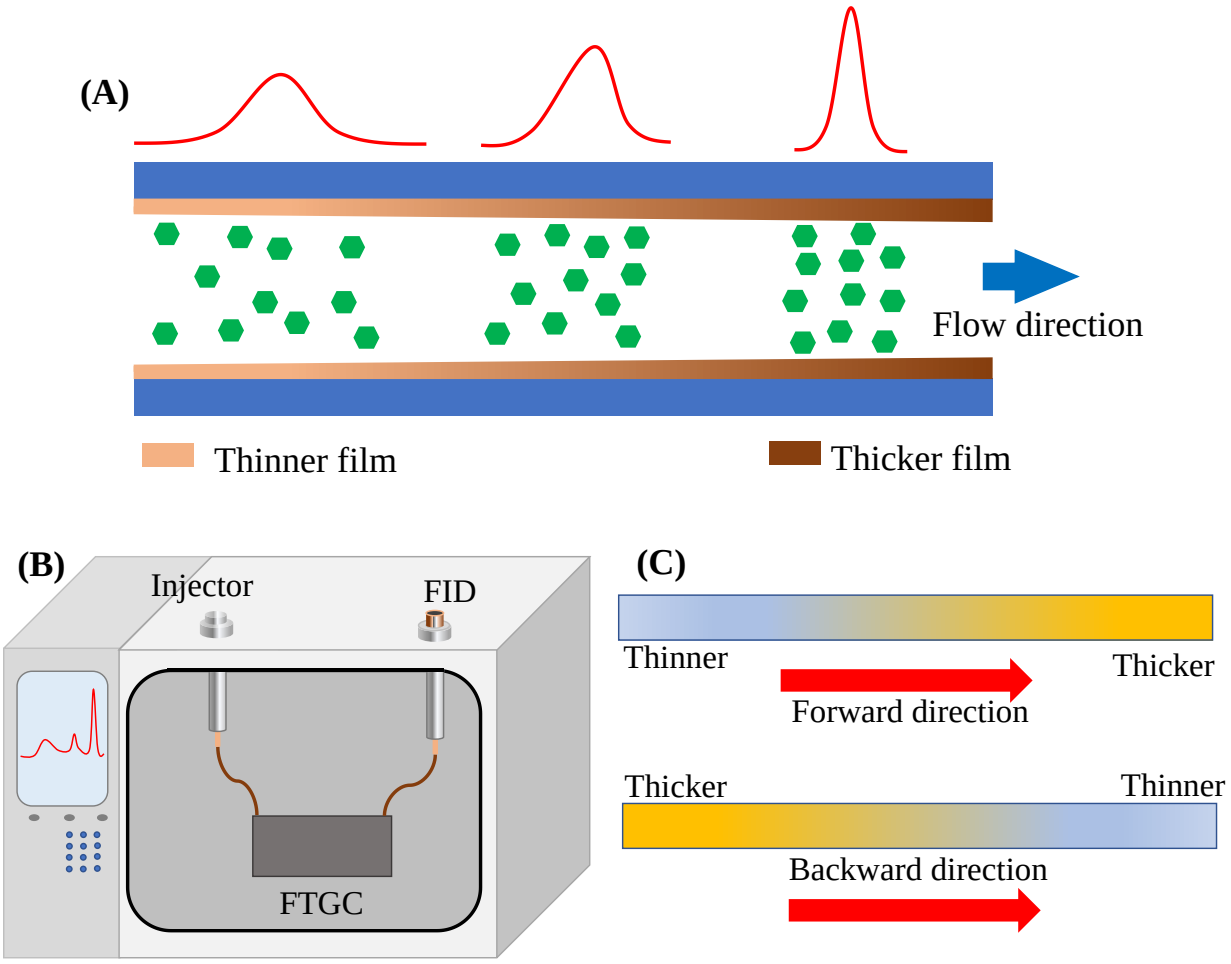

Figure 5.1 (A) Illustration of the peak focusing effect in an FTGC. (B) Setup for microcolumn performance evaluation. (C) Schematic of forward and backward modes.

5.2 Peak focusing principle

The velocity of an analyte at a location x (x being the distance from the column inlet), $V(x)$, is determined by

$$V(x) = \mu(x) \times u, \tag{5.2.1}$$

where $\mu(x)$ is the mobile phase fraction of an analyte at location x and u is the carrier gas velocity. $\mu(x)$ is given by

$$\mu(x) = 1 - \frac{a^{stat}(x,h)}{a}, \tag{5.2.2}$$

where a is the total amount of analyte and $a^{stat}(x,h)$ is the amount of analyte in the stationary phase at location x, which is linearly proportional to the stationary phase thickness, h, at location x. In a column that has a positive coating thickness gradient (i.e., the coating thickness increases with increased x), the front end of the analyte peak (or zone) travels more slowly than its tail end based on Equation 5.2.2. Consequently, the analyte peak is focused, and the peak height is increased compared to a column with a uniform coating (see Figure 5.1 A for illustration).

In fact, increasing the local stationary phase thickness at location *x* is equivalent to decreasing the temperature at the same location, which can be understood through the equation governing the local retention factor, $k(x)$[29]

$$k(x) = Ae^{\frac{G}{RT}} \times h, \tag{5.2.3}$$

where G is Gibbs free energy, R is the Boltzmann constant, T is temperature, and A is a constant. $k(x)$ is related to $\mu(x)$ by $\mu(x) = 1/(1 + k(x))$. From Equation 5.2.3 we further obtain

$$\frac{\Delta \mathrm{k}}{k} = -\frac{G}{RT}\frac{\Delta T}{T} + \frac{\Delta h}{h} = -g\frac{\Delta T}{T} + \frac{\Delta h}{h}, \tag{5.2.4}$$

where $g = \frac{G}{RT} = -\frac{\Delta S}{R} + \frac{\Delta H}{RT}$ is the dimensionless Gibbs free energy, which can be calculated from an analyte's entropy (ΔS) and enthalpy (ΔH). The entropy and enthalpy for three example alkanes and one particular stationary phase are listed in Table 5.1[30]. It can be seen from Equation 5.2.4 that a positive thickness gradient along the column has the same focusing effect as a negative temperature gradient. Both gradients can create a velocity difference (or retention factor difference) between the inlet and outlet (or the front and the tail of a peak). Their equivalency is expressed in the following equation

$$-g\frac{\Delta T}{T} = \frac{\Delta h}{h}. \tag{5.2.5}$$

Table 5.1 Entropy (ΔS) and enthalpy (ΔH) of evaporation of three representative n-alkanes from a (5%-phenyl)-dimethyl polysiloxane film. The values are adopted from Ref. [30].

	C_{10}	C_{12}	C_{14}
ΔS (*kJ/mol/K*)	74.3	76.8	79.3
ΔH (*kJ/mol*)	47	51.6	56.2

Figure 5.2 plots the relationship between the film thickness gradient and temperature gradient for analyte C_{10} and a particular stationary phase based on Equation 5.2.5. For the 10 m long FTGC in the present study, the film thickness was approximately 140 nm and 190 nm at the inlet and the outlet, respectively, corresponding to a fractional thickness change of 36%. Figure 5.3 shows the equivalent temperature gradient for analytes C_{10}, C_{12}, and C_{14} at various temperatures.

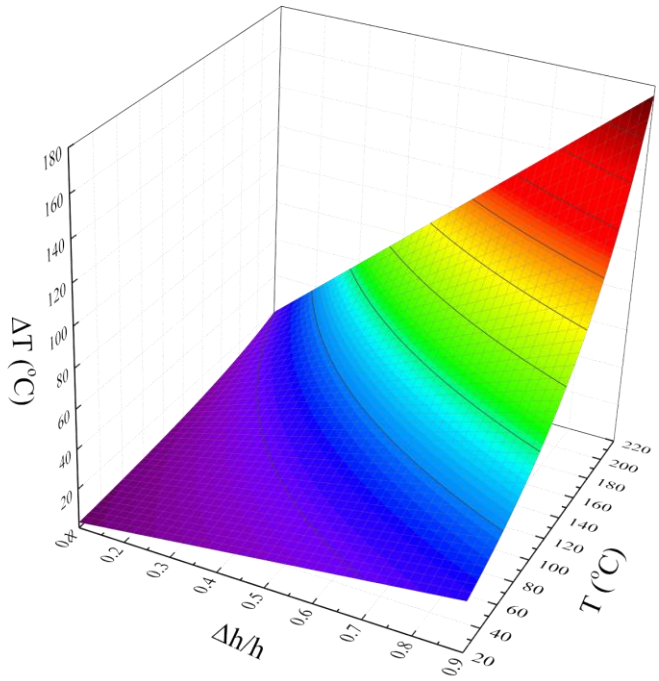

Figure 5.2 Equivalent column temperature gradient (ΔT) calculated using Eq. (5) and the Gibbs energy parameters listed in Table S1 for C_{10} under isothermal separation for various fractional film thicknesses and column temperatures.

The film thickness gradient has a number of advantages over temperature gradient based peak focusing. First, the column film thickness gradient is independent of the column temperature.

Therefore, the peak focusing effect exists regardless of the column temperature and is generally applicable to analytes of any volatilities, significantly broadening the column operating temperature range. For low volatility compounds, the entire column can be heated to the maximal allowable temperature. For high volatility compounds, the focusing effect persists even during room temperature isothermal separation, which could not be achieved using NTGS. Second, in contrast to the temperature gradient, which depends on heater and ambient conditions (such as heater arrangement, heat dissipation, column size/weight, column channel arrangement, and ambient temperature and air flow), the film thickness gradient is independent of ambient conditions, which makes GC operation more reliable and repeatable and less susceptible to environmental changes. Third, since no thermal exchange is required for the FTGC, the column can be packaged in thermal insulation materials to reduce heat dissipation and save energy, which is important for applications requiring low energy consumption. Finally, the FTGC can be operated in the same way as a regular column (or microcolumn) with no extra accessories (such as heater or cooler), which significantly reduces the device complexity for future integration.

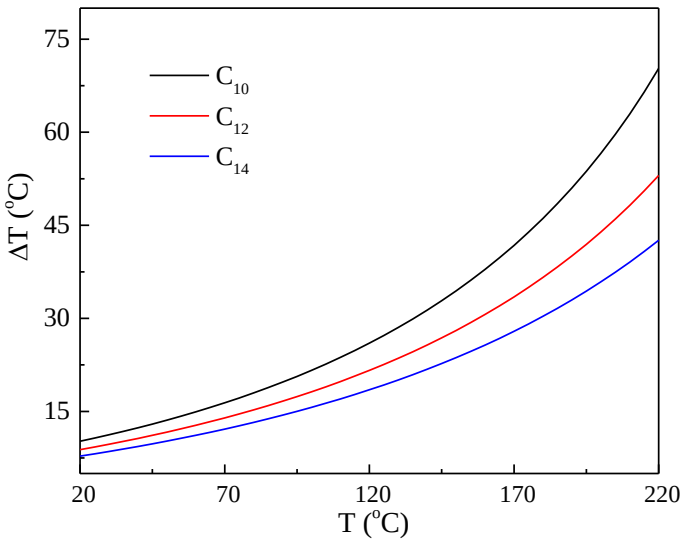

Figure 5.3 Equivalent column temperature gradient for C_{10}, C_{12}, and C_{14} using Eq. (5) and the Gibbs energy parameters listed in Table S1 for various column temperatures for a 36% film thickness gradient.

5.3 Experimental

5.3.1 Materials

Analytical standard grade C_5 to C_{15} and standard mixture ASTM D2887-12 (P/N 31674) were purchased from Sigma-Aldrich (St. Louis, MO) and Restek (Bellefonte, PA), respectively. Coating solvent (dichloromethane) and stationary phase materials (vinyl modified OV-1, P/N 6001; OV-17, P/N 6017) were bought from Ohio Valley Specialty Company (Marietta, OH). Dow SYLGARD™ 184 reagent B (crosslinker) and Hysol® 1C™ Epoxy were purchased from Ellsworth Adhesive (Germantown, WI). Polyimide sealing resin (P/N 23817) for the connection interface was purchased from Sigma-Aldrich (St. Louis, MO). PEEK tubing 1/32" OD x .015" ID (P/N 1568) was purchased from IDEX Health & Science (Forrest, IL). Rxi®5Sil MS (P/N 13620) with 250 µm inner diameter and 0.25 µm film thickness was purchased from Restek. All materials were used as purchased without further purification or modification.

5.3.2 Microcolumn fabrication

The microcolumn fabrication process is shown in Figure 5.4. The column pattern was created on the top side of a double side polished wafer with standard lithography processes (Figure 5.4 A). Deep reactive ion etching created a 390 µm deep trench on the inlet and outlet areas (Figure 5.4 B). Due to the lower etching rate on small patterns, the depth of the column area was found to be 350 to 360 µm. After stripping off the photoresist, anodic bonding with Boroflat 33 glass was performed at 350 °C under vacuum (Figure 5.4 C). The heater was then deposited on the back side of the column through physical vapor deposition and patterned with the lift-off method (Figure 5.4 D). Photos of a 10 m long microcolumn on the glass side (front) and the heater side (back) are shown in Figures 5.4 E and F, respectively.

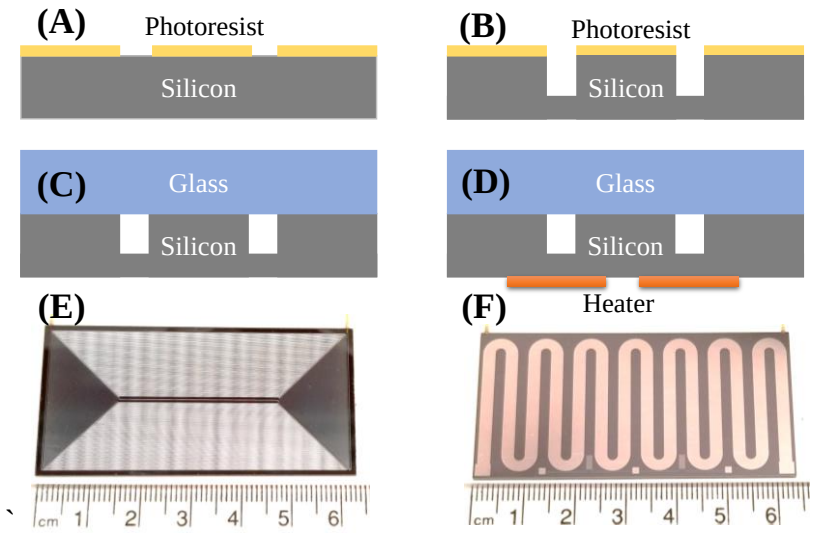

Figure 5.4 (A-D) Microcolumn fabrication processes. (E) and (F) Photos of the front and back side of a 10 m long microcolumn.

5.3.3 Microcolumn coating

A solute composed of OV-1 (75% w/w), OV-17 (10% w/w), and crosslinker (15% w/w) was dissolved in dichloromethane to create a 2% (w/w) coating solution. A salinization reaction was performed before coating by injecting hexamethyldisilazane (HMDS) vapor into the column multiple times from a benchtop GC. As illustrated in Figure 5.5, an 18 µL coating solution was loaded into a 10 m long column (cross-section 133 µm x 360 µm) from the column inlet via a syringe pump, which created an approximately 0.39 m long coating solution plug inside the column. A 5-psi positive pressure was applied from the inlet to drive the coating solution towards the outlet. A negative 2-psi vacuum pressure was applied to the outlet of the column through a dummy column with the same cross-sectional dimensions using a vacuum pump. The dummy column was used to maintain a constant coating plug speed when the coating solution traveled along the microcolumn. The small volume (18 µL) of low boiling point dichloromethane ensured that the coating solution concentration and hence the film thickness on the column wall increased

progressively when the coating solution plug moved from the inlet to the outlet of the microcolumn due to the rapid evaporation of the solvent under vacuum[31]. After coating, dry air was continuously flowed through the column to completely remove the solvent. The column was then crosslinked at 80 °C for 2 hours followed by post deactivation using HMDS. An aging process was performed in a GC oven under a helium flow of 1 mL/min at 200 °C for 2 hours with a temperature ramping rate of 5 °C/min from room temperature. The temperature was then ramped to 300 °C for an additional 2 hours at the same temperature ramping rate.

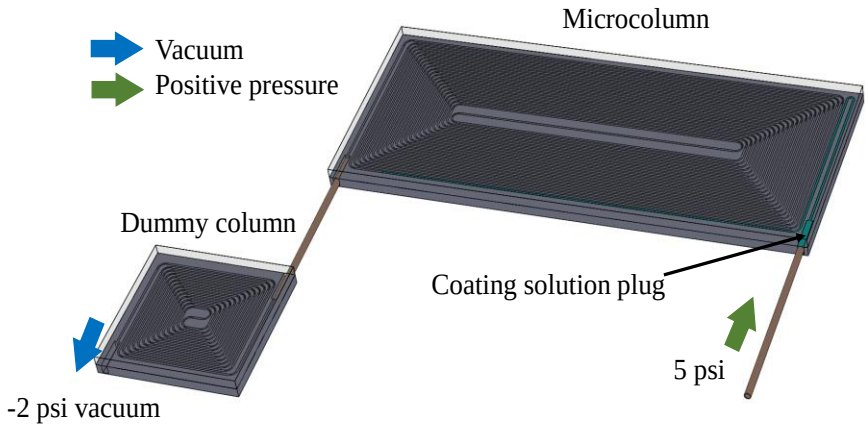

Figure 5.5 FTGC coating setup.

5.3.4 Connection interface design

Fluidic connections between microcolumns and other components is an important factor that affects μGC integration and performance. The connection interfaces are required to be leak-free, low in dead-volume, and capable of withstanding high temperatures. Fused silica capillaries are commonly used for fluidic connections due to the simple connection process and being compact in size as compared to other methods such as Nanoport™ assemblies[32], O-ring brazing[33], and heater/clamp assemblies[16]. Adhesives such as Hysol® epoxy[34-35], polyimide[36], and Duraseal[13, 37-39] are used to secure the connection interface between the capillary and the microcolumn chip,

but these suffer from low operating temperature[28], leakage after thermal cycling[16], and outgassing. For example, our own experiments have showed that while Hysol® epoxy has sufficient mechanical strength to withstand the shear force induced by thermal expansion mismatch between the adhesive and the column after thermal cycling of up to 350 °C, strong outgassing makes Hysol® epoxy unsuitable for high temperature operation beyond 200 °C (see Figure 5.6). Polyimide is a thermally stable and outgassing-free material commonly used for GC column outer surface coating. However, due to the poor adhesion between polyimide and silicon, leakage occurs after thermal cycling, which is exacerbated when the microcolumn is under high head pressure.

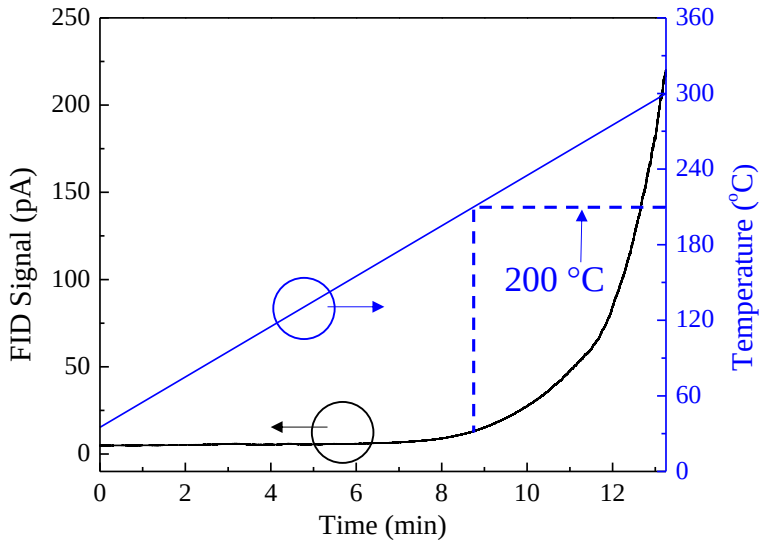

Figure 5.6 Hysol® 1C™ Epoxy thermal stability tested using GC/FID. Epoxy particles were loaded in a fused silica tube (0.58 mm ID), which was connected to a guard column between the GC injector and FID. The temperature was ramped from 35 °C to 300 °C at 20 °C/min. The onset temperature for FID signal distortion was 200 °C.

In this chapter, we developed a two-step gluing method using both polyimide and Hysol® epoxy at the connection interface of the capillary and column chip (see Figure 5.7). During the first step, polyimide was applied to the connection interface, which serves as an "O-ring" to

prevent chemicals released from Hysol® epoxy from entering the microcolumn. To avoid potential clogging of the microfluidic channel, the polyimide was pre-cured at 70 °C for 1 min to increase its viscosity. After polyimide application, the microcolumn was heated at 230 °C in an oven overnight to further cure the polyimide. During the second step, Hysol® epoxy was applied to the outer surface of the connection interface to robustly glue the polyimide, capillary, and microcolumn chip together. Finally, as an option, a polyether ether ketone (PEEK) tube was used to fix the epoxy and provided additional support to the capillary. The epoxy was initially cured at room temperature for 1 hour and then baked at 60 °C for 2 hours. This connector could withstand 350 °C for at least a few hundred thermal cycles without failure.

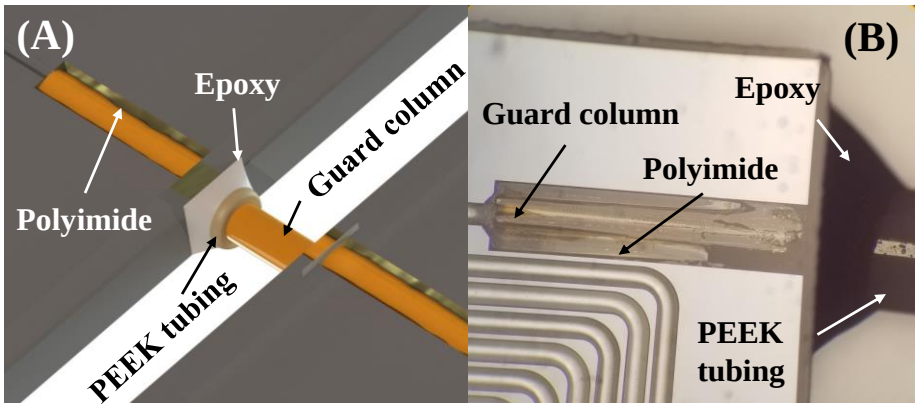

Figure 5.7 (A) Illustration of hybrid adhesive connection ports. (B) Photo of the connection port.

5.3.5 Testing setup

The FTGC performance evaluation setup is shown in Figure 5.1 B. The FTGC was installed in a benchtop GC (Agilent 6890) equipped with a flame ionization detector (FID). Helium was used as the carrier gas. Evaluation of the peak focusing effect was performed when the analytes were injected from the thinner coating end (forward mode) or the thicker coating end (backward mode), as illustrated in Figure 5.1 C.

5.4 Results and discussion

5.4.1 Characterization of the microcolumn stationary phase

The thickness of the stationary phase was characterized by using scanning electron microscopy (SEM) close to the inlet (thinner film side) and outlet (thicker film side) of the microcolumn. The column was cut in liquid nitrogen in order to change the stationary film to glass state, thus generating a clear film cross-section. The film morphology was fixed by lyophilization. Figure 5.8 shows that the film thickness changes from 142 nm to 188 nm from inlet to outlet.

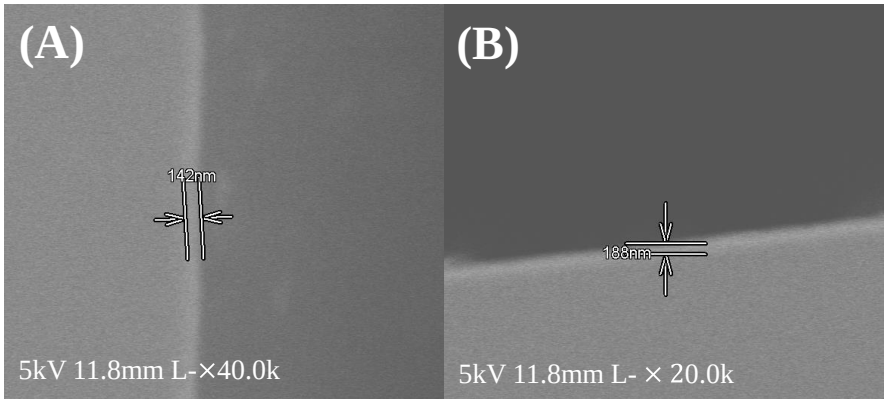

Figure 5.8 (A) SEM image close to the column inlet with a film thickness of 142 nm. (B) SEM image close to the column outlet with a film thickness of 188 nm.

5.4.2 Peak focusing

Separation of an alkane mixture was carried out to evaluate the peak focusing effect provided by the FTGC. The mixture was prepared with equal parts of C_8 to C_{15}. A volume of 0.1 µL mixture liquid at a split ratio of 100:1 was used for injection. Figure 5.9 shows the chromatograms when the FTGC was used in both forward and backward modes, where the temperature started from 30 °C and was ramped to 180 °C at 15 °C /min. Analyte peaks in the forward mode are clearly consistently sharper than those in backward mode. As shown in Table 5.2, the focusing rate ranges from 10% to 30% (or 5-15% when compared with the uniform

coating), which is similar to or better than the focusing rate achieved using NTGS (up to 10%) with a temperature gradient of up to 45 ^{o}C[27].

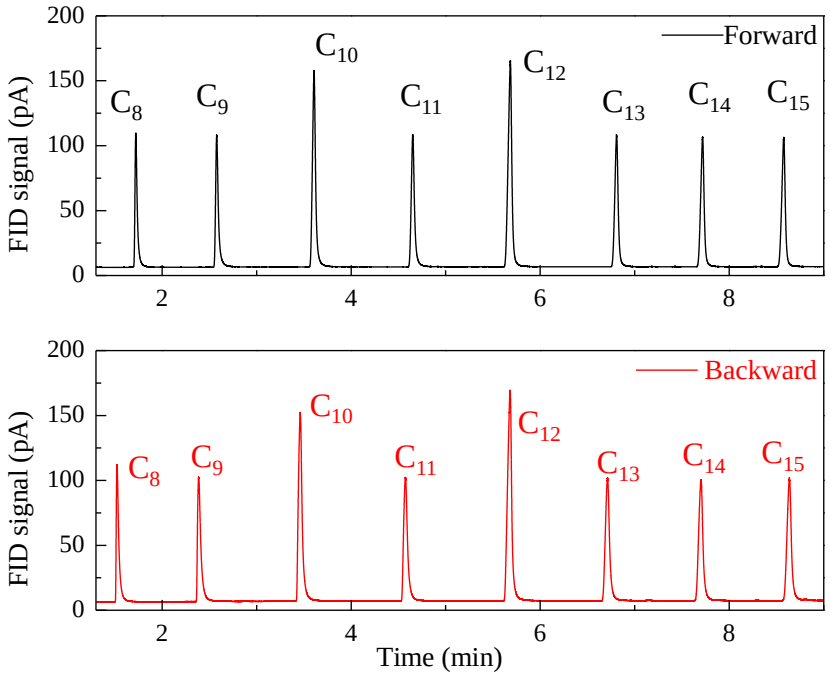

Figure 5.9 Separation of C_8 to C_{15} using a 10 m long FTGC in forward and backward modes. Sample injection volume was 0.1 µL at a split ratio of 100:1. The column temperature for both modes began at 30 °C and was ramped to 180 °C at 15 °C /min. The carrier gas flow rate was 1.2 mL/min. A zoom-in of the chromatograms in both forward and backward modes is provided in Figure 5.10. The full-width-at-half-maximum (FWHM) of each peak is given in Table 5.2.

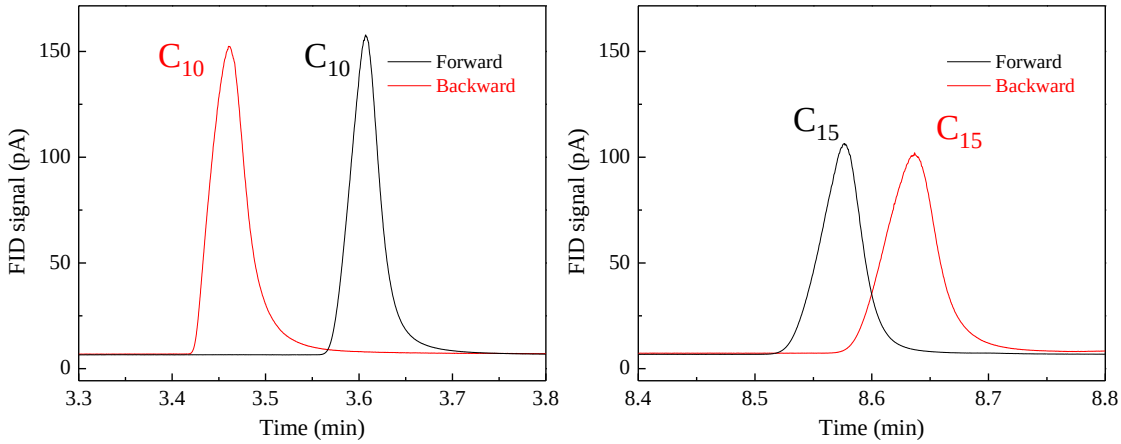

Figure 5.10 Zoom-in of chromatograms in Figure 5.9 for C_{10} and C_{15} in forward and backward modes.

Table 5.2 Full-widths-at-half-maximum (FWHMs) for all peaks in Figure 5 (both forward and backward chromatograms).

	C_8	C_9	C_{10}	C_{11}	C_{12}	C_{13}	C_{14}	C_{15}
Forward (min)	0.0237	0.0284	0.0342	0.0345	0.0414	0.0372	0.0382	0.0387
Backward (min)	0.0264	0.0354	0.0419	0.0446	0.0475	0.0462	0.0489	0.0489
Difference (min)	0.0027	0.0070	0.0077	0.0101	0.0061	0.0090	0.0107	0.0102
% change	11.4%	24.6%	22.5%	29.3%	14.7%	24.2%	28%	26.4%

Note that the separation conditions of the same analyte is not identical in forward and backward modes. In the forward mode, the analyte is first exposed to thinner film at low temperature before reaching thicker film at high temperature, which is opposite to the backward mode in which the analyte is first exposed to thicker film at low temperature, then thinner film at high temperature. As a result, the retention times for analytes in these two modes differs slightly, by a few seconds.

5.4.3 Temperature ramping dependent focusing

To elucidate how the temperature ramping rate affects the peak focusing, Figure 5.11 shows separation of the same C_8 to C_{15} mixture with three different ramping rates (5, 15, and 25 25 °C/min). At a higher temperature ramping rate, the analyte spends less time in the stationary phase. Consequently, the focusing effect becomes less significant and the difference in analyte peak widths between forward and backward modes becomes smaller, as shown in Figure 5.11 A. On the other hand, the increased temperature ramping rate sharpens all peaks. Therefore, the focusing rate (i.e., the peak width difference divided by the peak width) for each peak is still high, ranging from 5% to 35%.

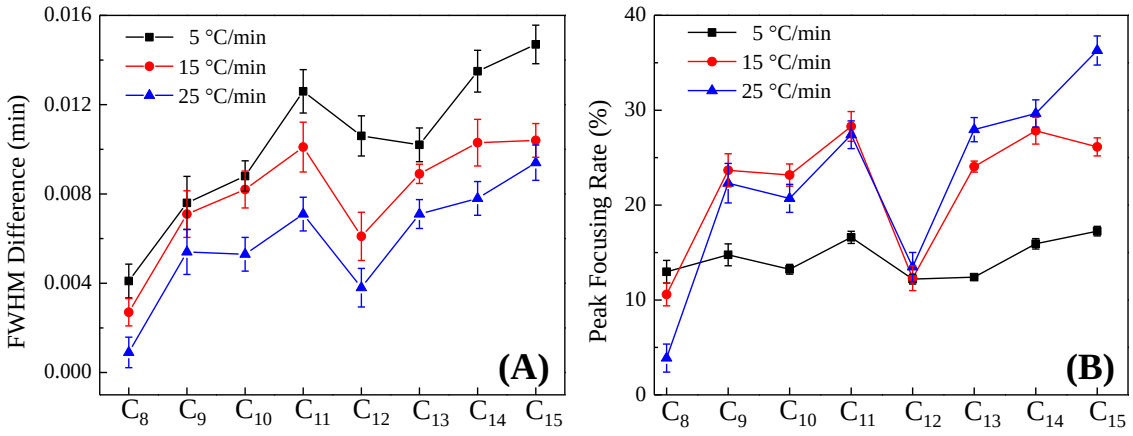

Figure 5.11 (A) Full-width-at-half-maximum (FWHM) differences of peaks generated from C_8 to C_{15} mixture separation at different temperature ramping rates. (B) Peak focusing rates for C_8 to C_{15}. Peak focusing rate is calculated by dividing FWHM differences by the corresponding peak's FWHM in the forward mode. Error bars are obtained from three measurements in both forward and backward modes.

5.4.4 Focusing for high volatility compounds

As discussed previously, the FTGC should be able to focus peaks even at low column temperatures typically used for high volatility compound separation (which was difficult to achieve using NTGS). Figure 5.12 shows isothermal separation of C_5 and C_6 (1:1 V/V) at 26 °C with a flow rate of 1.2 mL/min in both forward and backward modes. The FWHMs of C_5 and C_6 are 21.5% and 10.3% sharper, respectively, in the forward mode compared to in the backward mode. Note that for NTGS it is difficult to achieve the peak focusing effect for high volatility compounds.

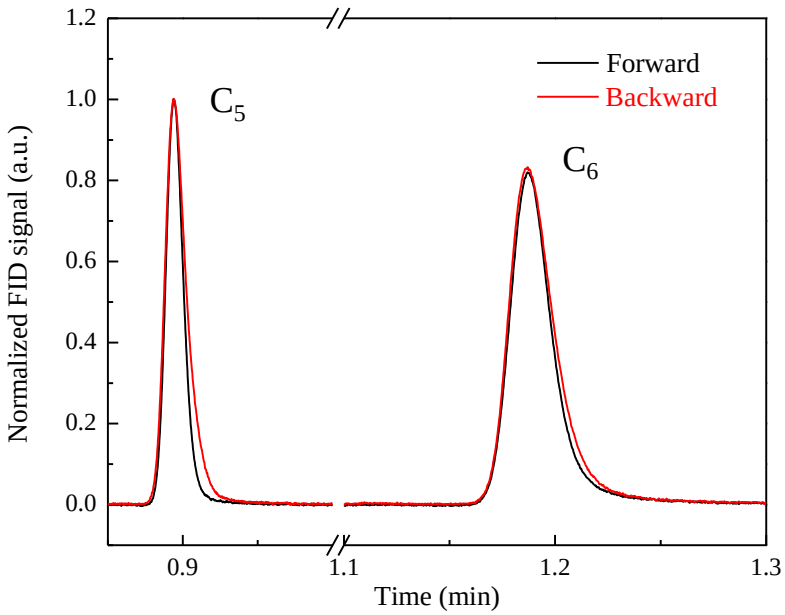

Figure 5.12 Isothermal separation of C_5 and C_6 at a temperature of 26 °C and a flow rate of 1.2 mL/min. Peak height is normalized to that of C_5. The peak width (FWHM) is 0.01293 min and 0.01557 min for C_5 and 0.02128 min and 0.02294 min for C_6 for the forward and backward mode, respectively.

5.4.5 Analysis of ASTM D2887-12 standard

In order to evaluate the FTGC's high temperature separation performance, we used the ASTM D2887 standard mixture as a model system, which contains C_5 to C_{44}. Tetratetracontane (C_{44}) has a Kovats index of approximately 4400 and requires a column temperature of 350 °C. High temperature operation requires high thermal stability for the connection interface (no leakage at the interface and low outgassing of the adhesive into the microcolumn) and the stationary phase (low stationary phase bleeding), which can be achieved in our microcolumn using the methods described in the Experimental section.

Figures 5.13 A and B show the separation of ASTM D2887 using a 10 m long FTGC that was operated in the forward mode. All peaks are well separated. In comparison with the same FTGC but operated in the backward mode, the significant focusing effect can be clearly seen. In particular, for the two compounds, C_{40} and C_{44}, which have the lowest volatility and require a

separation temperature of 350 ºC, the corresponding peak width is 0.03997 min and 0.0599 min in the forward mode and 0.05447 min and 0.08096 min in the backward mode (see Figure 5.14), about 35% peak width reduction for both compounds.

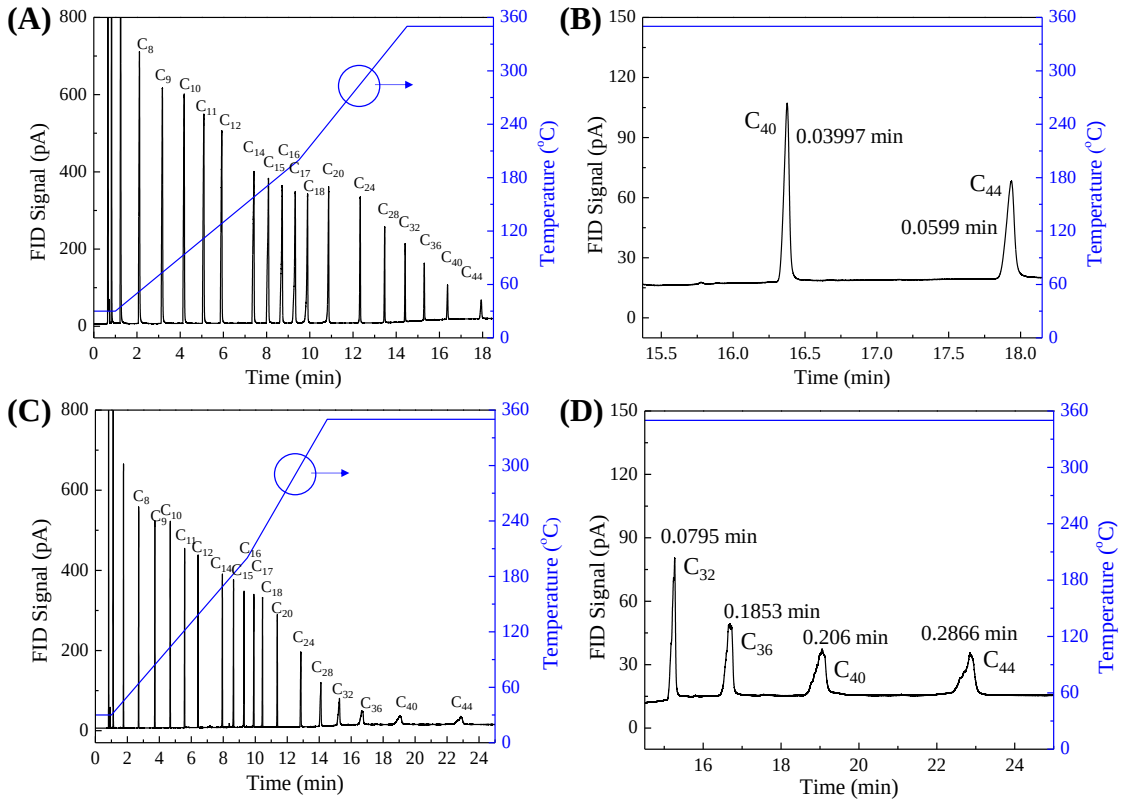

Figure 5.13 (A) Chromatogram of an *n*-alkane standard mixture (ASTM D2887) using a 10 m long FTGC without baseline subtraction. (B) Enlarged chromatogram in (A) for C_{40} and C_{44} peaks with each corresponding peak width (FWHM). The baseline drifted from 6.4 pA (30 °C) to 20.2 pA (350 °C). (C) Chromatogram of an *n*-alkane standard mixture (ASTM D2887) using a 15 m long Rxi®5Sil MS commercial column without baseline subtraction. (D) Enlarged chromatogram in (C) for C_{32} to C_{44} peaks with each corresponding peak width (FWHM). The baseline drifted from 6.3 pA (30 °C) to 15.5 pA (350 °C). In both (A) and (C), the temperature was set at 320 °C and 350 °C for injector and FID, respectively. 0.4 µL of mixture liquid was injected with a split ratio of 15:1. The oven temperature was set at 30 °C for 1 min and then ramped to 200 °C at a rate of 20 °C/min. A higher ramping rate of 30 °C/min was then used to heat the oven to 350 °C. The volumetric flow rate was 1.3 mL/min and the linear flow speed was 46.5 cm/s for both columns.

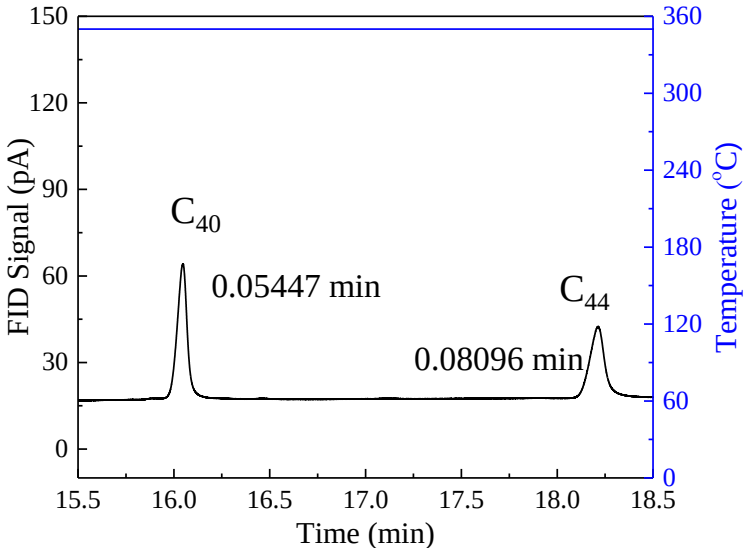

Figure 5.14 Zoom-in of chromatogram of ASTM D2887 for the 10 m long FTGC in Figure 5.13 was operated in the backward mode. All other conditions are the same as in Figure 5.13.

We further compare the FTGC with the commercial column that has a similar coating material. Figures 5.13 C and D show the separation of ASTM D2887 under the same experimental condition using a 15 m long Rxi®5Sil MS commercial column. Due to the different column lengths and film thicknesses, the retention time in these two chromatograms (Figures 5.13 A and C) may not be identical for the same analyte. Therefore, we compare the peak width of the analytes with similar retention times. From Figure 5.13 B, we can see that the retention time for C_{40} is 16.4 min, similar to C_{36} (16.7 min) in Figure 5.13 D. However, the peak width of C_{40} is 4.6 times sharper than that of C_{36}, demonstrating the excellent separation performance of the FTGC particularly for low volatility compounds. A baseline increase of only 13.8 pA from 30 °C to 350 °C was observed, comparable to the low bleed Rxi®5Sil MS column that had a baseline increase of 9.2 pA. Thus, the FTGC also demonstrated high thermal stability for the connection interface and the stationary phase.

5.5 Conclusion

We reported the development and evaluation of a film thickness gradient column that enables peak focusing. Theoretical analysis was performed to elucidate the working principle and systematic experiments were carried out to investigate the peak focusing effect under various conditions. A focusing rate of up to ~35% was achieved. Furthermore, we demonstrated separation of high volatility compounds isothermally at room temperature and low volatility compounds using temperature ramping up to 350 ^{o}C. As compared to the column based on the previously developed negative temperature gradient approach, the FTGC has advantages due to a larger applicable temperature range and compound volatility range, easier operation, better temperature control, less dependence on ambient conditions, greater compactness, and fewer accessories. Since the FTGC can be operated in the same manner as a regular column (or microcolumn), we expect that it will find broad applications in future GC devices.

5.6 References

1. Noh, H.-s.; Hesketh, P. J.; Frye-Mason, G. C., Parylene gas chromatographic column for rapid thermal cycling. *Journal of Microelectromechanical Systems* **2002,** *11* (6), 718-725.
2. Lambertus, G.; Elstro, A.; Sensenig, K.; Potkay, J.; Agah, M.; Scheuering, S.; Wise, K.; Dorman, F.; Sacks, R., Design, Fabrication, and Evaluation of Microfabricated Columns for Gas Chromatography. *Analytical Chemistry* **2004,** *76* (9), 2629-2637.
3. Sanchez, J.-B.; Berger, F.; Daniau, W.; Blind, P.; Fromm, M.; Nadal, M.-H., Development of a gas detection micro-device for hydrogen fluoride vapours. *Sensors and Actuators B: Chemical* **2006,** *113* (2), 1017-1024.
4. Yuan, H.; Du, X.; Tai, H.; Li, Y.; Zhao, X.; Guo, P.; Yang, X.; Su, Y.; Xiong, Z.; Xu, M., The effect of the channel curve on the performance of micromachined gas chromatography column. *Sensors and Actuators B: Chemical* **2017,** *239*, 304-310.
5. Bhushan, A.; Yemane, D.; Trudell, D.; Overton, E. B.; Goettert, J., Fabrication of micro-gas chromatograph columns for fast chromatography. *Microsystem Technologies* **2007,** *13* (3-4), 361-368.
6. Radadia, A.; Salehi-Khojin, A.; Masel, R.; Shannon, M., The fabrication of all-silicon micro gas chromatography columns using gold diffusion eutectic bonding. *Journal of Micromechanics and Microengineering* **2009,** *20* (1), 015002.
7. Reston, R. R.; Kolesar, E., Silicon-micromachined gas chromatography system used to separate and detect ammonia and nitrogen dioxide. I. Design, fabrication, and integration of the gas chromatography system. *Journal of Microelectromechanical Systems* **1994,** *3* (4), 134-146.
8. Lewis, A. C.; Hamilton, J. F.; Rhodes, C. N.; Halliday, J.; Bartle, K. D.; Homewood, P.; Grenfell, R. J.; Goody, B.; Harling, A. M.; Brewer, P., Microfabricated planar glass gas chromatography with photoionization detection. *Journal of Chromatography A* **2010,** *1217* (5), 768-774.
9. Qin, Y.; Gianchandani, Y. B., iGC2: an architecture for micro gas chromatographs utilizing integrated bi-directional pumps and multi-stage preconcentrators. *Journal of Micromechanics and Microengineering* **2014,** *24* (6), 065011.
10. Darko, E.; Thurbide, K. B.; Gerhardt, G. C.; Michienzi, J., Characterization of low-temperature cofired ceramic tiles as platforms for gas chromatographic separations. *Analytical Chemistry* **2013,** *85* (11), 5376-5381.
11. Raut, R. P.; Thurbide, K. B., Characterization of Titanium Tiles as Novel Platforms for Micro-Flame Ionization Detection in Miniature Gas Chromatography. *Chromatographia* **2017,** *80* (5), 805-812.
12. Malainou, A.; Vlachopoulou, M.; Triantafyllopoulou, R.; Tserepi, A.; Chatzandroulis, S., The fabrication of a microcolumn for gas separation using poly (dimethylsiloxane) as the structural and functional material. *Journal of Micromechanics and Microengineering* **2008,** *18* (10), 105007.
13. Gaddes, D.; Westland, J.; Dorman, F. L.; Tadigadapa, S., Improved micromachined column design and fluidic interconnects for programmed high-temperature gas chromatography separations. *Journal of Chromatography A* **2014,** *1349*, 96-104.
14. Zampolli, S.; Elmi, I.; Mancarella, F.; Betti, P.; Dalcanale, E.; Cardinali, G.; Severi, M., Real-time monitoring of sub-ppb concentrations of aromatic volatiles with a MEMS-enabled miniaturized gas-chromatograph. *Sensors and Actuators B: Chemical* **2009,** *141* (1), 322-328.

15. Radadia, A. D.; Morgan, R. D.; Masel, R. I.; Shannon, M. A., Partially buried microcolumns for micro gas analyzers. *Analytical Chemistry* **2009,** *81* (9), 3471-3477.
16. Ghosh, A.; Johnson, J. E.; Nuss, J. G.; Stark, B. A.; Hawkins, A. R.; Tolley, L. T.; Iverson, B. D.; Tolley, H. D.; Lee, M. L., Extending the upper temperature range of gas chromatography with all-silicon microchip columns using a heater/clamp assembly. *Journal of Chromatography A* **2017,** *1517*, 134-141.
17. Yamamoto, Y.; Akao, S.; Sakuma, M.; Kobari, K.; Noguchi, K.; Nakaso, N.; Tsuji, T.; Yamanaka, K., Development of Packed Column for Surface Acoustic Wave Gas Chromatograph Using Anodically Bonded Silicon–Glass Structure with a Compression Jacket. *Japanese Journal of Applied Physics* **2009,** *48* (7S), 07GG12.
18. Li, Y.; Zhang, R.; Wang, T.; Wang, Y.; Wang, Y.; Li, L.; Zhao, W.; Wang, X.; Luo, J., A micro gas chromatography with separation capability enhanced by polydimethylsiloxane stationary phase functionalized by carbon nanotubes and graphene. *Talanta* **2016,** *154*, 99-108.
19. Haudebourg, R.; Matouk, Z.; Zoghlami, E.; Azzouz, I.; Danaie, K.; Sassiat, P.; Thiebaut, D.; Vial, J., Sputtered alumina as a novel stationary phase for micro machined gas chromatography columns. *Analytical and bioanalytical chemistry* **2014,** *406* (4), 1245-1247.
20. Stadermann, M.; McBrady, A. D.; Dick, B.; Reid, V. R.; Noy, A.; Synovec, R. E.; Bakajin, O., Ultrafast gas chromatography on single-wall carbon nanotube stationary phases in microfabricated channels. *Analytical Chemistry* **2006,** *78* (16), 5639-5644.
21. Gross, G. M.; Grate, J. W.; Synovec, R. E., Monolayer-protected gold nanoparticles as an efficient stationary phase for open tubular gas chromatography using a square capillary: Model for chip-based gas chromatography in square cornered microfabricated channels. *Journal of Chromatography A* **2004,** *1029* (1-2), 185-192.
22. Zhukhovitskii, A. A.; Zolotareva, O. V.; Sokolov, V. A.; Turkel'taub, N. M., New method of chromatographic analysis. *Dokl. Akad. Nauk SSSR* **1951,** *77* (3), 435-438.
23. Blumberg, L. M., Limits of Resolution and Speed of Analysis in Linear Chromatography with and without Focusing. *Chromatographia* **1994,** *39*, 719-728.
24. Contreras, J. A.; Wang, A.; Rockwood, A. L.; Tolley, H. D.; Lee, M. L., Dynamic thermal gradient gas chromatography. *Journal of Chromatography A* **2013,** *1302*, 143-151.
25. Contreras, J. A.; Rockwood, A. L.; Tolley, H. D.; Lee, M. L., Peak sweeping and gating using thermal gradient gas chromatography. *Journal of Chromatography A* **2013,** *1278*, 160-165.
26. Tolley, H. D.; Tolley, S. E.; Wang, A.; Lee, M. L., Moving thermal gradients in gas chromatography. *Journal of Chromatography A* **2014,** *1374*, 189-198.
27. Boeker, P.; Leppert, J., Flow Field Thermal Gradient Gas Chromatography. *Analytical Chemistry* **2015,** *87* (17), 9033-9041.
28. Wang, A.; Hynynen, S.; Hawkins, A. R.; Tolley, S. E.; Tolley, H. D.; Lee, M. L., Axial thermal gradients in microchip gas chromatography. *Journal of Chromatography A* **2014,** *1374*, 216-223.
29. Poole, C., *Gas Chromatography*. Elsevier: Waltham, MA, 2012.
30. Blumberg, L. M., *Temperature-programmed gas chromatography*. John Wiley & Sons: 2010.
31. Bartle, K., Film thickness of dynamically coated open-tubular glass columns for gas chromatography. *Analytical Chemistry* **1973,** *45* (11), 1831-1836.
32. Radadia, A. D.; Salehi-Khojin, A.; Masel, R. I.; Shannon, M. A., The effect of microcolumn geometry on the performance of micro-gas chromatography columns for chip scale gas analyzers. *Sensors and Actuators B: Chemical* **2010,** *150* (1), 456-464.

33. Radadia, A. D.; Masel, R. I.; Shannon, M. A.; Jerrell, J. P.; Cadwallader, K. R., Micromachined GC Columns for Fast Separation of Organophosphonate and Organosulfur Compounds. *Analytical Chemistry* **2008,** *80* (11), 4087-4094.
34. Reidy, S.; George, D.; Agah, M.; Sacks, R., Temperature-Programmed GC Using Silicon Microfabricated Columns with Integrated Heaters and Temperature Sensors. *Analytical Chemistry* **2007,** *79* (7), 2911-2917.
35. Reidy, S.; Lambertus, G.; Reece, J.; Sacks, R., High-Performance, Static-Coated Silicon Microfabricated Columns for Gas Chromatography. *Analytical Chemistry* **2006,** *78* (8), 2623-2630.
36. Cagliero, C.; Galli, S.; Galli, M.; Elmi, I.; Belluce, M.; Zampolli, S.; Sgorbini, B.; Rubiolo, P.; Bicchi, C., Conventional and enantioselective gas chromatography with microfabricated planar columns for analysis of real-world samples of plant volatile fraction. *Journal of Chromatography A* **2016,** *1429*, 329-339.
37. Lee, J.; Zhou, M.; Zhu, H.; Nidetz, R.; Kurabayashi, K.; Fan, X., Fully Automated Portable Comprehensive 2-Dimensional Gas Chromatography Device. *Analytical Chemistry* **2016,** *88* (20), 10266-10274.
38. Serrano, G.; Reidy, S. M.; Zellers, E. T., Assessing the reliability of wall-coated microfabricated gas chromatographic separation columns. *Sensors and Actuators B: Chemical* **2009,** *141* (1), 217-226.
39. Wang, J.; Bryant-Genevier, J.; Nuñovero, N.; Zhang, C.; Kraay, B.; Zhan, C.; Scholten, K.; Nidetz, R.; Buggaveeti, S.; Zellers, E. T., Compact prototype microfabricated gas chromatographic analyzer for autonomous determinations of VOC mixtures at typical workplace concentrations. *Microsystems &Amp; Nanoengineering* **2018,** *4*, 17101.

Chapter 6 Ultra-compact One-dimensional GC System

6.1 Introduction

In chapter 1, motivation for μGC development as devices for field applications was discussed. The conventional portable GC is essentially a miniaturized version of the bench-top GC, employing the same architecture, but using a short commercial capillary-based GC column or a microcolumn and miniaturized vapor detector[1-6]. While μGCs are portable and provide rapid vapor analysis, they currently suffer from poor separation capabilities and peak capacities due to short column lengths resulting from miniaturization. Therefore, only a small set or limited, well defined classes of vapors can be separated, while complex sample matrices cannot be analyzed. In this chapter, an on-chip, highly compact μGC was developed using microfabrication of microcolumns, micro preconcentrators, and micro PIDs[7]. This μGC can serve as a module to build multichannel and multidimensional GC systems.

6.2 System Design

The microfabricated components, pump, multi-port valves, and portable helium cylinder are controlled through a DAQ card (USB 6003 OEM) from National Instruments. In sampling mode (Figure 6.1 A), the pump was connected with a μpreconcentrator through a three-port valve. The two-port valve is opened to allow sample gas to enter the μpreconcentrator via vacuum pump. Due to the high flow resistance of the column side, the flow contribution from the column is negligible. In analysis mode (Figure 6.1 B), desorption and separation occur sequentially. First, the three-port valve is switched to connect the μpreconcentrator to the carrier gas source, while the two-port

valve is closed to prevent carrier gas venting. In desorption, the µpreconcentrator is rapidly heated using 24 VDC for 0.75 s to heat the device to 280 °C. A 11 % pulse width modulated control was then applied on the 24 VDC source for 8 s to continuously heat the µpreconcentrator to 310 °C. The temperature was maintained to release trapped chemicals. The column was heated using a proportional integral derivative feedback control by reading the temperature from the column. The micro PID detects total analyte quantity, and the resulting signal is used to generate the chromatogram.

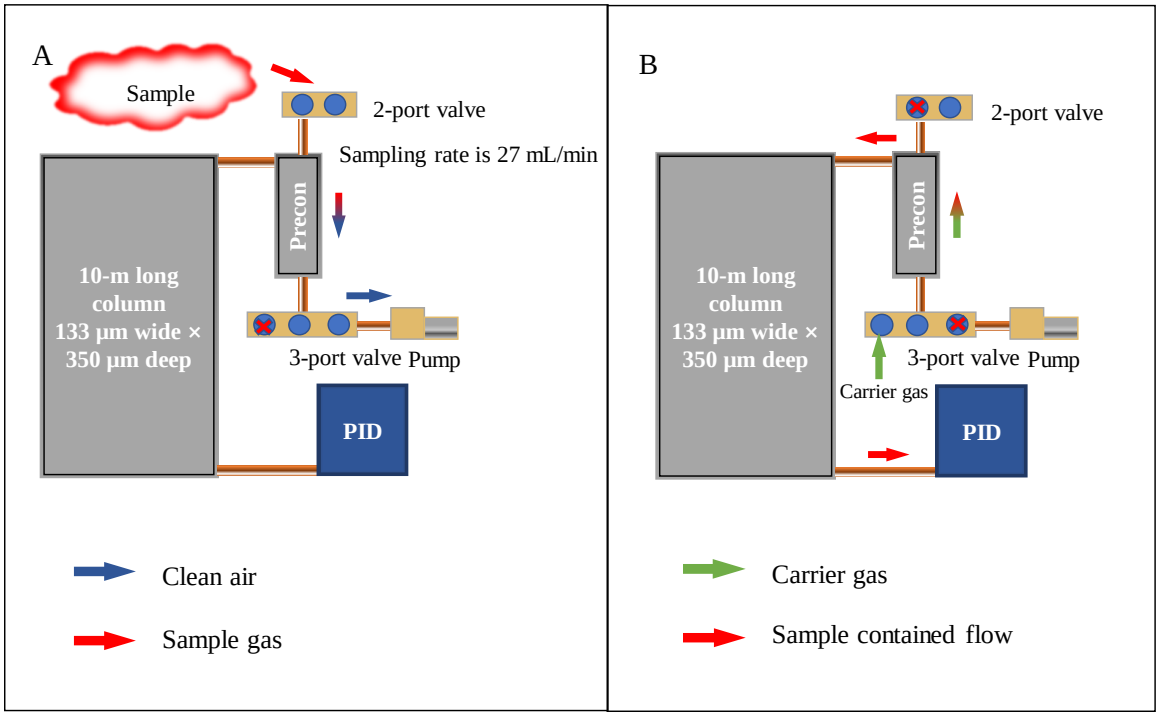

Figure 6.1 Flow configuration of one-dimensional GC system in (A) sampling mode and (B) analysis mode.

The electric control diagram is shown in Figure 6.2. A digital output provided a logical control (5V) to the MOSFET, which served as a relay to control corresponding components. The system input power of 24 VDC was converted to 5 VDC and 12 VDC using a voltage converter. The homemade control board also included a current source that provided 300 µA. Two analog

channels (16 bit) were used to collect the micro PID signal and resistance temperature detector (RTD) voltage signal.

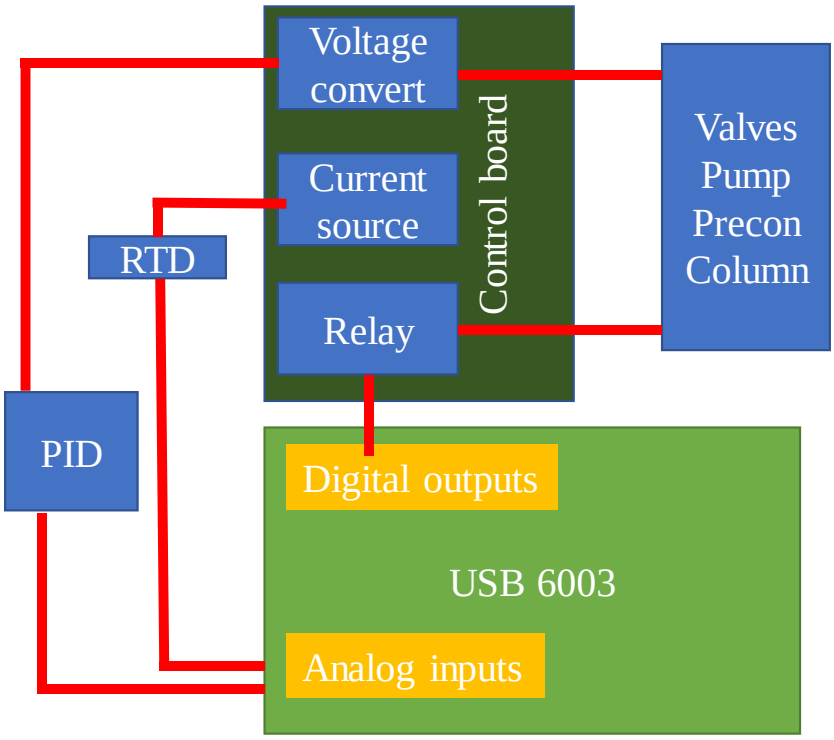

Figure 6.2 Integrated electric control diagram.

6.3 Micro GC Materials

The printed circuit board (PCB) was designed in our lab and manufactured by Advanced Circuits. All chemicals used for analysis were obtained from Sigma-Aldrich (St. Louis, MO). The micro two-port (P/N LHDB1252115H) and three-port valves (P/N LHDA1221311H) were purchased from Lee Company (Westbrook, CT). The micro pump (P/N NMP03KPDC-M) was purchased from KNF (Trenton, NJ).

6.4 Micro-preconcentrator

The μpreconcentrator was made on a silicon wafer using standard photolithography processes. It contains multiple beads capable of accommodating different types of absorbent materials (see Figure 6.3). 5 different absorbing materials with a total mass of ~3 mg were used: Carbopack™

C, Y, B, X, and Carboxen® 1000. The applicability range of these adsorption materials is summarized in Table 6.1.

Table 6.1 Chemical applicable range of adsorption materials.

Adsorption	Partial size	Specific surface area m^2/g	Chemical range
Carbopack™ C	60-80 mesh	10	C_{12}- C_{20}
Carbopack™ Y	60-80 mesh	24	C_9 – C_{14}
Carbopack™ B	60-80 mesh	100	C_5 – C_{12}
Carbopack™ X	60-80 mesh	240	C_3 – C_9
Carboxen® 1000	60-80 mesh	1200	C_2 – C_5

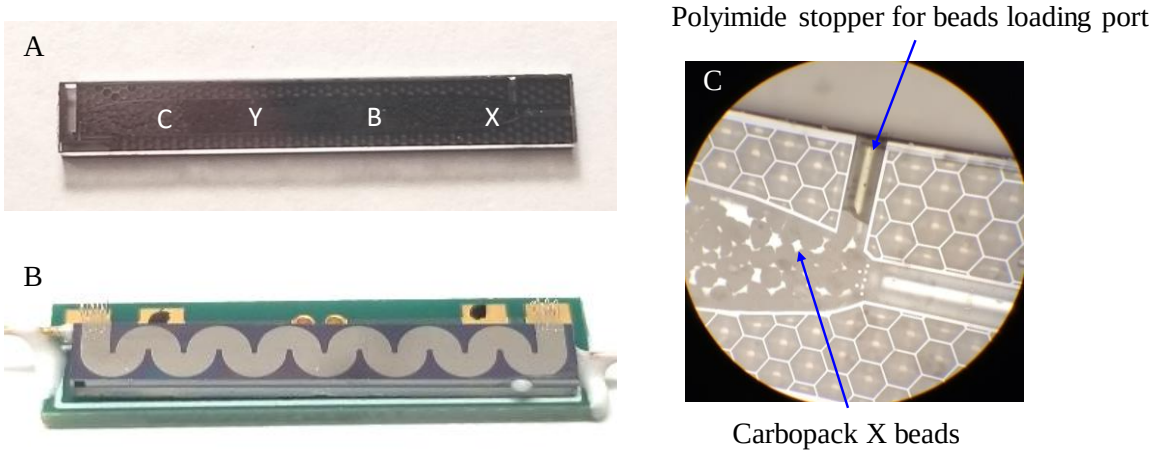

Figure 6.3 (A) and (B) Front and back view of the microfabricated preconcentrator. (C) Zoomed-in view. The preconcentrator has 4-5 absorbent beds filled with Carbopack C, Y, B, and X, and Carboxen, respectively, to capture C_3 – C_{20}. The device can be heated to 320 ºC in 1 s.

The micro-preconcentrator was heated to 320 ^oC in 1 s and the resulting FWHM (full-width at half-maximum) of the signal peak was about 800 ms (Figure 6.4). The energy consumption per injection is ~40 J. µpreconcentrator thermal stability was testing by heating to 320 ^oC for 15 minutes using a flow of dry air, which is equivalent to 110 injections (note that during the actual injection, the µpreconcentrator stays at 320 ^oC for less than 1 second). No degradation in capturing efficiency and injection peak width was found after prolonged use (more than 500 injections in

helium), demonstrating the high thermal stability of the μpreconcentrator. The novel hybrid gluing method discussed in Chapter V was applied to make fluidic connections for all components in this GC system. Owing to the thermal stability of the hybrid gluing method, the injection background (unexpected peaks or baseline drift at the beginning of separation) of the μpreconcentrator was also very low.

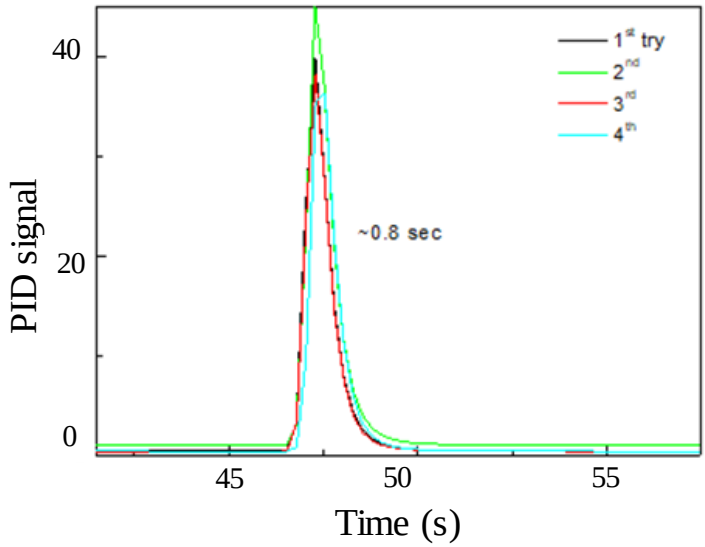

Figure 6.4 μpreconcentrator repeatability test. The full-width-at-half-maximum is approximately 0.8 s. The preconcentrator is heated to about 320 ºC in 1 s with 48 W and then 2 W for an additional 8 seconds for complete VOC release. Although the injection width is larger than the best current results (which can be as sharp as 0.25 s), the elution peak width is dominantly determined by the column, not by injection.

6.5 Micro-column

A 10-m long, uniformly coated microcolumn was used for this μGC. The fabrication process for this microcolumn was detailed in Chapter V. The coating setup is shown in Figure 6.5. After pre-activation, a 200 μL coating solution was loaded into the column by syringe pumping from the inlet. 15 psi of dry air was applied from the inlet to drive the coating solution towards the outlet. Post processing (drying and aging, described in Chapter V) was applied to treat the column after coating. The thickness of the stationary phase film can be controlled by changing the coating solution concentration (Figure 6.6). The microcolumn was mounted on a PCB board with Duraseal

and wire bonded with aluminum wire to connect the heater electrodes and RTD electrodes to a gold finished mounting pad on the PCB. RTD calibration is required to obtain coefficients for temperature as a function of resistance and the measurement is obtained by reading the voltage across the resistor using a constant current source

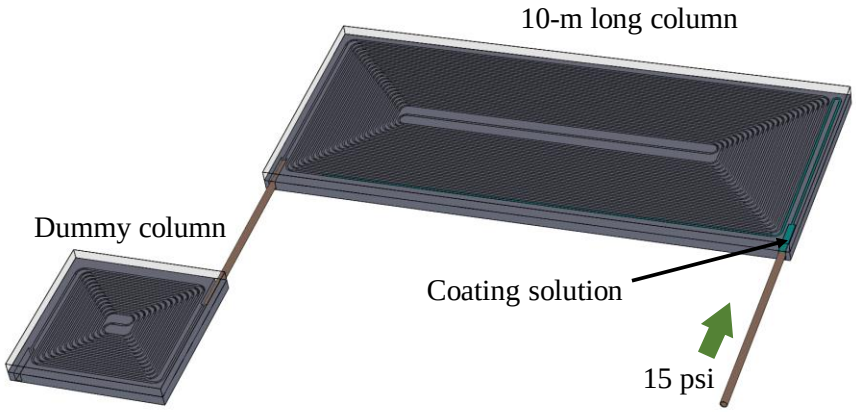

Figure 6.5 Uniformly coated column coating setup.

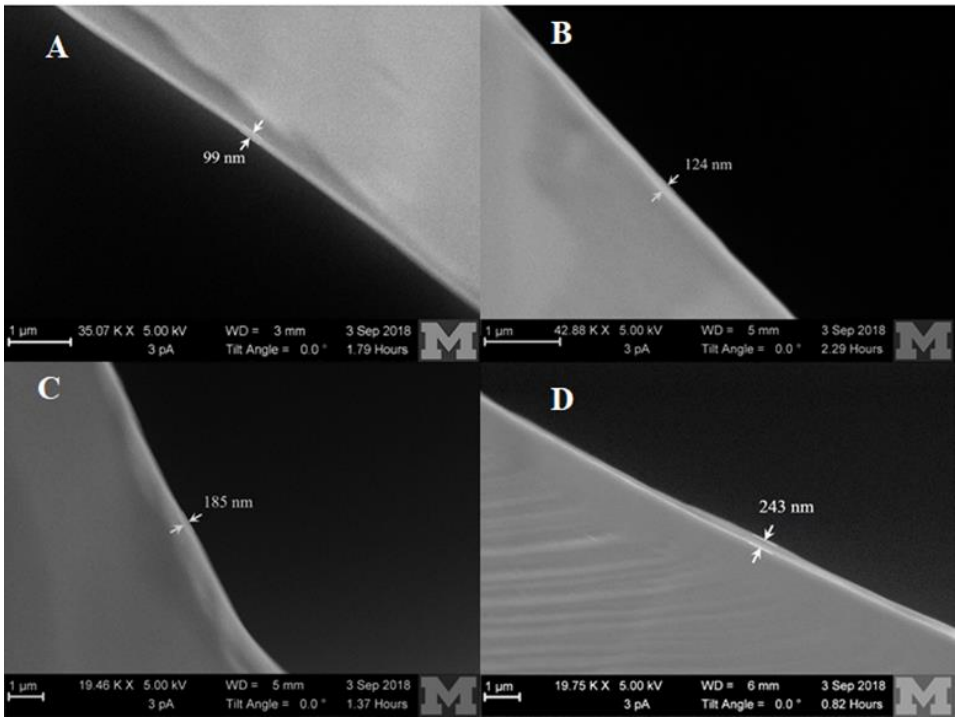

Figure 6.6 SEM image of the column coating (OV-5) thickness using different concentrations

(m/V) of coating solution. (A) 2%. (B) 3%. (C) 4%. (D) 5%.

6.6 System overview

The fluidic connections were made using the hybrid gluing method shown in Figure 6.7. Figure 6.8 shows the fully automated one-dimensional µGC which integrated the aforementioned components. It weighs 147 g (excluding batteries and the helium cartridge) and has a volume of only 0.14 L. It can use both helium and dry air as the carrier gas. The power consumption is 2 W for sampling and 40 J per injection. The energy used on column heating varies with target temperature and separation time. Our testing used 5 W to heat the column to 120 °C.

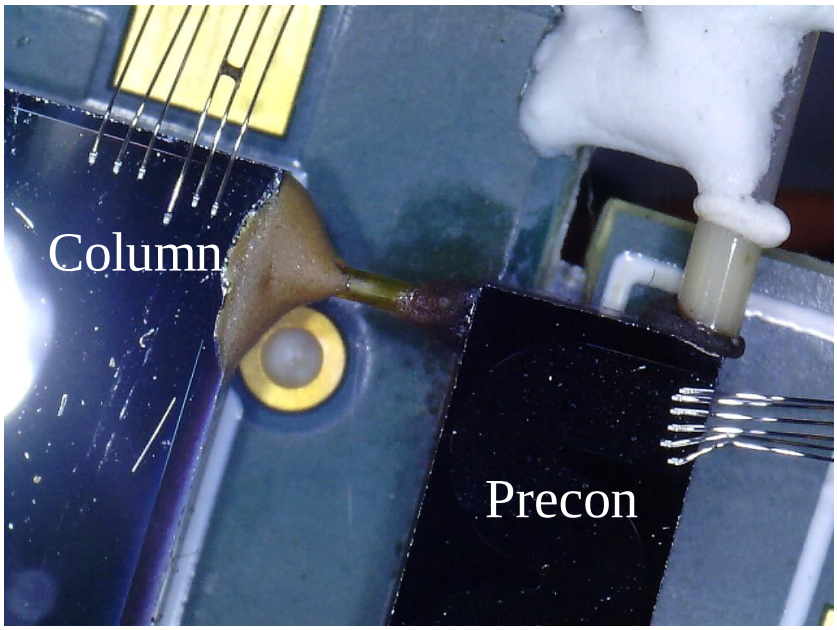

Figure 6.7 Fluidic connection interface between microcolumn and µpreconcentrator.

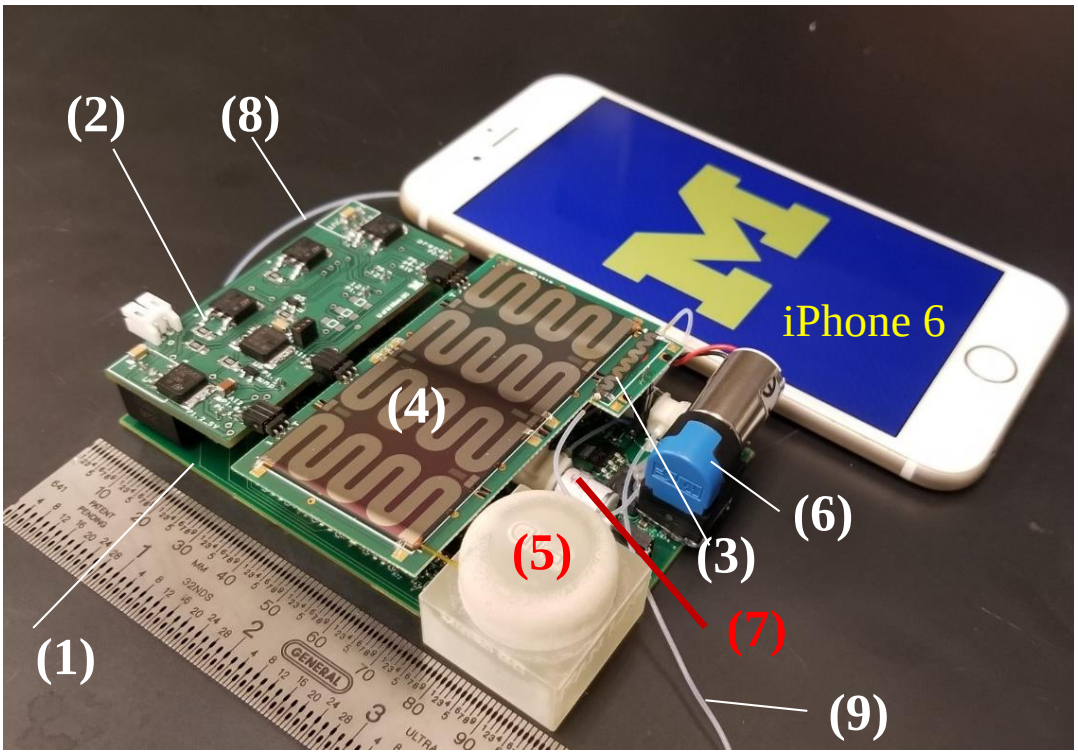

Figure 6.8 Automated ultra-compact 1D micro-GC with a 10-m column. Weight: 147 g (excluding batteries). Dimensions: 10 cm x 7 cm x 2 cm (0.14 L). Sampling power: 2 W. Analyzing power: 5 W. 1. NI DAQ card; 2. Customized PCB board for GC operation; 3. μpreconcentrator; 4. 10-m long column; 5. Micro-PID; 6. Mini-pump; 7. Valve; 8. Analyte inlet; 9. Carrier gas inlet.

6.7 Separation

A separation of a 14 analyte mixture was performed. The mixture contains 1,2-Dichloroethane, 2,5-Dimethylbenzaldehyde, Acetone, Benzene, Cyclohexanol, Cyclohexanone, Dichloromethane, Dimethyl sulfide, Heptane, Nitrobenzene, Octane, o-Xylene, Toluene, and Vinyl acetate and was prepared using analytical standard grade pure compounds in equal volume ratios and diluted to 12.5 ppm (V/V) with water. A purge-and-trap setup (same as in Chapter IV) was used to generate the mixture vapor. After 1 min of sampling, the separation was performed with a 10-m long programmably heated column with an initial temperature of 30 °C held for 1 min

and ramped to 150 °C with a rate of 15 °C/min at flow rate of 1.2 mL/min. The resulting chromatogram is shown in Figure 6.9.

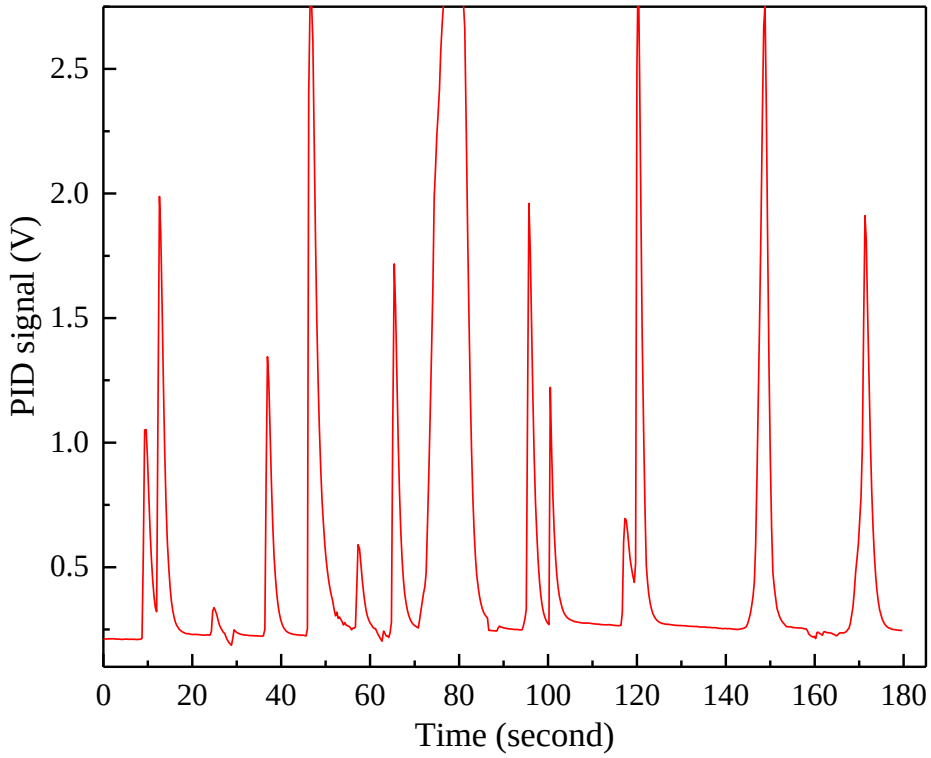

Figure 6.9 Separation chromatography of a 14 analyte mixture using 30 min sampling and separated using an initial temperature of 30 °C for 1 min and ramped to 150 °C with rate of 15 °C/min at flow rate of 1.2 mL/min.

6.8 Conclusions

The work presented in this chapter details the electric and fluidic control strategies for an ultra-compact µGC. This system was developed based on previous work on miniaturization of the detector, column, and preconcentrator. Golay[8] proposed a dynamic model of a rectangular cross-section column, which theoretically showed that a high aspect ratio channel structure can improve the separation efficiency of a MEMS micro GC column. IN general, scaling down the size of columns and other components can benefit GC performance. However, the development of individual component should not adversely impact other components. Common issues such as the

high pressure required for narrow columns, cold spots in connection columns, and thermal crosstalk need to be prevented for systemic design.

6.9 References

1. Oldridge, N.; Panic, O.; Górecki, T., Stop-flow comprehensive two-dimensional gas chromatography with pneumatic switching. *Journal of Separation Science* **2008,** *31* (19), 3375-3384.
2. Whiting, J. J.; Fix, C. S.; Anderson, J. M.; Staton, A. W.; Manginell, R. P.; Wheeler, D. R.; Myers, E. B.; Roukes, M. L.; Simonson, R. J. In *High-speed two-dimensional gas chromatography using microfabricated GC columns combined with nanoelectromechanical mass sensors*, TRANSDUCERS 2009 - 2009 International Solid-State Sensors, Actuators and Microsystems Conference, 21-25 June 2009; 2009; pp 1666-1669.
3. Kim, S.-J.; Reidy, S. M.; Block, B. P.; Wise, K. D.; Zellers, E. T.; Kurabayashi, K., Microfabricated thermal modulator for comprehensive two-dimensional micro gas chromatography: design, thermal modeling, and preliminary testing. *Lab on a Chip* **2010,** *10* (13), 1647-1654.
4. Zeng, Z.-D.; Chin, S.-T.; Hugel, H. M.; Marriott, P. J., Simultaneous deconvolution and re-construction of primary and secondary overlapping peak clusters in comprehensive two-dimensional gas chromatography. *Journal of Chromatography A* **2011,** *1218* (16), 2301-2310.
5. Seeley, J. V., Recent advances in flow-controlled multidimensional gas chromatography. *Journal of Chromatography A* **2012,** *1255*, 24-37.
6. Akbar, M.; Shakeel, H.; Agah, M., GC-on-chip: integrated column and photoionization detector. *Lab on a Chip* **2015,** *15* (7), 1748-1758.
7. Zhu, H.; Nidetz, R.; Zhou, M.; Lee, J.; Buggaveeti, S.; Kurabayashi, K.; Fan, X., Flow-through microfluidic photoionization detectors for rapid and highly sensitive vapor detection. *Lab on a Chip* **2015,** *15* (14), 3021-3029.
8. Golay, M. J. E., Vapor Phase Chromatography and Telegrapher's Equation. *Analytical Chemistry* **1957,** *29* (6), 928-932.

Chapter 7 Conclusions and Future Directions

7.1 Conclusions

The main topics of this dissertation discussed improvement of detectors, columns, and preconcentrators and presented design, assembly, and characterization of these components. This chapter summarizes the aforementioned developments and briefly analyzes obtained results. An outlook on development of micro GC technology is discussed at the end of this chapter.

The first chapter provided a review of GC mechanisms, technologies, and applications GC as well as motivation for μGC. It also provided a critical analysis of the development of micro components and system performance.

The second chapter presented the development of a rapid, flow-through, and highly sensitive microfluidic PID that was microfabricated directly on a conductive silicon wafer. The microfluidic PID has a significantly reduced ionization chamber volume of only 1.3 μL, nearly 10 times smaller than other state-of-the-art PIDs and over 100 times smaller than commercial PIDs. Moreover, it has virtually zero dead volume due to its flow-through design. Consequently, the response time of the microfluidic PID is considerably shorter, ultimately limited by its residence time (7.8 ms for 10 mL/min and 78 ms for 1 mL/min). Experimentally, the response of the microfluidic PID was measured to be the same as the standard flame ionization detector, with a peak full-width-at-half-maximum of 0.25 s and 0.085 s for a flow rate of 2.3 mL/min and 10 mL/min, respectively. Our studies further showed that the microfluidic PID was able to detect analytes down to the picogram level (at 3 σ of noise) and had a linear dynamic range of six orders

of magnitude. Finally, because of the very short distance between the electrodes, low voltages (<10 VDC, over 10 times lower than that in a regular PID) can be used for microfluidic PID operation. This work will open a door to broad applications of PIDs in gas analyzers, particularly micro-GC and multi-dimensional GC.

The third chapter presented the design, fabrication, and characterization of a helium dielectric barrier discharge-based micro on chip photoionization detector (μHDBD-PID) with dimensions of only ~15 mm × ~10 mm × ~0.7 mm and a weight of only ~0.25 g. This device offers low power consumption (<400 mW), low helium consumption (5.8 mL/min), rapid response (up to 60 ms at a flow rate of 1.5 mL/min), quick warm-up time (~5 min), excellent detection limit (few pg), large linear dynamic range (>4 orders of magnitude), and maintenance-free operation. Furthermore, the μHDBD-PID can be driven with a miniaturized (~5 cm × ~2.5 cm × ~2.5 cm), light (22 g), and low cost (~$2) power supply with only 1.5 VDC input. The dependence of the μHDBD-PID performance on bias voltage, auxiliary helium flow rate, carrier gas flow rate, and temperature was also systematically investigated. Finally, the μHDBD-PID was employed to detect permanent gases and a sub-list of the EPA 8260 standard reagents that includes 51 analytes. The sensor developed in this chapter has a broad range of applications in portable and micro-gas chromatography systems for *in situ*, real-time, and sensitive gas analysis.

Chapter 4 focused on the development of an automated, highly portable device for rapid and sensitive formaldehyde detection based on heart-cutting, two-dimensional GC. In this design, the air sample was first absorbed by a preconcentrator before injection into the first-dimensional column (Rtx®-VMS). The partial elution from the first-dimensional column containing formaldehyde was re-injected into the second-dimensional column (Rt® Q-BOND column) for further separation. Detection of formaldehyde was achieved by using a μHDBD-PID capable of

ionizing formaldehyde (ionization potential = 10.88 eV). Due to the use of many miniaturized components, the entire system had a weight of only 1.3 kg (excluding the helium cartridge) and dimensions of 27 cm x 24 cm x 12 cm. It is capable of detecting formaldehyde down to 0.5 ppb (V/V) with a signal-to-noise ratio of 6 and an analysis time of 11 minutes. Simultaneous separation and detection of other air pollution-related toxic compounds such as benzene, toluene, ethylbenzene, and xylene, was also demonstrated by the first-dimensional column and a flow-through micro-photoionization detector. The device developed here has a broad range of applications in environmental protection, energy industries, space exploration, and military applications.

Chapter 5 described a novel film thickness gradient column that enables peak focusing in gas chromatography. A theoretical analysis was first performed to elucidate the peak focusing effect through the positive film thickness gradient. Peak focusing was then experimentally verified by using a 10 m long microcolumn fabricated on a silicon wafer and coated with a stationary phase whose thickness increased from approximately 140 nm at the column inlet to approximately 190 nm at the column outlet. By comparing the chromatograms obtained when the microcolumn was operated in forward and backward modes, a focusing rate of up to 35% was achieved. The peak focusing effect was demonstrated for various temperature programmed separations with different ramping rates as well as for isothermal separation. Finally, separation of the ASTM D2887 standard mixture ($C_5 – C_{44}$) using the same microcolumn with temperature ramping to 350 ^oC was demonstrated to show the microcolumn's separation capability and thermal stability.

Chapter 6 presented development of an ultra-compact one-dimensional GC which integrated aforementioned components in a 0.14 L volume. This system weighs 147 g and can use both helium and dry air as carrier gases. 2 W of power is consumed for sampling and 40 J is required

per injection. The energy used for column heating varies with target temperature and separation time; our experiment used 5 W to heat the column to 120 °C. However, the detection of chemicals with low volatility is limited by use of a nonheated detector, which will encounter condensation.

7.2 Future Directions

The preceding chapters present development of μGC components and systems which target applications in field analysis such as human chemical exposure, national security, and environmental contamination. Further improvements can target reductions in size, weight, and power consumption, while performance should be improved with better separation, lower detection limit, and broader applicability to various chemicals (volatility range).

7.2.1 Multidimensional and multichannel system

To achieve a higher separation capacity, we proposed use of multichannel and multidimensional μGCs. The ultra-compact one-dimensional GC (chapter six) demonstrated high performance for VOC analysis, and can be used as a separation module in multidimensional GC systems. This modular design simplifies modifications of system configuration. For example, a 1x4 GC system can be easily changed to a 1x2x2 three-dimensional system. The Deans switch should ideally be heatable to reduce chemical condensation in cold areas, but thermal transfer between the Deans switch and thermal injector should be avoided to prevent tapping efficiency losses in the thermal injector. Furthermore, the flow balance between channels is required to be well adjusted and channel flow resistances should be ideally identical.

7.2.2 Microcolumn and monolithic column/injector

The microcolumn developed in chapter four has an open tubular design. Further work may consider semipacked and multichannel structures for higher column efficiency per unit length; however, the tradeoff between high column efficiency and high system pressure must be

considered for future designs. In addition, due to the improved column layout density in this work, we instead consider column efficiency per unit chip area, since a longer length of microcolumn can be fabricated in the same area of silicon. Channel cross section structure optimization may be another promising area for column improvement.

Integrating columns with preconcentrators/thermal injectors can reduce the number of connection ports, but thermal crosstalk between column and preconcentrator/thermal injector can impair separation efficiency. Thermal expansion mismatch can also induce cracks, which is another challenge for monolithic chip design.

7.2.3 Detector

Currently, the μPID microfluidic channel is not heated, which results in likely contamination of the UV transparent window. In the future, the μPID channel can be integrated with heaters to prevent chemical condensation. Signal amplification should be redesigned and separated from the microfluidic channel to prevent output drift that is induced by thermal transfer from the heated channel.

In conclusion, the improvement of aforementioned devices and systems can aid in solving many practical problems and applications such as breath analysis for clinical diagnoses, plant infections, and soil contaminant analysis. Chemical identification analysis can be performed from rigorous retention time matching with preloaded libraries. Packaging and thermal insulation of various components provides mechanical support and may be especially useful for applications in harsh condition and for further energy cost reduction.

Appendix 1 Column Fabrication Process

A1.1 Create mask for micro column pattern

Create metal contact mask with column pattern shown in Figure A1.1

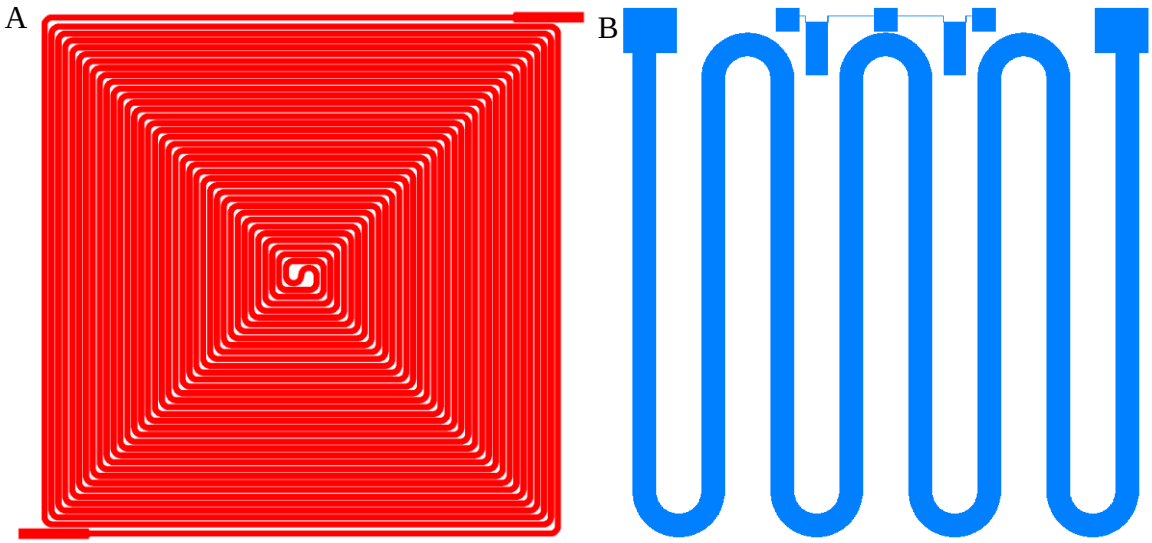

FigureA1. 2 Pattern example (A) microcolumn channel, (B) microcolumn heater.

A1.2 Channel creation with deep reactive ion etching etch

- Spin coat the front side with 3 µm SPR 220 3.0 photoresist on double side polished silicon wafer after HMDS primer reaction. Bake at 115 °C for 90 s
- Expose for 7 s with mask patterned for silica hard mask which includes deep and shallow etching area.
- Post bake at 115 °C for 90 s and develop with MF 300 for 32 second (For AZ726 developer, development time is required to be 30 s + 30 s with double puddle)

- Clean the wafer backside.
- Run deep reactive ion etching for 390 μm deep after with 1.5 min Argon plasma descum.
- Clean up the remained C4F8 film with Strip off all photoresist with oxygen plasma through YES Plasma Stripper (800 W, 360 sec, 80 mL/min O2, 150°C).

A1.3 wafer bonding

- Run Organic clean with Nanostrip at 60 °C for 10 min and risen 6 times with DI water.
- Bake the wafers on a 130°C hotplate for 5 min to remove the remaining water
- Load the wafers onto the SB-6e chuck. The Si wafer is loaded first, with the etched surface facing up. Insert the flags. Then, the glass wafer is loaded. Engage the clamps. Place the bonding plate on top of the wafer stack such that the metal is showing on top.
- Load the chuck into the SB-6e. Run the anodic bonding recipe, which bond process is carried out at 350 °C, 1 mbar pressure, and stopped at 2% of peak bonding current.
- After the bonding, carefully unload the wafers and inspect the bond. Fringing is a sign of debris/incomplete bonding.

A1.4 Metallization of the heaters and RTDs

- Oxygen plasma clean up on Si wafer back side with YES Plasma recipe 2 (800 W, 360 sec, 80 sccm O_2, 150°C).
- Using the CEE100B, spin LOR-10B 5 sec @ 500 rpm (spread) + 30 sec @ 3000 rpm (spin). Bake at 190°C for 5 min on a hotplate.
- Using the CEE100B, spin S1813. 5 sec @ 500 rpm (spread) + 30 sec @ 4000 rpm (spin). Bake at 115°C for 4 min.

- Use back side alignment and expose t = 6.3 sec SOFT contact on MA/BA-6. Develop on the CEE Developers. Run AZ726 40 sec SP.
- Run the Enerjet Evaporator to deposit Ti (150 Å, 10 Å/sec), Al (1500 Å, 10 Å/s)
- Soak wafers in Remover PG overnight to initiate liftoff.
- Transfer wafers (2 at a time, maximum) to fresh, hot (80°C) Remover PG and soak for 20 minutes. Then use ultrasonics (power < 2) for an additional 5 minutes.
- Rinse wafers with IPA to remove particles.

A1.5 Dicing

- Spin coat PR on the metallized Si surface to protect the metal during dicing. Spin SPR 220 3.0 at 3000 rpm and bake for 90 sec at 115°C.
- Dice the wafers
- After the columns are diced, use the blowout kit to remove debris from the devices.

Appendix 2 Preconcentrator/thermal Injector Fabrication Process

A2.1 Thermal oxidation

- Use DSP Si wafer with thickness of 525 µm for thermal oxidation with target thickness of 1.5 µm. Pre-furnace cleaning process is required before oxidation which includes three-stage cleaning.
- Transfer wafers to silica boat in thermal oxidation tube for oxidization. The wet oxidation time and optimized temperature for target thickness can be found online.
- Characterize oxidation layer thickness with NanoSpec 6100 through non-contact spectroscopic reflectometry.

A2.2 Create silica hard mask and first step etching

- Create mask with preconcentrator/thermal injector patterns shown in Figure A2.2

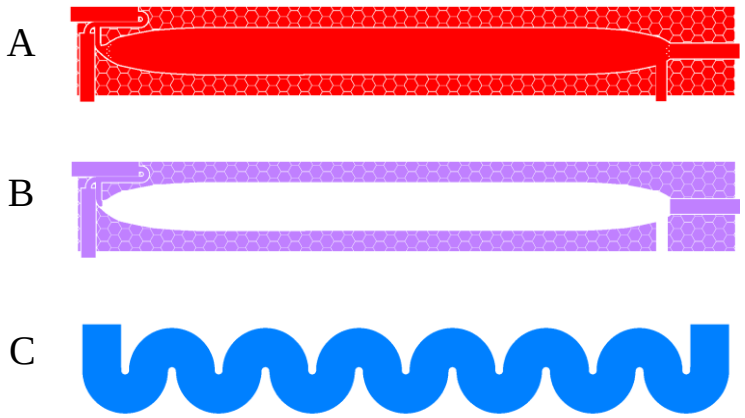

FigureA2. 2 Photo lithography pattern of, (A) silica hard mask pattern of preconcentrator, B) Deep etching pattern for inlet, outlet, and mass remove area, C) Heater pattern.

- Spin coat the front side with 3 µm SPR 220 3.0 photoresist after HMDS primer reaction. Bake at 115 °C for 90 s

- Expose for 7 s with mask patterned for silica hard mask which includes deep and shallow etching area.
- Post bake at 115 °C for 90 s and develop with MF 300 for 32 second (For AZ726 developer, development time is required to be 30 s + 30 s with double puddle)
- Clean the wafer backside and then mount on silicon carrier wafer with Santovac 5 under vacuum for 5 min at 80 °C.
- Etch off silica layer using 'uk submicron' method for 7 min at STS deep glass etcher to create silica pattern, which includes deep and shallow etch area.
- Measure the oxide thickness using the Nanospec to ensure that the oxide is fully etched through.
- Clean off Santovac 5 with acetone and deep cleaned with Nanostrip for 20 min at 60 °C
- Rinse with deionized water and spin dry
- prime the silicon wafer on silica pattern side and spin coat with layer of 3 µm SPR 220 3.0 photoresist followed by 115 °C, 90 s baking.
- Expose for 8 s with mask patterned for deep etching area.
- Develop with MF 300 for 35 second
- Carefully clean the back side with acetone. And load to STS Pegasus 4 for DRIE with the recipe after blowing with nitrogen gun.
- Run same DRIE process in section A1.2 to create 150 µm deep channels
- Inspect DRIE using microscope and Zygo to confirm etch depth of the inlets/outlets.

A2.3 Second step etching area etching

- Strip off all photoresist with oxygen plasma through YES Plasma Stripper (800 W, 600 sec, 80 mL/min O2, 150°C)

- Continue DIRE at STS Pegasus 4 with same recipe for another 250 µm deep.
- Inspect DRIE using microscope and Zygo to confirm etch depth of the inlets/outlets and the column or beads loading bed at both the center and edge of the wafer. It is common for the edges to etch faster. However, low pattern density case, the center will etcher faster due to thermal effect. Continue until the desired etch depths are achieved.
- Clean up the remained C4F8 film with Strip off all photoresist with oxygen plasma through YES Plasma Stripper (800 W, 360 sec, 80 mL/min O2, 150°C)
- trip off remained oxide layer with buttered HF (etching rate 100 nm/min). an additional 60 seconds of etch time to ensure the oxide is totally stripped everywhere to account for rate variability across the wafer.
- Run Organic clean with Nanostrip at 60 °C for 10 min and risen 6 times with DI water

A2.4 Wafer bonding, metal deposition, and dicing

- On the CEE100B, using a blank Si dummy wafer, spin S1827 for 3 sec @ 2000 rpm.
- The photoresist on the dummy wafer will be very wet. Mount the etched, DSP wafer on the dummy/carrier wafer such that the back side (unetched) of the DSP wafer comes in contact with the photoresist without dirtying the front side of the wafer, rotate the top DSP wafer a full 360 degrees to improve contact between the wafers and reduce bubbles/gaps in the PR.
- Transfer the mounted wafer to a 110°C oven and bake for 30 min. Transfer to a 115°C hotplate and bake for another 60 sec. Let the wafers cool for 5 min.
- Buffered HF (BHF) etch of SiO_2 hard mask using the BHF tank. The etch time is determined by the remaining oxide thickness on the front side of the wafer which was measured in step 3-4. Generally, BHF etches thermal oxide at a rate of ~1000 Å/min. As a good rule, add an

additional 60 seconds of etch time to ensure the oxide is totally stripped everywhere to account for rate variability across the wafer.

- After the etching, rinse with DI water and manually dry the wafers with a N_2 gun.
- Inspect the wafer using a microscope to check for any remaining spots of oxide. If there are areas in the field that will not be on the final device, they may not matter. Remaining oxide thickness can be checked using the Nanospec. Any value less than 100 Å is acceptable as that is the lower limit of the tool. If necessary, continue etching with BHF.
- Run following bonding, metal deposition, and dicing as mentioned in Appendix 1